Advances in Acoustics and Vibration

Recent Trends of Computational Methods in Vibration Problems

Guest Editors: Snehashish Chakraverty, Atma Sahu, Choong Kok Keong, and Saleh M. Hassan

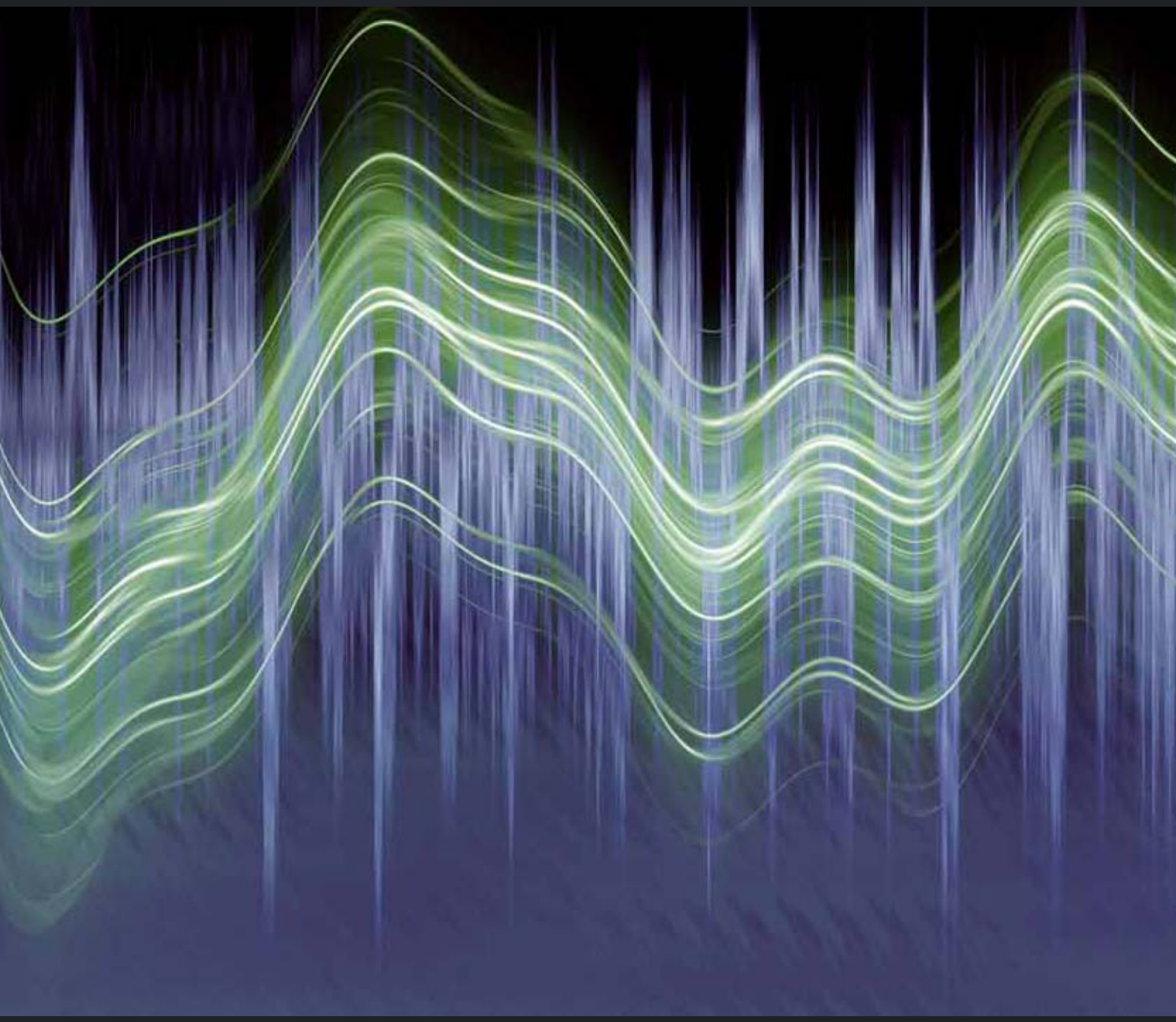

Recent Trends of Computational Methods in Vibration Problems

Advances in Acoustics and Vibration

Recent Trends of Computational Methods in Vibration Problems

Guest Editors: Snehashish Chakraverty, Atma Sahu, Choong Kok Keong, and Saleh M. Hassan

Editorial Board

Contents

Hindawi Publishing Corporation
Advances in Acoustics and Vibration
Volume 2012, Article ID 645981, 2 pages
doi:10.1155/2012/645981

Editorial

Recent Trends of Computational Methods in Vibration Problems

Snehashish Chakraverty,[1] Atma Sahu,[2] Choong Kok Keong,[3] and Saleh M. Hassan[4]

[1] *Department of Applied Mathematics, National Institute of Technology, Rourkela 769 008, India*
[2] *Department of Mathematics, Coppin State University, Baltimore, MD 21216, USA*
[3] *School of Civil Engineering, Universiti Sains Malaysia, Engineering Campus Seri Ampangan, 14300 Nibong Tebal, Malaysia*
[4] *Department of Mathematics, College of Sciences, King Saud University, P.O. Box 2455, Riyadh 11451, Saudi Arabia*

Correspondence should be addressed to Snehashish Chakraverty, sne_chak@yahoo.com

Received 23 October 2011; Accepted 23 October 2011

Prior to developing expensive prototype systems in engineering and sciences, it is well known that computational methods are often called into inquiry. Therefore, in order to allow prototyping of engineering systems to be in greater confidence, the degree of correlation between computational modeling predictions and experimental results has to be adequate. Accordingly, new and efficient computational methods help in determining the validation of the experimental results giving rise to a reliable and timely design systems.

The aim of this special issue is to bring together the leading researchers of dynamics and vibration area including applied mathematicians, and allow them to share their original research work. Mathematical theory, numerical simulation, physical experiments with advanced computational investigations, engineering design, and their various engineering applications are included in the main program of the issue.

Accordingly, various papers on vibration analysis have been included in this special issue after completing a careful rigorous peer-review process. In particular, a new actuator for reducing rotor vibrations in electrical machines is investigated in one of the papers. In addition to the traditional prediction error method, a new knowledge-based artificial Fish-Swarm optimization algorithm (AFA) with crossover, CAFAC, is proposed to identify the parameters in the new model. The prediction error method (PEM) is also employed to identify the induction motor to produce a black box model with correspondence to input-output measurements.

Another paper is of use of particle Swarm optimization to find the best teeth modifications for multimesh helical gears, which are crucial for the static transmission error (STE). Robustness of the solutions toward manufacturing errors and applied torque is analyzed by the particle Swarm algorithm to access to the deterioration capacity of the tested solution.

In another paper, the homotopy analysis method (HAM) is employed to propose a highly accurate technique for solving strongly nonlinear aeroelastic systems of airfoils in subsonic flow. The frequencies and amplitudes of limit cycle oscillations (LCOs) arising in the considered systems are expanded as a series of an embedding parameter. Numerical examples show that the HAM solutions are obtained very precisely.

Then stochastic BEM has been used to handle geometrical uncertainties within the classic BEM formulation. As a result, the solution shows deterministic behaviour at low frequencies; decreasing the wavelength, the effect of the uncertainties smooths the response.

In order to assess the dynamic behavior of the high-speed vibratory drilling system, this study develops a rotor-based finite element model, integrated with the modelling of component interfaces. The current results indicate that the simulations are consistent with the experimental measurements.

The automotive gearbox rattle noise resulting from vibro-impacts that can occur between the idle gears under excessive velocity fluctuations of the shaft-driving gears imposed by engine torque fluctuation is also studied. This

study presents various effect components on the dynamic response of the idle gear.

As of today, vibration analysis of complex systems is commonly encountered in science and engineering practice. Analysis and design of such structures call for efficient computational tools. As such, the present issue has addressed recent trends of the computational methods that may be used in the said vibration problems. Finally, it is hoped that the present special issue would certainly ignite researchers new problem domain and enhance efficiency and accuracy of the solution methods in use to-day.

Snehashish Chakraverty
Atma Sahu
Choong Kok Keong
Saleh M. Hassan

Hindawi Publishing Corporation
Advances in Acoustics and Vibration
Volume 2012, Article ID 189376, 16 pages
doi:10.1155/2012/189376

Research Article

Dynamical Analysis of Long Fiber-Reinforced Laminated Plates with Elastically Restrained Edges

Liz G. Nallim,[1] Facundo J. Bellomo,[1] Ricardo D. Quinteros,[1] and Sergio Oller[2]

[1] *INIQUI-CONICET, Facultad de Ingeniería, Universidad Nacional de Salta, Avenue Bolivia 5150, 4400 Salta, Argentina*
[2] *International Center for Numerical Method in Engineering, (CIMNE) Technical University of Catalonia-Barcelona Tech (UPC), Edif. C1, Campus Nord, Jordi Girona 1-3, 08034 Barcelona, Spain*

Correspondence should be addressed to Liz G. Nallim, lnallim@unsa.edu.ar

Received 30 December 2010; Revised 7 August 2011; Accepted 14 September 2011

Academic Editor: Kok Keong Choong

This paper presents a variational formulation for the free vibration analysis of unsymmetrically laminated composite plates with elastically restrained edges. The study includes a micromechanics approach that allows starting the study considering each layer as constituted by long unidirectional fibers in a continuous matrix. The Mori-Tanaka method is used to predict the mechanical properties of each lamina as a function of the elastic properties of the components and of the fiber volume fraction. The resulting mechanical properties for each lamina are included in a general Ritz formulation developed to analyze the free vibration response of thick laminated anisotropic plates resting on elastic supports. Comprehensive numerical examples are computed to validate the present method, and the effects of the different mechanical and geometrical parameters on the dynamical behavior of different laminated plates are shown. New results for general unsymmetrical laminates with elastically restrained edges are also presented. The analytical approximate solution obtained in this paper can also be useful as a basis to deal with optimization problems under, for instance, frequency constraints.

1. Introduction

Fiber-reinforced composite laminated plates are extensively used in many engineering applications. The free vibration analysis of these plates plays a very important role in the design of civil, aerospace, mechanical, and marine structures. In addition to the favorable high specific strength and high specific stiffness, fiber-reinforced composite laminates offer the possibility of optimal design through the variation of stacking pattern, angle of fiber orientation, fiber content, and so forth, known as composite tailoring. All these mechanical and geometrical characteristics, as well as the various coupling effects that take place, must be considered in the prediction of the laminates dynamical response to assure that this is reliable, accurate, and adequate to the design requirements.

It is well known that laminated composite plates have relatively low transverse shear stiffness, playing the shear deformation an important role in the global and local behavior of these structures. Among the numerous theories used for laminated plates that include the transverse shear strain, the first-order shear deformation theory (FSDT) [1, 2] is adequate for the computation of global responses (such as natural frequencies) and simultaneously has some advantages due to its simplicity and low computational cost. Many investigations have been reported for free vibration analysis of moderately thick composite laminates using the FSDT kinematics (see for instance [3–13]). However, the results are, in most cases, limited to certain lamination schemes and boundary conditions. As far as the study of thick plates with elastically restrained edges is concerned, most of the previous works are limited to isotropic ones ([14–19] among others). But, limited information is found for the case of thick anisotropic laminated plates resting on elastic supports. For instance, Setoodeh and Karami [20] implemented a layer-wise laminated plate theory linked with three-dimensional elasticity approach for vibration and buckling of symmetric and antisymmetric fiber-reinforced composite plates having elastically restraint edges support and results for cross-ply laminates are presented, whereas Karami et al. [21] applied the differential quadrature method for the free vibration

analysis of moderately thick symmetric laminated plates with elastically restrained edges. For the same boundary conditions, semianalytical solutions for the free vibration of angle-ply symmetrically laminated plates were presented by Ashour [22]. Nallim and Grossi [23] also studied the vibration of symmetric laminated plates resting on elastic support employing the Ritz method and beam orthogonal polynomials as approximated functions. These kind of approximate functions (in one or two variables) have been used by many authors to the free vibration analysis of, both homogeneous and nonhomogeneous, plates (Chakraverty et al. [24–26] and Chow et al. [27], among others).

In this paper, a general Ritz formulation for the free vibration analysis of anisotropic laminated plates is developed. All kind of boundary conditions including elastically restrained edges are considered enhancing the study. This feature allows a more realistic analysis of some structural problems. The analysis includes a micromechanical approach (according to the classification of Altenbach et al. [28]), where the average mechanical properties of each anisotropic lamina are estimated from the known characteristics of the fibers and the matrix materials taking into account the fiber volume ratio and the fiber-packing arrangement. At structural level, the dynamic response of the unsymmetrical laminated plate, with elastically restrained edges, is analyzed using the first-order shear deformation theory and the Ritz method with beam orthogonal polynomials as coordinate functions. The approximate analytical solution developed here is very useful to understand, both qualitatively and quantitatively, the behavior of complex laminated plates.

2. Formulation

2.1. Effective Elastic Moduli of Long Fiber-Reinforced Laminae. The micromechanics-based Mori-Tanaka method [29] is used in this section to predict the elastic mechanical properties of the orthotropic unidirectional laminae. This method may be viewed as the simplest mean field approach for inhomogeneous materials that encompass the full physical range of phase volume fraction.

Eshelby's results [33] show that if an elastic homogeneous ellipsoidal inclusion in an infinite linear elastic matrix is subjected to an eigenstrain $\boldsymbol{\varepsilon}^T$, uniform strain states $\boldsymbol{\varepsilon}^C$ is induced, and it is related to the eigenstrain by the expression

$$\boldsymbol{\varepsilon}^C = \mathbf{S}^E : \boldsymbol{\varepsilon}^T, \tag{1}$$

where $\mathbf{S}^E$ is the Eshelby tensor, which depends on the reinforcement dimensions and the Poisson ratio of the matrix ν_m. The components of this tensor for a circular, cylindrical inclusion with an infinite length-to-diameter ratio parallel to the 1-axis (parallel to the fiber direction, Figure 1) are

$$\begin{aligned} S_{1111} &= S_{1133} = S_{1122} = 0, \qquad S_{3333} = S_{2222} = \frac{5-4\nu_m}{8(1-\nu_m)}, \\ S_{3322} &= S_{2233} = \frac{4\nu_m - 1}{8(1-\nu_m)}, \qquad S_{3311} = S_{2211} = \frac{\nu_m}{2(1-\nu_m)}, \\ S_{3232} &= \frac{3-4\nu_m}{8(1-\nu_m)}, \qquad S_{1313} = S_{1212} = \frac{1}{4}. \end{aligned} \tag{2}$$

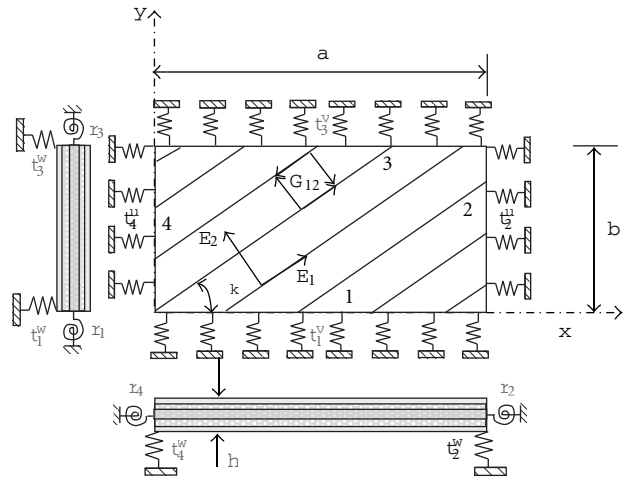

Figure 1: General laminated plate resting on elastic supports.

The transformations strains are obtained considering the equivalent homogeneous inclusion for inhomogeneous inclusions developed by Eshelby [33] together with the interaction effects of Mori-Tanaka [29]. These transformations strains are used to equate the total stresses in the inhomogeneities and their equivalent inclusions, as described in the following equation:

$$\mathbf{C}_f : \left(\boldsymbol{\varepsilon}^a + \boldsymbol{\varepsilon}^{\text{int}} + \boldsymbol{\varepsilon}^C\right) = \mathbf{C}_m : \left(\boldsymbol{\varepsilon}^a + \boldsymbol{\varepsilon}^{\text{int}} + \boldsymbol{\varepsilon}^C - \boldsymbol{\varepsilon}^T\right), \tag{3}$$

where $\mathbf{C}_f$ and $\mathbf{C}_m$ are the stiffness tensors of fiber and matrix, respectively, $\boldsymbol{\varepsilon}^a$ is the uniform far field strain applied to the domain at infinity, and $\boldsymbol{\varepsilon}^{\text{int}}$ is the average elastic strain defined by Mori-Tanaka which is given by

$$\boldsymbol{\varepsilon}^{\text{int}} = -k_f\left(\boldsymbol{\varepsilon}^C - \boldsymbol{\varepsilon}^{\text{T}}\right), \tag{4}$$

where k_f is the fiber volume fraction.

Finally, the stiffness tensor $\mathbf{C}$ for different unidirectional laminae can be obtained from energy considerations [34] and (1) to (4) as

$$\begin{aligned} \mathbf{C} = \mathbf{C}_m \times \Big\{\mathbf{I} - k_f\Big[\left(\mathbf{C}_f - \mathbf{C}_m\right)\left(\mathbf{S}^E - k_f\left(\mathbf{S}^E - \mathbf{I}\right) + \mathbf{C}_m\right)\Big]^{-1} \\ \times \left(\mathbf{C}_f - \mathbf{C}_m\right)\Big\}^{-1}, \end{aligned} \tag{5}$$

where $\mathbf{I}$ is the fourth order identity tensor.

Using this method the mechanical properties of unidirectional carbon/epoxy laminae are found considering various fiber volume fractions, and they are depicted in Table 1. These properties, for each unidirectional lamina, are then used in the next section to obtain the reduced constitutive matrix.

2.2. General Laminated Plate Resting on Elastic Supports. Let us consider a rectangular fiber-reinforced composite laminated plate, of dimension $a \times b$ and total thickness h

Table 1: Mechanical properties of unidirectional laminae (AS4-3501-6), obtained using Mori-Tanaka method. Fiber and matrix properties $E_{f1} = 225\,\text{GPa}$, $E_{f2} = 15\,\text{GPa}$, $G_{f12} = 15\,\text{GPa}$, $G_{f23} = 7\,\text{GPa}$, $\nu_{f12} = 0.20$; $E_m = 4.2\,\text{GPa}$, $\nu_m = 0.34$ ([30]).

k_f	0.1	0.2	0.3	0.4	0.5	0.6	0.7	0.8
E_1	26.29	48.38	70.46	92.54	114.62	136.70	158.78	180.86
E_2	5.11	5.69	6.31	7.01	7.81	8.76	9.87	11.23
$G_{12} = G_{13}$	1.84	2.17	2.57	3.07	3.70	4.54	5.68	7.35
G_{23}	1.75	1.97	2.22	2.52	2.88	3.32	3.88	4.61
n_{12}	0.32	0.31	0.29	0.28	0.27	0.25	0.24	0.23

($h = \sum h_k$, h_k represents the thickness of a layer). The laminated plate is composed of an arbitrary number of N_c orthotropic layers and fibre orientation β_k ($k = 1, 2, \ldots, N_c$) as shown in Figure 1. A rectangular Cartesian coordinate system (x, y, z) is used to represent the plate geometry and the strain–displacement relations. The x-y plane coincides with the middle plane of the plate. The displacement field of the first-order shear deformation theory is assumed to be of the form [1, 2]

$$\begin{aligned} u(x,y,z,t) &= u_0(x,y,t) + z\phi_x(x,y,t), \\ v(x,y,z,t) &= v_0(x,y,t) + z\phi_y(x,y,t), \\ w(x,y,z,t) &= w_0(x,y,t), \end{aligned} \tag{6}$$

where t is the time dimension u_0, v_0 and w_0 denote the mid-surface translational displacements along the x, y, and z axes, and ϕ_x, ϕ_y are the rotations about y- and x-axes, respectively. The displacement model (6) yields the following kinematic relations:

$$\{\varepsilon\} = \begin{bmatrix} \{\varepsilon_0\} \\ \{\varepsilon_0^*\} \end{bmatrix} + z \begin{bmatrix} \{\varepsilon_1\} \\ \{0\} \end{bmatrix}, \tag{7}$$

where

$$\begin{aligned} \{\varepsilon\}^T &= \left\{\varepsilon_x, \varepsilon_y, \gamma_{xy}, \gamma_{yz}, \gamma_{xz}\right\}, \\ \{\varepsilon_0\}^T &= \left\{\frac{\partial u_0}{\partial x}, \frac{\partial v_0}{\partial y}, \frac{\partial u_0}{\partial y} + \frac{\partial v_0}{\partial x}\right\}, \\ \{\varepsilon_0^*\}^T &= \left\{\frac{\partial w_0}{\partial y} + \phi_y, \frac{\partial w_0}{\partial x} + \phi_x\right\}, \\ \{\varepsilon_1\}^T &= \left\{\frac{\partial \phi_x}{\partial x}, \frac{\partial \phi_y}{\partial y}, \frac{\partial \phi_x}{\partial y} + \frac{\partial \phi_y}{\partial x}\right\}. \end{aligned} \tag{8}$$

The stress-strain relation of each layer is given by the generalized Hooke's law as follows:

$$\begin{pmatrix} \sigma_x \\ \sigma_y \\ \tau_{xy} \\ \tau_{yz} \\ \tau_{xz} \end{pmatrix}^{(k)} = \begin{bmatrix} \overline{Q}_{11} & \overline{Q}_{12} & \overline{Q}_{16} & 0 & 0 \\ \overline{Q}_{12} & \overline{Q}_{22} & \overline{Q}_{26} & 0 & 0 \\ \overline{Q}_{16} & \overline{Q}_{26} & \overline{Q}_{66} & 0 & 0 \\ 0 & 0 & 0 & \overline{Q}_{44} & \overline{Q}_{45} \\ 0 & 0 & 0 & \overline{Q}_{45} & \overline{Q}_{55} \end{bmatrix}^{(k)} \begin{bmatrix} \varepsilon_x \\ \varepsilon_y \\ \gamma_{xy} \\ \gamma_{yz} \\ \gamma_{xz} \end{bmatrix}, \tag{9}$$

where $\overline{Q}_{ij}$ are the components of the plane-stress reduced constitutive matrix [35] which are function of the elastic constant determined in Section 2.1 and the ply angle β_k.

2.3. Energy Functional Components. Taking into account (7) and (9), the strain energy due to the laminated plate deflection can be written as

$$\begin{aligned} U_p = \frac{1}{2}\iint_R \Big[&\{\varepsilon_0\}[A]\{\varepsilon_0\}^T + \{\varepsilon_0\}[B]\{\varepsilon_1\}^T + \{\varepsilon_1\}[B]\{\varepsilon_0\}^T \\ &+ \{\varepsilon_1\}[D]\{\varepsilon_1\}^T + \{\varepsilon_0^*\}[A^*]\{\varepsilon_0^*\}^T \Big] dx\,dy, \end{aligned} \tag{10}$$

where R is the mid-surface area (Figure 1) and the stiffness coefficients [35, 36] are given by $(A_{ij}, B_{ij}, D_{ij}) = \int_{-h/2}^{h/2} \overline{Q}_{ij}(1, z, z^2)dz$ $(i, j = 1, 2, 6)$, $A_{ij}^* = \int_{-h/2}^{h/2} k_{ij}\overline{Q}_{ij}dz$ $(i, j = 4, 5)$ k_{ij} being the shear correction factors.

The strain energy corresponding to the elastic edge restraints is given by

$$\begin{aligned} U_t = \frac{1}{2}\int_0^a \Big[&t_1^w \left(w_0|_{y=0}\right)^2 + t_3^w \left(w_0|_{y=b}\right)^2 + t_1^v \left(v_0|_{y=0}\right)^2 \\ &+ t_3^v \left(v_0|_{y=b}\right)^2 + r_1 \left(\phi_y|_{y=0}\right)^2 + r_3 \left(\phi_y|_{y=b}\right)^2 \Big] dx \\ + \frac{1}{2}\int_0^b \Big[&t_2^w (w_0|_{x=a})^2 + t_4^w (w_0|_{x=0})^2 + t_2^u (v_0|_{x=a})^2 \\ &+ t_4^u (v_0|_{x=0})^2 + r_2 (\phi_x|_{x=a})^2 + r_4 \left(\phi_x|_{y=0}\right)^2 \Big] dy, \end{aligned} \tag{11}$$

where $t_i^\bullet$ ($i = 1, \ldots, 4$ and $\bullet = u, v, w$) are the elastic translational coefficients and r_i ($i = 1, \ldots, 4$) are the elastic rotational coefficients.

The kinetic energy is expressed as

$$\begin{aligned} T = \frac{1}{2}\iint_R \Big[&I_0(\dot{u}_0^2 + \dot{v}_0^2 + \dot{w}_0^2) + 2I_1\left(\dot{u}_0\dot{\phi}_x + \dot{v}_0\dot{\phi}_y\right) \\ &+ I_2\left(\dot{\phi}_x^2 + \dot{\phi}_y^2\right) \Big] dx\,dy, \end{aligned} \tag{12}$$

being I_i ($i = 0, 1, 2$) the mass inertias of the plate defined as [35]

$$I_i = \int_{-h/2}^{h/2} \rho^{(k)} z^i dz, \quad (i = 0, 1, 2), \tag{13}$$

where $\rho^{(k)}$ is the material density of the k-th layer.

3. Application of the Ritz Method for the Free Vibration Analysis

The Ritz method is applied to determine analytical approximate solutions for dynamical behavior of arbitrarily laminated plates resting on elastic supports. During free vibration, the displacements components are assumed split in

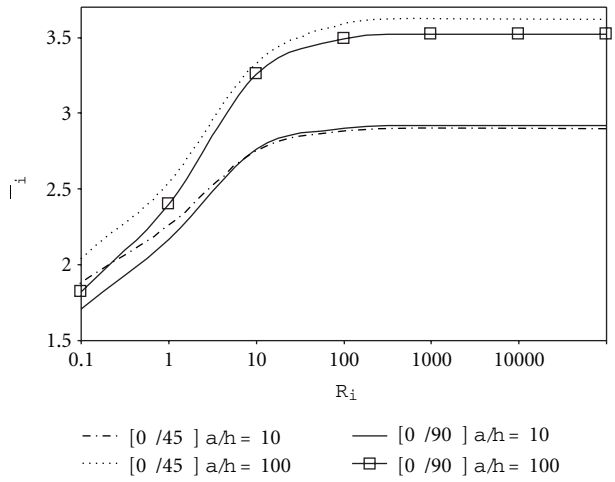

Figure 2: Variation of the fundamental frequency coefficient $\overline{\omega}$ with the rotational restraint parameter R_i, $T_i^w = T_i^u = T_i^v = \infty$ ($i = 1,\ldots,4$) for square [0°/45°] and [0°/90°] carbon-epoxy (Table 1), with $k_f = 0.6$.

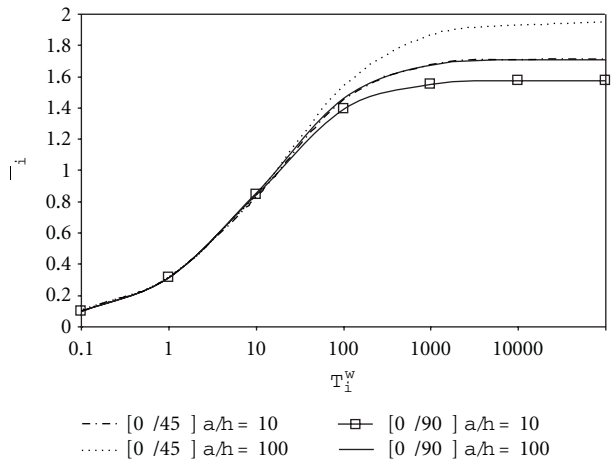

Figure 3: Variation of the fundamental frequency coefficient $\overline{\omega}$ with the translational restraint parameter T_i^w, $T_i^u = T_i^v = R_i = 0$ ($i = 1,\ldots,4$) for square [0°/45°] and [0°/90°] carbon-epoxy (Table 1), with $k_f = 0.6$.

the spatial and temporal parts, being the last one periodic in time; that is,

$$\begin{aligned} u_0(x,y,t) &= U(x,y)\sin\omega t, \\ v_0(x,y,t) &= V(x,y)\sin\omega t, \\ w_0(x,y,t) &= W(x,y)\sin\omega t, \\ \phi_x(x,y,t) &= \Phi_x(x,y)\sin\omega t, \\ \phi_y(x,y,t) &= \Phi_y(x,y)\sin\omega t, \end{aligned} \tag{14}$$

where ω is the natural frequency in radian.

Putting these displacements into the energy functional components ((10) to (12)) the maximum values of the kinetic

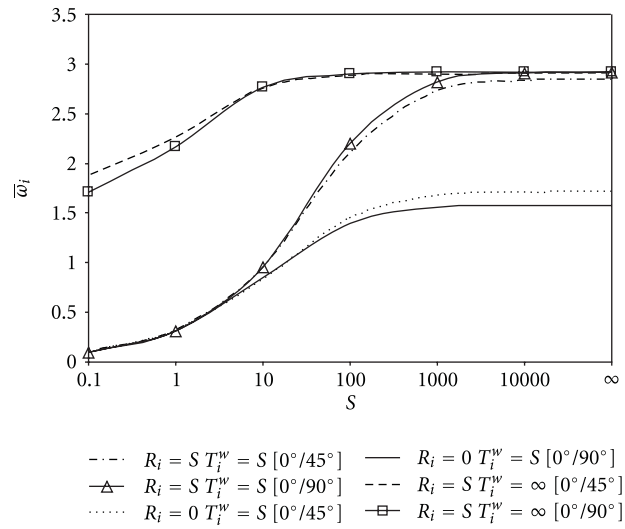

Figure 4: Variation of the fundamental frequency coefficient $\overline{\omega}$ with the translational and the rotational restraint parameters $T_i^w = R_i$, $T_i^u = T_i^v = 0$ ($i = 1,\ldots,4$) for square [0°/45°] and [0°/90°] carbon-epoxy (Table 1), with $k_f = 0.6$ and $a/h = 10$.

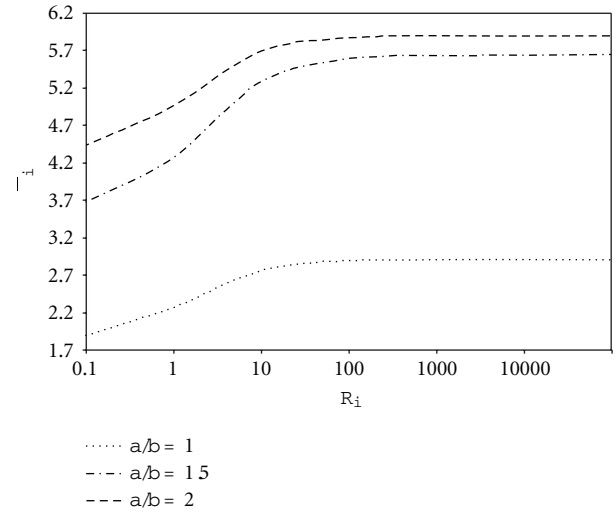

Figure 5: Variation of the fundamental frequency coefficient $\overline{\omega}$ with the rotational restraint parameter R_i, $T_i^w = T_i^u = T_i^v = \infty$ ($i = 1,\ldots,4$) for different aspect ratios [0°/45°] carbon-epoxy (Table 1), with $k_f = 0.6$.

energy ($T_{\max}$) and the strain energies ($U_{p,\max}, U_{t,\max}$) are derived. Then, the energy functional for free vibration of the laminated plate is given by

$$\Pi = U_{p,\max} + U_{t,\max} - T_{\max}, \tag{15}$$

which is to be minimized according to the Ritz principle.

3.1. Boundary Conditions and Approximating Functions. There are some options when choosing the unknown functions of displacement components to apply the Ritz method. Particularly, the use of orthogonal polynomials as coordinate

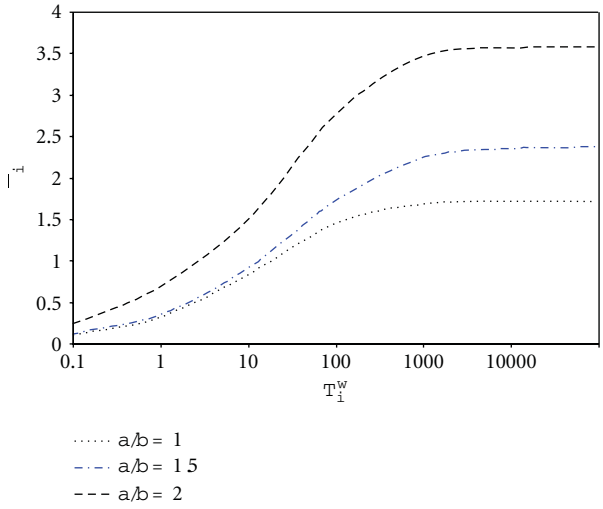

Figure 6: Variation of the fundamental frequency coefficient $\overline{\omega}$ with the translational restraint parameter T_i^w, $T_i^u = T_i^v = R_i = 0$ $(i = 1, \ldots, 4)$ for different aspect ratios $[0°/45°]$ carbon-epoxy (Table 1), with $k_f = 0.6$.

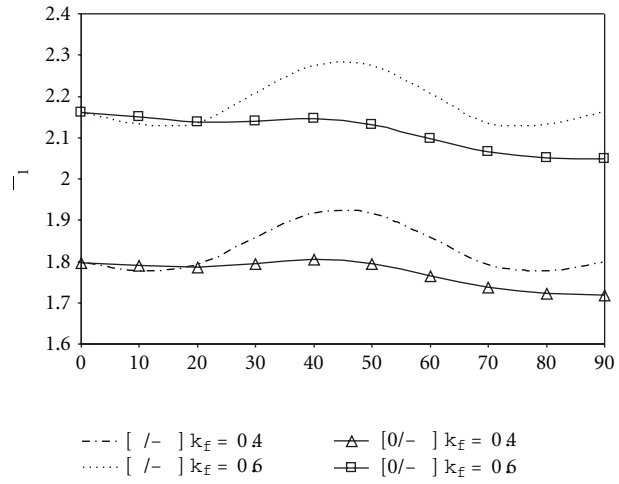

Figure 7: Effect of the fiber orientation on the first vibration frequency coefficient $\overline{\omega}_1$, for two different fiber volume fraction k_f with $C_1C_1C_1C_1$ boundary condition and $a/h = 10$.

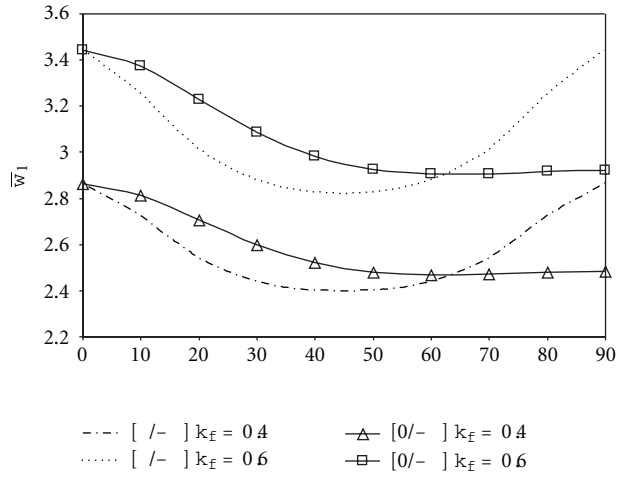

Figure 8: Effect of the fiber orientation on the first vibration frequency coefficient $\overline{\omega}_1$, for two different fiber volume fraction k_f with $S_1S_1S_1S_1$ boundary condition and $a/h = 10$.

functions has important advantages related to numerical stability and fast convergence as has been demonstrated in previous works [23, 37, 38], even for plates with complicated boundary conditions and high degree of anisotropy. For these reasons, in this work, the displacement components are expressed by sets of beam characteristic orthogonal polynomials $\{p_i^{(\cdot)}(x)\}$, $\{q_j^{(\bullet)}(y)\}$, $(\bullet) = u, v, w, \phi_x, \phi_y$, resulting in

$$U(x,y) \approx U_{MN}(x,y) = \sum_{i=1}^{M}\sum_{j=1}^{N} c_{ij}^{(u)} p_i^{(u)}(x)\, q_j^{(u)}(y),$$

$$V(x,y) \approx V_{MN}(x,y) = \sum_{i=1}^{M}\sum_{j=1}^{N} c_{ij}^{(v)} p_i^{(v)}(x)\, q_j^{(v)}(y),$$

$$W(x,y) \approx W_{MN}(x,y) = \sum_{i=1}^{M}\sum_{j=1}^{N} c_{ij}^{(w)} p_i^{(w)}(x)\, q_j^{(w)}(y),$$

$$\Phi_x \approx \Phi_{xMN}(x,y) = \sum_{i=1}^{N}\sum_{j=1}^{M} c_{ij}^{(\phi_x)} p_i^{(\phi_x)}(x)\, q_j^{(\phi_x)}(y),$$

$$\Phi_y \approx \Phi_{yMN}(x,y) = \sum_{i=1}^{N}\sum_{j=1}^{M} c_{ij}^{(\phi_y)} p_i^{(\phi_y)}(x)\, q_j^{(\phi_y)}(y), \tag{16}$$

where $c_{ij}^{(u)}$, $c_{ij}^{(v)}$, $c_{ij}^{(w)}$, $c_{ij}^{(\phi_x)}$, $c_{ij}^{(\phi_y)}$ are the unknown coefficients, and M, N are the numbers of polynomials in each coordinate.

The procedure for the construction of the orthogonal polynomials has been developed by Bhat [39]. The first members of the sets, $p_1^{(\bullet)}(x)$ and $q_1^{(\bullet)}(y)(\bullet) = u, v, w, \phi_x, \phi_y$ are obtained as the simplest polynomials that satisfy all the geometrical boundary conditions of the plate in their respective x and y directions. The higher members of each set are constructed by employing the Gram-Schmidt orthogonalization procedure. The coefficients of the polynomials are chosen in such a way as to make the polynomials orthonormal. However, the functions $p_k^{(\bullet)}(x)$ and $q_k^{(\bullet)}(y)$ for $(\bullet) = \phi_x, \phi_y$ are obtained from relative rotation conditions starting from polynomials of an order lower than the chosen for the transversal displacements and then applying the sequence of Gram-Schmidt orthogonalization procedure. This particular choice is made to avoid the overestimation of the rate of elastic energy due to the shear respect to the rate due to the bending. This concept has been applied by Auciello and Ercolano [40], to Timoshenko beams, to avoid

Table 2: Notations for various combinations of boundary conditions, in which n and s indicate the directions normal and tangential to the respective plate edges.

	In-plane constraints			
Transverse constraints	$u_n = 0, u_s = 0$	$N_n = 0, u_s = 0$	$u_n = 0, N_{ns} = 0$	$N_n = 0, N_{ns} = 0$
Clamped: $w = 0; \phi_n = 0$	C_1	C_2	C_3	C_4
Simply supported: $w = 0; M_n = 0; \phi_s = 0$	S_1	S_2	S_3	S_4
Free: $M_n = 0; M_{ns} = 0; Q_n = 0$	F_1	F_2	F_3	F_4

Table 3: Convergence study of frequencies $\omega_i^* = \omega_i a^2\sqrt{\rho/(E_2h^2)}$ for a two-layered $[0^\circ/45^\circ]$ square plate. $E_1/E_2 = 25$, $G_{12} = G_{13} = 0.5E_2$, $G_{23} = 0.2E_2$, $\nu_{12} = 0.25$.

a/h	M, N	Mode sequence number					
	$(M = N)$	1	2	3	4	5	6
10	4	15.487	23.582	30.182	35.243	42.217	49.098
	5	15.480	23.401	30.005	33.514	38.099	44.303
	6	15.478	23.359	29.960	33.217	37.825	43.331
	7	15.478	23.356	29.957	33.112	37.691	42.997
	8	15.478	23.356	29.956	33.104	37.679	42.901
	9	15.478	23.356	29.956	33.103	37.676	42.889
	10	15.478	23.356	29.956	33.103	37.675	42.887
	Shi et al. [5]	15.504	23.399	29.991	33.170	37.740	42.973
20	4	19.248	30.947	42.338	50.788	71.618	81.985
	5	19.227	30.415	41.788	46.288	54.225	64.750
	6	19.221	30.279	41.586	45.434	53.531	62.080
	7	19.219	30.271	41.572	45.047	53.090	61.032
	8	19.219	30.268	41.569	45.016	53.047	60.655
	9	19.218	30.267	41.569	45.008	53.032	60.600
	10	19.218	30.267	41.568	45.007	53.030	60.587
	Shi et al. [5]	19.350	30.490	41.769	45.400	53.385	61.035
100	4	21.348	36.366	52.130	65.773	298.228	304.052
	5	21.314	35.002	50.893	56.783	68.251	86.403
	6	21.291	34.676	50.155	54.927	66.919	79.733
	7	21.289	34.660	50.124	53.854	65.602	76.972
	8	21.288	34.655	50.107	53.792	65.504	75.800
	9	21.288	34.654	50.106	53.757	65.449	75.631
	10	21.288	34.654	50.106	53.754	65.444	75.553
	Shi et al. [5]	21.802	35.692	51.304	55.298	67.257	77.843

Table 4: Comparison of fundamental frequency coefficient $\omega_i^* = \omega_i a^2\sqrt{\rho/(E_2h^2)}$ for a four layered $[45^\circ/-45^\circ/45^\circ/-45^\circ]$ plate with different aspect ratios a/b. $E_1/E_2 = 40$, $G_{12} = 0.6E_2$, $G_{13} = G_{23} = 0.5E_2$, $\nu_{12} = 0.25$.

a/h		a/b						
		0.2	0.6	0.8	1	1.2	1.6	2
10	Present	9.013	13.02	15.74	18.62	21.59	27.66	34.57
	Alibeigloo et al. [31]	8.559	12.565	15.187	17.983	20.895	27.031	33.634
	Redy [32]	8.724	12.965	15.712	18.609	21.567	27.736	34.247
30	Present	9.965	15.409	19.293	23.638	28.377	39.062	51.480
	Alibeigloo et al. [31]	9.420	14.790	18.487	22.637	27.200	37.534	49.499
	Redy [32]	9.667	15.385	19.304	23.676	28.381	38.940	51.132
50	Present	10.056	15.66	19.70	24.25	29.25	40.70	54.25
	Alibeigloo et al. [31]	9.5016	15.0261	18.8586	23.195	28.003	39.05	52.686
	Redy [32]	9.816	15.689	19.759	24.343	29.321	40.653	53.989

Table 5: (a) Frequency parameters $\overline{\omega}_i$ for [0°/45°]and [0°/90°] carbon-epoxy AS4-3501-6 (Table 1), with different translational restraint parameter T_i^w, $T_i^u = T_i^v = R_i = 0$ ($i = 1, \ldots, 4$), and $a/h = 10$. (b) Frequency parameters $\overline{\omega}_i$ for [0°/45°] and [0°/90°] carbon-epoxy AS4-3501-6 (Table 1), with different translational restraint parameter T_i^w, $T_i^u = T_i^v = R_i = 0$ ($i = 1, \ldots, 4$), and $a/h = 100$.

(a)

k_f	Mode	Translational restraint parameter T_i^w						
		0.1	1	10	100	1000	10000	$1.00E+10$
				$a/h = 10$				
	[0°/45°]							
0.2	1	0.060	0.187	0.520	0.969	1.161	1.191	1.195
	2	0.085	0.266	0.803	1.827	2.380	2.470	2.481
	3	0.085	0.267	0.822	2.079	2.930	3.063	3.078
	4	0.754	0.810	1.224	2.609	3.776	4.004	4.032
0.4	1	0.083	0.256	0.689	1.219	1.419	1.448	1.452
	2	0.117	0.367	1.083	2.284	2.829	2.912	2.922
	3	0.117	0.368	1.125	2.723	3.638	3.767	3.782
	4	0.890	0.978	1.590	3.325	4.530	4.735	4.759
0.6	1	0.101	0.310	0.824	1.443	1.671	1.705	1.709
	2	0.142	0.445	1.303	2.685	3.290	3.382	3.393
	3	0.142	0.447	1.364	3.274	4.342	4.492	4.509
	4	1.040	1.151	1.903	3.936	5.292	5.517	5.543
	[0°/90°]							
0.2	1	0.060	0.188	0.528	0.942	1.084	1.104	1.106
	2	0.085	0.267	0.814	1.970	2.657	2.756	2.768
	3	0.085	0.267	0.814	1.970	2.657	2.756	2.768
	4	0.628	0.697	1.164	2.642	3.708	3.888	3.909
0.4	1	0.083	0.258	0.705	1.181	1.321	1.340	1.342
	2	0.117	0.368	1.110	2.546	3.251	3.344	3.355
	3	0.117	0.368	1.110	2.546	3.251	3.344	3.355
	4	0.750	0.858	1.540	3.424	4.519	4.675	4.675
0.6	1	0.101	0.313	0.847	1.395	1.553	1.574	1.577
	2	0.142	0.446	1.343	3.035	3.829	3.932	3.944
	3	0.142	0.446	1.343	3.035	3.829	3.932	3.944
	4	0.910	1.040	1.864	4.089	5.329	5.514	5.536

(b)

k_f	Mode	Translational restraint parameter T_i^w						
		0.1	1	10	100	1000	10000	$1.00E+10$
				$a/h = 100$				
	[0°/45°]							
0.2	1	0.060	0.187	0.525	1.014	1.276	1.329	1.340
	2	0.085	0.268	0.813	1.928	2.708	2.881	2.908
	3	0.085	0.269	0.832	2.214	3.489	3.771	3.815
	4	0.804	0.858	1.266	2.774	4.519	5.027	5.098
0.4	1	0.083	0.256	0.697	1.292	1.577	1.633	1.646
	2	0.117	0.369	1.099	2.445	3.269	3.440	3.468
	3	0.117	0.370	1.142	2.952	4.444	4.746	4.794
	4	0.947	1.032	1.642	3.588	5.531	6.011	6.073
0.6	1	0.101	0.310	0.835	1.531	1.859	1.925	1.940
	2	0.142	0.447	1.324	2.880	3.804	3.995	4.028
	3	0.143	0.450	1.385	3.555	5.304	5.654	5.711
	4	1.104	1.210	1.962	4.255	6.457	6.980	7.046

(b) Continued.

k_f	Mode	Translational restraint parameter T_i^w						
		0.1	1	10	100	1000	10000	$1.00E+10$
	$[0°/90°]$							
0.2	1	0.060	0.188	0.533	0.981	1.161	1.190	1.194
	2	0.085	0.268	0.823	2.086	3.043	3.212	3.233
	3	0.085	0.268	0.823	2.086	3.043	3.212	3.233
	4	0.666	0.732	1.197	2.805	4.365	4.732	4.782
0.4	1	0.083	0.258	0.714	1.239	1.422	1.449	1.453
	2	0.117	0.370	1.126	2.738	3.783	3.948	3.969
	3	0.117	0.370	1.126	2.738	3.783	3.948	3.969
	4	0.797	0.901	1.583	3.699	5.418	5.774	5.821
0.6	1	0.101	0.313	0.857	1.464	1.674	1.706	1.710
	2	0.143	0.449	1.363	3.271	4.453	4.638	4.661
	3	0.143	0.449	1.363	3.271	4.453	4.638	4.661
	4	0.967	1.093	1.917	4.427	6.392	6.797	6.851

the shear locking effect and is extended here for laminated plates.

The classical boundary conditions considered in this study are depicted in Table 2. By keeping in mind that in the Ritz method only the geometric boundary conditions need to be satisfied, it is possible to work with any sets of required edge boundary condition and also is very simple the consideration of elastically restrained edges where there are not essential boundary conditions to satisfy.

Upon inserting the displacement forms (16) into the energy functional of the system (15), the minimization with respect to the coefficients of the displacement functions is given by

$$\frac{\partial \Pi}{\partial c_{ij}^{(u)}} = 0, \qquad \frac{\partial \Pi}{\partial c_{ij}^{(v)}} = 0, \qquad \frac{\partial \Pi}{\partial c_{ij}^{(w)}} = 0,$$
$$\frac{\partial \Pi}{\partial c_{ij}^{(\phi_x)}} = 0, \qquad \frac{\partial \Pi}{\partial c_{ij}^{(\phi_y)}} = 0. \tag{17}$$

From (17) a set of algebraic simultaneous equations is obtained. The number of these equations becomes $5 \times M \times N$. The algebraic equations obtained are given as follows, in the form of the generalized eigenvalue problem:

$$(\mathbf{K} - \omega^2 \mathbf{M})\{\mathbf{C}\} = \{\mathbf{0}\}, \tag{18}$$

where $\mathbf{K}$ and $\mathbf{M}$ are stiffness and inertia matrices, respectively (their expressions are given in the Appendix, $\{\mathbf{C}\}$ contains the unknown coefficients of (16).

For a nontrivial solution, the eigenvalues which make the determinant equal to zero, correspond to the free vibration frequencies.

4. Verification of the Formulation and Numerical Applications

4.1. General Description. The variational algorithm developed in this paper was programmed in Fortran language and used for the free vibration analysis of generally laminated thin and moderately thick laminated plates having different geometric parameters, stacking sequences, material properties, fiber volume fractions, and boundary conditions. The examples considered in this study are confined to laminates with layers of equal thickness, even though the procedure was formulated for plies with arbitrary thickness. In all cases the shear correction factor was taken a 5/6.

Let us introduce the terminology to be used throughout the remainder of the paper for describing the boundary conditions of the considered plates. The designation $C_iS_iF_iS_i$, for example, identifies a plate with edges (1) clamped, (2) simply supported, (3) free, and (4) simply supported (see Figure 1) the subscript i ($i = 1,\ldots,4$) identifies the in-plane constraints according to Table 2. When the edges are elastically restrained against rotation or translation, the following nondimensional restraint parameters are used

$$T_i^{\bullet} = \frac{a^3 t_i^{\bullet}}{D_0}, \quad (i = 1,\ldots,4 \text{ and } \bullet = u, v, w),$$
$$R_i = \frac{r_i a}{D_0}, \quad (i = 1,\ldots,4), \tag{19}$$

where $D_0 = E_1 h^3/12(1 - \nu_{12}\nu_{21})$.

The main purposes of the numerical applications presented in this section are twofold. One is to demonstrate the accuracy, the flexibility, and the efficiency of the proposed method and the other is to produce some results which may be regarded as benchmark solutions for other academic research workers and design engineers.

4.2. Validation and Convergence Studies. The accuracy and reliability of the results obtained with the present approach are next demonstrated by comparing them with some selected values published by Shi et al. [5] for moderately thick ($a/h = 10, 20$) and thin ($a/h = 100$) arbitrarily clamped laminated plates. The comparison presented in Table 3 authenticates the validity of the present method for arbitrarily laminated plates. Very close agreement for the first

Table 6: (a) Frequency parameters $\overline{\omega}_i$ for [0°/45°] and [0°/90°] carbon-epoxy AS4-3501-6 (Table 1), with different rotational restraint parameter R_i, $T_i^w = T_i^u = T_i^v = \infty$ ($i = 1,..,4$), and $a/h = 10$. (b) Frequency parameters $\overline{\omega}_i$ for [0°/45°] and [0°/90°] carbon-epoxy AS4-3501-6 (Table 1), with different rotational restraint parameter R_i, $T_i^w = T_i^u = T_i^v = \infty$ ($i = 1,..,4$), and $a/h = 100$.

(a)

k_f	Mode	Rotational restraint parameter R_i						
		0.1	1	10	100	1000	10000	$1.00E+10$
				$a/h = 10$				
	[0°/45°]							
0.2	1	1.461	1.623	1.943	2.056	2.071	2.072	2.072
	2	2.709	2.903	3.268	3.390	3.406	3.407	3.407
	3	3.350	3.497	3.861	4.010	4.030	4.032	4.032
	4	4.322	4.477	4.818	4.951	4.969	4.971	4.971
0.4	1	1.837	2.029	2.371	2.483	2.497	2.498	2.498
	2	3.249	3.493	3.875	3.988	4.002	4.003	4.003
	3	4.112	4.302	4.709	4.854	4.872	4.874	4.874
	4	5.129	5.333	5.700	5.823	5.838	5.840	5.840
0.6	1	2.182	2.408	2.803	2.931	2.947	2.949	2.949
	2	3.799	4.090	4.527	4.654	4.669	4.671	4.671
	3	4.884	5.119	5.611	5.783	5.804	5.806	5.807
	4	5.987	6.239	6.672	6.812	6.830	6.832	6.832
	[0°/90°]							
0.2	1	1.386	1.562	1.916	2.034	2.048	2.050	2.050
	2	2.901	3.110	3.561	3.719	3.738	3.740	3.741
	3	2.901	3.110	3.561	3.719	3.738	3.740	3.741
	4	4.052	4.287	4.764	4.970	4.994	4.996	4.996
0.4	1	1.755	1.969	2.352	2.468	2.482	2.483	2.483
	2	3.532	3.814	4.321	4.473	4.491	4.493	4.493
	3	3.532	3.814	4.321	4.473	4.491	4.493	4.493
	4	4.932	5.218	5.745	5.949	5.971	5.973	5.973
0.6	1	2.090	2.340	2.776	2.905	2.920	2.922	2.922
	2	4.167	4.511	5.102	5.272	5.292	5.294	5.295
	3	4.167	4.511	5.102	5.272	5.292	5.294	5.295
	4	5.833	6.179	6.790	7.021	7.045	7.047	7.048

(b)

k_f	Mode	Rotational restraint parameter R_i						
		0.1	1	10	100	1000	10000	$1.00E+10$
				$a/h = 100$				
	[0°/45°]							
0.2	1	1.598	1.814	2.318	2.534	2.564	2.567	2.567
	2	3.108	3.410	4.115	4.415	4.457	4.461	4.462
	3	4.161	4.421	5.275	5.759	5.831	5.839	5.840
	4	5.366	5.689	6.611	7.100	7.173	7.181	7.181
0.4	1	2.044	2.316	2.901	3.135	3.166	3.169	3.170
	2	3.783	4.185	4.997	5.311	5.353	5.358	5.358
	3	5.265	5.627	6.699	7.240	7.317	7.325	7.326
	4	6.450	6.911	8.018	8.523	8.594	8.601	8.602
0.6	1	2.428	2.748	3.423	3.689	3.725	3.729	3.729
	2	4.418	4.896	5.821	6.171	6.217	6.222	6.223
	3	6.250	6.692	7.967	8.593	8.682	8.691	8.692
	4	7.498	8.058	9.337	9.897	9.974	9.983	9.983

(b) Continued.

k_f	Mode	Rotational restraint parameter R_i						
		0.1	1	10	100	1000	10000	$1.00E+10$
	$[0°/90°]$							
0.2	1	1.493	1.719	2.223	2.413	2.437	2.440	2.440
	2	3.396	3.720	4.583	4.960	5.010	5.016	5.016
	3	3.396	3.720	4.583	4.960	5.010	5.016	5.016
	4	5.036	5.390	6.396	6.966	7.039	7.047	7.048
0.4	1	1.917	2.203	2.780	2.976	3.001	3.003	3.003
	2	4.202	4.665	5.725	6.122	6.172	6.178	6.178
	3	4.202	4.665	5.725	6.122	6.172	6.178	6.178
	4	6.173	6.688	7.937	8.560	8.634	8.641	8.642
0.6	1	2.286	2.621	3.277	3.494	3.521	3.523	3.524
	2	4.952	5.515	6.745	7.185	7.241	7.247	7.247
	3	4.952	5.515	6.745	7.185	7.241	7.247	7.247
	4	7.297	7.918	9.364	10.060	10.141	10.149	10.150

sixth nondimensional frequencies $\omega_i^* = \omega_i a^2\sqrt{\rho/(E_2h^2)}$ is obtained for all cases and display monotonic convergence tendency to constant values. For thick plates, as shown in Table 3, as number of N and M is increased from 7 to 10, the frequency parameter decreases merely 0.002% for the first mode and 0.26% for the sixth. For thin plates the relative decreases of the frequency parameters are 0.004% for the first mode and 1.88% for the sixth as the numbers of polynomials M, N are increased from 7 to 10, exhibiting slower convergence rate than that of moderately thick plates. Consequently the number of beam characteristic polynomials used in the following computations for thin and thick plates is chosen as $M = N = 7$.

The validation of the proposed methodology for different aspect ratios (a/b) is presented in Table 4, showing a good agreement with Alibeigloo et al. [31] and Reddy [32].

4.3. Numerical Results and Discussion. Several examples including new results for arbitrarily laminated plates with elastically restrained edges are presented in this section. The elastic properties of the composite materials used here are those shown in Table 1. The influence of different values of fiber volume ratios (k_f) is analyzed in several figures and tables.

Values of the first four frequency parameters $\overline{\omega}_i = \omega_i(a^2/h)\sqrt{\rho/E_{f1}}$ for square thick ($a/h = 10$) and thin ($a/h = 100$) unsymmetric laminated plates are shown for increasing values of the translational restraint parameter T_i^w, in Tables 5(a) and 5(b). Moreover, the influence of rotational restraint parameter R_i in the free vibration frequency coefficients is shown in Tables 6(a) and 6(b).

In Figures 2–4 the fundamental frequency coefficients $\overline{\omega}$ corresponding to two laminated square plates are plotted against the restraint parameters R_i and T_i^w. Figure 2 shows the variation of $\overline{\omega}$ for various values of the rotational restraint R_i, while Figure 3 shows the variation of $\overline{\omega}$ for various values of the translational restraint T_i^w. A major increase of frequency occurs when the elastic restraint values are in the interval 0.1–50. Figure 4 shows the variation of $\overline{\omega}$ for various values of the rotational and translational restraint parameters: (a) $R_i = 0$, $T_i^w = S$; (b) $R_i = S$, $T_i^w = \infty$, and (c) $R_i = T_i^w = S$. The obtained curves illustrate the restraint parameters intervals for which the frequency coefficient $\overline{\omega}$ is sensitive to R_i and T_i^w.

To asses the influence of the aspects ratio a/b in the laminated plate response, values of the first four frequency parameters $\overline{\omega}_i = \omega_i(a^2/h)\sqrt{\rho/E_{f1}}$ for rectangular thick ($a/h = 10$) unsymmetric laminated plates are shown, for increasing values of the translational restraint parameter T_i^w (Table 7(a)) and the rotational restraint parameter R_i (Table 7(b)) considering $a/b = 1.5$ and $a/b = 2$.

Figure 5 shows the variation of $\overline{\omega}$ for various values of the rotational restraint R_i, while Figure 6 shows the variation of $\overline{\omega}$ for various values of the translational restraint T_i^w for rectangular laminated plates.

To evaluate the effect of different fiber orientation angles (β) and fiber volume fraction on the dynamic properties of the laminates, the variation of the first free vibration coefficient $\overline{\omega}_1$ is plotted in Figures 7 and 8, considering two lamination stacking sequences, $[\beta/-\beta]$ and $[0/\beta]$. Two boundary conditions have been included, $C_1C_1C_1C_1$ in Figure 7 and $S_1S_1S_1S_1$ in Figure 6. It is observed that the $[\beta/-\beta]$ laminate is more sensitive to the fiber orientation angle than $[0/\beta]$ lamination scheme. The adimensional frequency parameter is noticeable higher as the fiber volume fraction k_f increases and as the boundary conditions become clamped.

Finally, the first four free vibration coefficients are presented in Table 8 to illustrate the influence of various fiber volume fractions and boundary conditions on the dynamical behavior of an unsymmetric $[0°/45°]$ laminated plate.

5. Concluding Remarks

A Ritz approach for free vibration analysis of general laminated plates with edges elastically restrained against translation and rotation is presented in this work. The study

Table 7: (a) Frequency parameters $\overline{\omega}_i$ for [0°/45°] carbon-epoxy AS4-3501-6 (Table 1), with different translational restraint parameter T_i^w, $T_i^u = T_i^v = R_i = 0$ ($i = 1,..,4$), and $a/h = 10$. (b) Frequency parameters $\overline{\omega}_i$ for [0°/45°] carbon-epoxy AS4-3501-6 (Table 1), with different rotational restraint parameter R_i, $T_i^w = T_i^u = T_i^v = \infty$ ($i = 1,\ldots,4$), and $a/h = 10$.

(a)

k_f	Mode	Translational restraint parameter T_i^w						
		0.1	1	10	100	1000	10000	$1.00E+10$
				$a/b = 2$				
0.2	1	0.158	0.464	1.043	2.045	2.778	2.903	2.917
	2	0.184	0.574	1.625	3.592	4.520	4.704	4.726
	3	0.255	0.793	2.167	3.948	6.915	7.139	7.149
	4	1.652	1.823	2.838	5.127	7.177	7.419	7.449
0.4	1	0.199	0.578	1.268	2.392	3.046	3.144	3.156
	2	0.233	0.723	1.999	4.175	5.024	5.169	5.186
	3	0.322	0.999	2.649	4.774	7.759	8.125	8.148
	4	1.832	2.071	3.374	6.021	7.973	8.173	8.196
0.6	1	0.235	0.681	1.487	2.757	3.455	3.557	3.569
	2	0.275	0.853	2.347	4.837	5.763	5.915	5.933
	3	0.380	1.179	3.115	5.589	8.864	9.309	9.342
	4	2.104	2.394	3.945	6.992	9.186	9.408	9.434
				$a/b = 1.5$				
0.2	1	0.111	0.341	0.904	1.724	2.239	2.345	2.364
	2	0.141	0.443	1.335	3.326	4.739	5.023	5.067
	3	0.171	0.539	1.627	3.705	5.946	6.580	6.673
	4	1.423	1.542	2.285	4.768	7.832	8.845	8.980
0.4	1	0.140	0.429	1.108	2.012	2.501	2.598	2.617
	2	0.178	0.559	1.664	3.964	5.396	5.649	5.686
	3	0.216	0.681	2.037	4.480	6.688	7.229	7.313
	4	1.587	1.731	2.729	5.680	8.857	9.749	9.869
0.6	1	0.165	0.506	1.296	2.316	2.847	2.954	2.976
	2	0.210	0.660	1.957	4.587	6.194	6.469	6.509
	3	0.256	0.804	2.400	5.243	7.625	8.198	8.292
	4	1.815	1.989	3.182	6.582	10.085	11.034	11.163

(b)

k_f	Mode	Rotational restraint parameter $R_i^{\phi_x,\phi_y}$						
		0.1	1	10	100	1000	10000	$1.00E+10$
				$a/b = 2$				
0.2	1	3.444	3.858	4.588	4.806	4.833	4.835	4.836
	2	5.467	5.742	6.278	6.450	6.472	6.474	6.474
	3	8.161	8.349	8.750	8.890	8.908	8.909	8.910
	4	8.357	8.741	9.485	9.722	9.751	9.754	9.754
0.4	1	3.854	4.314	4.989	5.183	5.183	5.185	5.186
	2	6.061	6.362	6.855	7.009	7.009	7.011	7.011
	3	8.971	9.187	9.552	9.678	9.678	9.680	9.680
	4	8.987	9.437	10.142	10.37	10.347	10.349	10.349
0.6	1	4.421	4.946	5.682	5.866	5.887	5.889	5.889
	2	6.961	7.309	7.858	8.006	8.024	8.026	8.026
	3	10.160	10.584	10.999	11.124	11.139	11.140	11.141
	4	10.352	10.720	11.512	11.709	11.732	11.734	11.735

(b) Continued.

k_f	Mode	Rotational restraint parameter $R_i^{\phi_x,\phi_y}$						
		0.1	1	10	100	1000	10000	$1.00E+10$
		$a/b = 1.5$						
0.2	1	2.764	3.203	4.114	4.438	4.479	4.483	4.484
	2	5.686	6.122	7.270	7.771	7.839	7.846	7.847
	3	7.047	7.669	9.272	9.946	10.035	10.045	10.046
	4	9.588	10.107	11.673	12.471	12.586	12.598	12.599
0.4	1	3.188	3.703	4.631	4.925	4.961	4.965	4.966
	2	6.470	7.016	8.260	8.739	8.801	8.807	8.808
	3	7.847	8.632	10.324	10.927	11.003	11.011	11.012
	4	10.679	11.329	13.007	13.742	13.843	13.853	13.854
0.6	1	3.663	4.252	5.272	5.585	5.624	5.628	5.628
	2	7.394	8.040	9.448	9.973	10.040	10.047	10.048
	3	8.920	9.842	11.721	12.360	12.440	12.448	12.449
	4	12.113	12.873	14.748	15.537	15.643	15.654	15.655

Table 8: Frequency parameters $\overline{\omega}_i$ for $[0°/45°]$ carbon-epoxy AS4-3501-6 (Table 1), with different fiber volume fraction k_f and boundary conditions. $a/h = 10$.

Boundary conditions	k_f	Mode sequence number			
		1	2	3	4
$S_1S_1S_1S_1$	0.1	1.198	2.379	0.193	2.872
	0.2	1.435	2.683	0.166	3.337
	0.3	1.628	2.951	0.154	3.723
	0.4	1.804	3.212	0.148	4.092
	0.5	1.973	3.475	0.145	4.463
	0.6	2.143	3.754	0.145	4.859
	0.7	2.319	4.054	0.146	5.290
	0.8	2.489	4.344	0.148	5.724
$C_1C_1C_1C_1$	0.1	1.826	3.091	3.560	4.502
	0.2	2.073	3.407	4.032	4.961
	0.3	2.287	3.702	4.452	5.387
	0.4	2.498	4.003	4.874	5.824
	0.5	2.715	4.321	5.317	6.290
	0.6	2.949	4.671	5.807	6.809
	0.7	3.207	5.062	6.359	7.396
	0.8	3.466	5.449	6.934	7.982
$S_2S_2C_1C_1$	0.1	1.446	2.825	3.037	3.975
	0.2	1.651	3.137	3.469	4.621
	0.3	1.830	3.417	3.847	5.045
	0.4	2.002	3.697	4.213	5.470
	0.5	2.173	3.987	4.587	5.912
	0.6	2.351	4.303	4.989	6.395
	0.7	2.541	4.651	5.430	6.933
	0.8	2.724	4.989	5.876	7.464

includes the effective elastic moduli of each lamina obtained using the Mori-Tanaka mean field theory, which allows taking into account the influence of the fiber volume ratios and the elastic properties of the components (fiber and matrix) into the vibration behavior. The formulation is based on the first-order shear deformation theory, and the generalized displacements are approximate using sets of characteristic orthogonal polynomials generated by the Gram-Schmidt procedure. The consideration of all possible rotational and translational restraints allows generating any classical

boundary condition, only approaching the corresponding spring parameter to zero or infinity. The algorithm is computationally efficient, and the solutions are stables and convergent. Close agreement with existing results in the literature is shown and new results are presented in tables and figures which could be useful for design and optimization problems of general long fiber-reinforced laminated plates.

Appendix

The matrices K and M in (18) are given by

$$[\mathbf{K}] = \begin{bmatrix} \left[K_{ijkh}^{uu}\right] & \left[K_{ijkh}^{uv}\right] & \left[K_{ijkh}^{uw}\right] & \left[K_{ijkh}^{u\phi_x}\right] & \left[K_{ijkh}^{u\phi_y}\right] \\ & \left[K_{ijkh}^{vv}\right] & \left[K_{ijkh}^{vw}\right] & \left[K_{ijkh}^{v\phi_x}\right] & \left[K_{ijkh}^{v\phi_y}\right] \\ & & \left[K_{ijkh}^{ww}\right] & \left[K_{ijkh}^{w\phi_x}\right] & \left[K_{ijkh}^{w\phi_y}\right] \\ & & & \left[K_{ijkh}^{\phi_x\phi_x}\right] & \left[K_{ijkh}^{\phi_x\phi_y}\right] \\ \text{sym} & & & & \left[K_{ijkh}^{\phi_y\phi_y}\right] \end{bmatrix}, \tag{A.1}$$

where

$$\begin{aligned}
3K_{ijkh}^{uu} &= A_{11}\iint_R p_i^{'(u)} p_k^{'(u)} q_j^{(u)} q_h^{(u)}\,dx\,dy \\
&\quad + A_{16}\iint_R \left(p_i^{'(u)} p_k^{(u)} q_j^{(u)} q_h^{'(u)} \right. \\
&\qquad \left. + p_i^{(u)} p_k^{'(u)} q_j^{'(u)} q_h^{(u)}\right) dx\,dy \\
&\quad + A_{66}\iint_R p_i^{(u)} p_k^{(u)} q_j^{'(u)} q_h^{'(u)}\,dx\,dy \\
&\quad + t_2^u \int_0^b \left[p_i^{(u)} p_k^{(u)}\right]_{x=1} q_j^{(u)} q_h^{(u)}\,dy \\
&\quad + t_4^u \int_0^b \left[p_i^{(u)} p_k^{(u)}\right]_{x=0} q_j^{(u)} q_h^{(u)}\,dy, \\
K_{ijkh}^{uv} &= A_{12}\iint_R p_i^{'(u)} p_k^{(v)} q_j^{(u)} q_h^{'(v)}\,dx\,dy \\
&\quad + A_{16}\iint_R p_i^{'(v)} p_k^{'(u)} q_j^{(v)} q_h^{(u)}\,dx\,dy \\
&\quad + A_{26}\iint_R p_i^{(v)} p_k^{(u)} q_j^{'(v)} q_h^{'(u)}\,dx\,dy \\
&\quad + A_{66}\iint_R p_i^{'(v)} p_k^{(u)} q_j^{(v)} p_h^{'(u)}\,dx\,dy, \\
K_{ijkh}^{uw} &= 0, \qquad K_{ijkh}^{vw} = 0,
\end{aligned}$$

$$\begin{aligned}
K_{ijkh}^{u\phi_x} &= B_{11}\iint_R p_i^{'(u)} p_k^{'(\phi_x)} q_j^{(u)} q_h^{(\phi_x)}\,dx\,dy \\
&\quad + B_{16}\iint_R p_i^{'(u)} p_k^{(\phi_x)} q_j^{(u)} q_h^{'(\phi_x)}\,dx\,dy \\
&\quad + B_{16}\iint_R p_i^{(u)} p_k^{'(\phi_x)} q_j^{'(u)} q_h^{(\phi_x)}\,dx\,dy \\
&\quad + B_{66}\iint_R p_i^{(u)} p_k^{(\phi_x)} q_j^{'(u)} p_h^{'(\phi_x)}\,dx\,dy, \\
K_{ijkh}^{u\phi_y} &= B_{12}\iint_R p_i^{'(u)} p_k^{(\phi_y)} q_j^{(u)} q_h^{'(\phi_y)}\,dx\,dy \\
&\quad + B_{16}\iint_R p_i^{'(u)} p_k^{'(\phi_y)} q_j^{(u)} q_h^{(\phi_y)}\,dx\,dy \\
&\quad + B_{26}\iint_R p_i^{(u)} p_k^{(\phi_y)} q'^{(u)}_j q'^{(\phi_y)}_h\,dx\,dy \\
&\quad + B_{66}\iint_R p_i^{(u)} p_k^{'(\phi_y)} q'^{(u)}_j q_h^{(\phi_y)}\,dx\,dy, \\
K_{ijkh}^{vv} &= A_{22}\iint_R p_i^{(v)} p_k^{(v)} q_j^{'(v)} q_h^{'(v)}\,dx\,dy \\
&\quad + A_{26}\iint_R \left(p_i^{(v)} p_k^{'(v)} q_j^{'(v)} q_h^{(v)} \right. \\
&\qquad \left. + p_i^{'(v)} p_k^{(v)} q_j^{(v)} q_h^{'(v)}\right) dx\,dy \\
&\quad + A_{66}\iint_R p_i^{'(v)} p_k^{'(v)} q_j^{(v)} q_h^{(v)}\,dx\,dy \\
&\quad + t_1^v \int_0^a p_i^{(v)} p_k^{(v)} \left[q_j^{(v)} q_h^{(v)}\right]_{y=0} dx \\
&\quad + t_3^v \int_0^b p_i^{(v)} p_k^{(v)} \left[q_j^{(v)} q_h^{(v)}\right]_{y=1} dx, \\
K_{ijkh}^{v\phi_x} &= B_{12}\iint_R p_i^{(v)} p_k^{'(\phi_x)} q_j^{'(v)} q_h^{(\phi_x)}\,dx\,dy \\
&\quad + B_{16}\iint_R p_i^{'(v)} p_k^{'(\phi_x)} q_j^{(v)} q_h^{(\phi_x)}\,dx\,dy \\
&\quad + B_{26}\iint_R p_i^{(v)} p_k^{(\phi_x)} q_j^{'(v)} q_h^{'(\phi_x)}\,dx\,dy \\
&\quad + B_{66}\iint_R p_i^{'(v)} p_k^{(\phi_x)} q_j^{(v)} q_h^{'(\phi_x)}\,dx\,dy, \\
K_{ijkh}^{v\phi_y} &= B_{22}\iint_R p_i^{(v)} p_k^{(\phi_y)} q_j^{'(v)} q_h^{'(\phi_y)}\,dx\,dy \\
&\quad + B_{26}\iint_R p_i^{(v)} p_k^{'(\phi_y)} q_j^{'(v)} q_h^{(\phi_y)}\,dx\,dy \\
&\quad + B_{26}\iint_R p_i^{'(v)} p_k^{(\phi_y)} q_j^{(v)} q_h^{'(\phi_y)}\,dx\,dy \\
&\quad + B_{66}\iint_R p_i^{'(v)} p_k^{'(\phi_y)} q_j^{(v)} q_h^{(\phi_y)}\,dx\,dy,
\end{aligned}$$

$$
\begin{aligned}
K_{ijkh}^{ww} &= A_{44}\iint_R p_i^{(w)} p_k^{(w)} q_j^{'(w)} q_h^{'(w)}\,dx\,dy \\
&\quad + A_{55}\iint_R p_i^{'(w)} p_k^{'(w)} q_j^{(w)} q_h^{(w)}\,dx\,dy \\
&\quad + A_{45}\iint_R \Big(p_i^{'(w)} p_k^{(w)} q_j^{(w)} q_h^{'(w)} \\
&\qquad + p_i^{(w)} p_k^{'(w)} q_j^{'(w)} q_h^{(w)}\Big)\,dx\,dy \\
&\quad + t_1^w \int_0^a p_i^{(w)} p_k^{(w)} \left[q_j^{(w)} q_h^{(w)}\right]_{y=0} dx \\
&\quad + t_2^w \int_0^b \left[p_i^{(w)} p_k^{(w)}\right]_{x=1} q_j^{(w)} q_h^{(w)}\,dy \\
&\quad + t_3^w \int_0^a p_i^{(w)} p_k^{(w)} \left[q_j^{(w)} q_h^{(w)}\right]_{y=1} dx \\
&\quad + t_4^w \int_0^b \left[p_i^{(w)} p_k^{(w)}\right]_{x=0} q_j^{(w)} q_h^{(w)}\,dy, \\
K_{ijkh}^{w\phi_x} &= K\Big(A_{45}\iint_R p_i^{(w)} p_k^{(\phi_x)} q_j^{'(w)} q_h^{(\phi_x)}\,dx\,dy \\
&\quad + A_{55}\iint_R p_i^{'(w)} p_k^{(\phi_x)} q_j^{(w)} q_h^{(\phi_x)}\,dx\,dy\Big), \\
K_{ijkh}^{w\phi_y} &= K\Big(A_{44}\iint_R p_i^{(w)} p_k^{(\phi_y)} q_j^{'(w)} q_h^{(\phi_y)}\,dx dy \\
&\quad + A_{45}\iint_R p_i^{'(w)} p_k^{(\phi_y)} q_j^{(w)} q_h^{(\phi_y)}\,dx\,dy\Big), \\
K_{ijkh}^{\phi_x\phi_x} &= KA_{55}\iint_R p_i^{(\phi_x)} p_k^{(\phi_x)} q_j^{(\phi_x)} q_h^{(\phi_x)}\,dx\,dy \\
&\quad + D_{11}\iint_R p_i^{'(\phi_x)} p_k^{'(\phi_x)} q_j^{(\phi_x)} q_h^{(\phi_x)}\,dx\,dy \\
&\quad + D_{16}\iint_R \Big(p_i^{'(\phi_x)} p_k^{(\phi_x)} q_j^{(\phi_x)} q_h^{'(\phi_x)} \\
&\qquad + p_i^{(\phi_x)} p_k^{'(\phi_x)} q_j^{'(\phi_x)} q_h^{(\phi_x)}\Big)\,dx\,dy \\
&\quad + D_{66}\iint_R p_i^{(\phi_x)} p_k^{(\phi_x)} q_j^{'(\phi_x)} q_h^{(\phi_x)}\,dx\,dy \\
&\quad + r_2 \int_0^b \left[p_i^{(\phi_x)} p_k^{(\phi_x)}\right]_{x=a} q_j^{(\phi_x)} q_h^{(\phi_x)}\,dy \\
&\quad + r_4 \int_0^b \left[p_i^{(\phi_x)} p_k^{(\phi_x)}\right]_{x=0} q_j^{(\phi_x)} q_h^{(\phi_x)}\,dy, \\
K_{ijkh}^{\phi_x\phi_y} &= KA_{45}\iint_R p_i^{(\phi_x)} p_k^{(\phi_y)} q_j^{(\phi_x)} q_h^{(\phi_y)}\,dx\,dy \\
&\quad + D_{12}\iint_R p_i^{'(\phi_x)} p_k^{(\phi_y)} q_j^{(\phi_x)} q_h^{'(\phi_y)}\,dx\,dy \\
&\quad + D_{16}\iint_R p_i^{'(\phi_x)} p_k^{'(\phi_y)} q_j^{(\phi_x)} q_h^{(\phi_y)}\,dx\,dy \\
&\quad + D_{26}\iint_R p_i^{(\phi_x)} p_k^{(\phi_y)} q_j^{'(\phi_x)} q_h^{'(\phi_y)}\,dx\,dy \\
&\quad + D_{66}\iint_R p_i^{(\phi_x)} p_k^{'(\phi_y)} q_j^{'(\phi_x)} q_h^{(\phi_y)}\,dx\,dy, \\
K_{ijkh}^{\phi_y\phi_y} &= KA_{44}\iint_R p_i^{(\phi_y)} p_k^{(\phi_y)} q_j^{(\phi_y)} q_h^{(\phi_y)}\,dx\,dy \\
&\quad + D_{22}\iint_R p_i^{(\phi_y)} p_k^{(\phi_y)} q_j^{'(\phi_y)} q_h^{'(\phi_y)}\,dx\,dy \\
&\quad + D_{26}\iint_R \Big(p_i^{(\phi_y)} p_k^{'(\phi_y)} q_j^{'(\phi_y)} q_h^{(\phi_y)} \\
&\qquad + p_i^{'(\phi_y)} p_k^{(\phi_y)} q_j^{(\phi_y)} q_h^{'(\phi_y)}\Big)\,dx\,dy \\
&\quad + D_{66}\iint_R p_i^{'(\phi_y)} p_k^{'(\phi_y)} q_j^{(\phi_y)} q_h^{(\phi_y)}\,dx\,dy \\
&\quad + r_1 \int_0^a p_i^{(\phi_y)} p_k^{(\phi_y)} \left[q_j^{(\phi_y)} q_h^{(\phi_y)}\right]_{y=0} dx \\
&\quad + r_3 \int_0^a p_i^{(\phi_y)} p_k^{(\phi_y)} \left[q_j^{(\phi_y)} q_h^{(\phi_y)}\right]_{y=b} dx.
\end{aligned}
\tag{A.2}
$$

with $K = 5/6$

$$
[\mathbf{M}] = \begin{bmatrix}
\left[M_{ijkh}^{uu}\right] & 0 & 0 & 0 & 0 \\
 & \left[M_{ijkh}^{vv}\right] & 0 & 0 & 0 \\
 & & \left[M_{ijkh}^{ww}\right] & 0 & 0 \\
 & & & \left[M_{ijkh}^{\phi_x\phi_x}\right] & 0 \\
\text{sym} & & & & \left[M_{ijkh}^{\phi_y\phi_y}\right]
\end{bmatrix},
$$

$$
\begin{aligned}
M_{ijkh}^{uu} &= I_0\iint_R p_i^{(u)} p_k^{(u)} q_j^{(u)} q_h^{(u)}\,dx\,dy, \\
M_{ijkh}^{vv} &= I_0\iint_R p_i^{(v)} p_k^{(v)} q_j^{(v)} q_h^{(v)}\,dx\,dy, \\
M_{ijkh}^{ww} &= I_0\iint_R p_i^{(w)} p_k^{(w)} q_j^{(w)} q_h^{(w)}\,dx\,dy, \\
M_{ijkh}^{\phi_x\phi_x} &= I_2\iint_R p_i^{(\phi_x)} p_k^{(\phi_x)} q_j^{(\phi_x)} q_h^{(\phi_x)}\,dx\,dy, \\
M_{ijkh}^{\phi_y\phi_y} &= I_2\iint_R p_i^{(\phi_y)} p_k^{(\phi_y)} q_j^{(\phi_y)} q_h^{(\phi_y)}\,dx\,dy.
\end{aligned}
\tag{A.3}
$$

Acknowledgment

The authors wish to thank the economic support of CONICET (PIP no. 0105/2010) and CIUNSa.

References

[1] E. Reissner, "On transverse bending of plates, including the effect of transverse shear deformation," *International Journal of Solids and Structures*, vol. 11, no. 5, pp. 569–576, 1975.

[2] R. D. Mindlin, "Influences of rotatory inertia and shear inflexural motion of isotropic, elastic plates," *Journal of Applied Mechanics*, vol. 18, pp. 1031–1036, 1951.

[3] H. R. H. Kabir, "On the frequency response of moderately thick simply supported rectangular plates with arbitrary lamination," *International Journal of Solids and Structures*, vol. 36, no. 15, pp. 2285–2301, 1999.

[4] K. M. Liew, "Solving the vibation of thick symmetric laminates by Reissner/Mindlin plate theory and the p-Ritz method," *Journal of Sound and Vibration*, vol. 198, no. 3, pp. 343–360, 1996.

[5] J. W. Shi, A. Nakatani, and H. Kitagawa, "Vibration analysis of fully clamped arbitrarily laminated plate," *Composite Structures*, vol. 63, no. 1, pp. 115–122, 2004.

[6] M. Aydogdu and T. Timarci, "Vibration analysis of cross-ply laminated square plates with general boundary conditions," *Composites Science and Technology*, vol. 63, no. 7, pp. 1061–1070, 2003.

[7] L. Liu, L. P. Chua, and D. N. Ghista, "Mesh-free radial basis function method for static, free vibration and buckling analysis of shear deformable composite laminates," *Composite Structures*, vol. 78, no. 1, pp. 58–69, 2007.

[8] G. R. Liu, X. Zhao, K. Y. Dai, Z. H. Zhong, G. Y. Li, and X. Han, "Static and free vibration analysis of laminated composite plates using the conforming radial point interpolation method," *Composites Science and Technology*, vol. 68, no. 2, pp. 354–366, 2008.

[9] J. Wang, K. M. Liew, M. J. Tan, and S. Rajendran, "Analysis of rectangular laminated composite plates via FSDT meshless method," *International Journal of Mechanical Sciences*, vol. 44, no. 7, pp. 1275–1293, 2002.

[10] K. S. Numayr, R. H. Haddad, and M. A. Haddad, "Free vibration of composite plates using the finite difference method," *Thin-Walled Structures*, vol. 42, no. 3, pp. 399–414, 2004.

[11] W. Lanhe, L. Hua, and W. Daobin, "Vibration analysis of generally laminated composite plates by the moving least squares differential quadrature method," *Composite Structures*, vol. 68, no. 3, pp. 319–330, 2005.

[12] P. Ribeiro, "First-order shear deformation, p-version, finite element for laminated plate nonlinear vibrations," *AIAA Journal*, vol. 43, no. 6, pp. 1371–1379, 2005.

[13] A. J. M. Ferreira and G. E. Fasshauer, "Analysis of natural frequencies of composite plates by an RBF-pseudospectral method," *Composite Structures*, vol. 79, no. 2, pp. 202–210, 2007.

[14] P. Malekzadeh and S. A. Shahpari, "Free vibration analysis of variable thickness thin and moderately thick plates with elastically restrained edges by DQM," *Thin-Walled Structures*, vol. 43, no. 7, pp. 1037–1050, 2005.

[15] F. Ohya, M. Ueda, T. Uchiyama, and M. Kikuchi, "Free vibration analysis by the superposition method of rectangular Mindlin plates with internal columns resting on uniform elastic edge supports," *Journal of Sound and Vibration*, vol. 289, no. 1-2, pp. 1–24, 2006.

[16] D. Zhou, "Vibrations of Mindlin rectangular plates with elastically restrained edges using static Timoshenko beam functions with the Rayleigh-Ritz method," *International Journal of Solids and Structures*, vol. 38, no. 32-33, pp. 5565–5580, 2001.

[17] K. Khorshidi, "Vibro-acoustic analysis of Mindlin rectangular plates resting on an elastic foundation," *Scientia Iranica*, vol. 18, no. 1, pp. 60–69, 2001.

[18] L. H. Wu and Y. Lu, "Free vibration analysis of rectangular plates with internal columns and uniform elastic edge supports by pb-2 Ritz method," *International Journal of Mechanical Sciences*, vol. 53, no. 7, pp. 494–504, 2011.

[19] G. Y. Jin, H. Chen, J. T. Du, T. J. Yang, and W. Y. Li, "The Influence of edge restraining stiffness on the transverse vibrations of rectangular plate structures," *Journal of Marine Science and Application*, vol. 9, no. 4, pp. 393–402, 2010.

[20] A. R. Setoodeh and G. Karami, "A solution for the vibration and buckling of composite laminates with elastically restrained edges," *Composite Structures*, vol. 60, no. 3, pp. 245–253, 2003.

[21] G. Karami, P. Malekzadeh, and S. R. Mohebpour, "DQM free vibration analysis of moderately thick symmetric laminated plates with elastically restrained edges," *Composite Structures*, vol. 74, no. 1, pp. 115–125, 2006.

[22] A. S. Ashour, "Vibration of angle-ply symmetric laminated composite plates with edges elastically restrained," *Composite Structures*, vol. 74, no. 3, pp. 294–302, 2006.

[23] L. G. Nallim and R. O. Grossi, "Vibration of angle-ply symmetric laminated composite plates with edges elastically restrained," *Composite Structures*, vol. 81, no. 1, pp. 80–83, 2007.

[24] S. Chakraverty and M. Petyt, "Natural frequencies for free vibration of nonhomogeneous elliptic and circular plates using two-dimensional orthogonal polynomials," *Applied Mathematical Modelling*, vol. 21, no. 7, pp. 399–417, 1997.

[25] B. Singh and S. Chakraverty, "Flexural vibration of skew plates using boundary characteristic orthogonal polynomials in two variables," *Journal of Sound and Vibration*, vol. 173, no. 2, pp. 157–178, 1994.

[26] S. Chakraverty, R. B. Bhat, and I. Stiharu, "Free vibration of annular elliptic plates using boundary characteristic orthogonal polynomials as shape functions in the Rayleigh-Ritz method," *Journal of Sound and Vibration*, vol. 241, no. 3, pp. 524–539, 2001.

[27] S. T. Chow, K. M. Liew, and K. Y. Lam, "Transverse vibration of symmetrically laminated rectangular composite plates," *Composite Structures*, vol. 20, no. 4, pp. 213–226, 1992.

[28] H. Altenbach, J. Altenbach, and W. Kisssing, *Mechanics of Composite Structural Elements*, Springer, Berlin, Germany, 2004.

[29] T. Mori and K. Tanaka, "Average stress in matrix and average elastic energy of materials with misfitting inclusions," *Acta Metallurgica*, vol. 21, no. 5, pp. 571–574, 1973.

[30] P. D. Soden, M. J. Hinton, and A. S. Kaddour, "Lamina properties, lay-up configurations and loading conditions for a range of fibre-reinforced composite laminates," *Composites Science and Technology*, vol. 58, no. 7, pp. 1011–1022, 1998.

[31] A. Alibeigloo, M. Shakeri, and M. R. Kari, "Free vibration analysis of antisymmetric laminated rectangular plates with distributed patch mass using third-order shear deformation theory," *Ocean Engineering*, vol. 35, no. 2, pp. 183–190, 2008.

[32] J. N. Reddy, "A simple higher-order theory for laminated composite plates," *ASME Journal of Applied Mechanics*, vol. 51, no. 4, pp. 745–752, 1984.

[33] J. D. Eshelby, "The determination of the elastic field of an ellipsoidal inclusion and related problems," *Proceedings of the Royal Society*, vol. 241, pp. 376–396, 1957.

[34] G. P. Tandon and G. J. Weng, "The effect of aspect ratio of inclusions on the elastic properties of unidirectionally aligned composites," *Polymer Composites*, vol. 5, no. 4, pp. 327–333, 1984.

[35] J. N. Reddy, *Mechanics of Laminated Composite Plates and Shells: Theory and Analysis*, CRC Press, Boca Raton, Fla, USA, 2nd edition, 2003.

[36] J. M. Whitney, *Structural Analysis of Laminated Anisotropic Plates*, Technomic Publishing Co., Lancaster, Pa, USA, 1987.

[37] L. G. Nallim and R. O. Grossi, "On the use of orthogonal polynomials in the study of anisotropic plates," *Journal of Sound and Vibration*, vol. 264, no. 5, pp. 1201–1207, 2003.

[38] L. G. Nallim and S. Oller, "An analytical-numerical approach to simulate the dynamic behaviour of arbitrarily laminated

composite plates," *Composite Structures*, vol. 85, no. 4, pp. 311–325, 2008.

[39] R. B. Bhat, "Plate deflection using orthogonal polynomials," *Journal of Engineering Mechanics*, vol. 101, no. 11, pp. 1301–1309, 1985.

[40] N. M. Auciello and A. Ercolano, "A general solution for dynamic response of axially loaded non-uniform Timoshenko beams," *International Journal of Solids and Structures*, vol. 41, no. 18-19, pp. 4861–4874, 2004.

Hindawi Publishing Corporation
Advances in Acoustics and Vibration
Volume 2011, Article ID 659797, 6 pages
doi:10.1155/2011/659797

Research Article

Influence of Multiharmonics Excitation on Rattle Noise in Automotive Gearboxes

Y. Kadmiri,[1,2] J. Perret-Liaudet,[1] E. Rigaud,[1] A. Le Bot,[1] and L. Vary[2]

[1] *Laboratoire de Tribologie et Dynamique des Systèmes, UMR CNRS 5513, Ecole Centrale de Lyon, Université de Lyon, 69130 Ecully, France*
[2] *Renault S.A.S., Centre Technique, 91510 Lardy, France*

Correspondence should be addressed to Y. Kadmiri, younes.kadmiri@ec-lyon.fr

Received 12 January 2011; Accepted 2 June 2011

Academic Editor: Kok Keong Choong

We consider the automotive gearbox rattle noise resulting from vibro-impacts that can occur between the idle gears under excessive velocity fluctuations of the shaft-driving gears imposed by engine torque fluctuation. Even if the rattling phenomenon has no consequence on reliability, it may be particularly annoying for vehicle interior sound quality and acoustic comfort. The main parameters governing such kind of vibrations are the excitation source associated with engine torque fluctuation which can be modeled by an imposed displacement of the driveline, the inertia of the idle gear, the drag torque acting during the free flight motion, and the impact laws. In the case of rattle, it is reasonable to assume that duration of impacts between teeth is very short compared to the excitation period. Then, these impacts are modeled by a coefficient of restitution law. The excitation source is not composed only with fundamental component but also with other harmonic components. This study presents some effects of these additional components on the dynamic response of the idle gear.

1. Introduction

Acoustic comfort is an important sales point, in particular in car industry [1]. For many years, the research efforts allowed reduction of acoustic levels, in particular those related to interior sources like the engine-related noise and to exterior sources as tire and wind-related noises [2]. Consequently, noise sources that were previously masked emerge, because of the total reduction of the acoustic level. Among those, rattle noise in automotive gearboxes needs to be reduced. Actually, it is perceived like an unpleasant noise, more for its intrusive character, than for the acoustic levels generated.

Rattle noise results from the dynamic behavior of idle gears induced by the fluctuations of the driveline velocity. Under certain operating conditions, the idle gears can vibrate through their functional backlashes. Consequently, rattle noise is mainly related to impacts between gear teeth. The only harmful effect is radiated noise since impacts between gears do not change the dynamic behavior of the drivelines and do not lead to excessive loads and damage.

The key parameters governing rattle noise are the inertia of the idle gears, the drag torque acting on the idle gears, the elastic, and damping characteristics during impacts and free flights and the velocity fluctuations of the driving gears. These last ones result from velocity fluctuation of the engine which mainly depends on the engine type, driveline design, and car running conditions [3]. Frequency content is dominated by harmonics of the engine rotational velocity.

There are several studies concerning rattle noise [3–9]. Among these, some deal with the analysis of the complete dynamic behavior of the entire driveline in relation with design [4–6], whereas others remain localized on the idle gears dynamics [7, 8]. Two ways are retained for introducing the impact force [10]: it is modeled by stereo-mechanical impact with the introduction of a coefficient of restitution [7, 8, 11–13], or by elastic and damping characteristics during impacts [5]. Other authors concentrate their analysis on drag torque [14]. In all these studies, the excitation source is

generally introduced as a purely harmonic excitation related to the engine torque fluctuations. Few experimental studies recently considered multiharmonic excitations [13, 15, 16].

In this context, the main objective of this paper is to present some theoretical results in relation with the effects of multiharmonics excitation related to the acyclic fluctuations induced by engine torque.

2. Assumptions

Several assumptions for modeling the motion of the idle gear can be done as follows. Impacts duration is supposed infinitely short so that impacts are described by a coefficient of restitution. Drag torque is assumed to be constant during the gear-free flight. This assumption remains valuable as long as velocity fluctuation of the driving gear remains negligible compared with the average velocity. In addition, interactions between the dynamic response of the idle driven gear and the motion of the driving gear are neglected. The motion of the driving gear is assumed to be a periodic function and corresponds to the excitation source. Finally, backlash between teeth is assumed to be constant. Based on these assumptions, a single-degree-of-freedom nonlinear model is built to describe the idle gear dynamics.

3. Dynamic Modeling

3.1. Equation of Motion. The nonlinear single-degree-of-freedom model of rattle gear is displayed in Figure 1. $x(t)$ is the equivalent displacement along the line of action corresponding to angular fluctuations of the idle gear around its theoretical position, m is an equivalent mass associated with its inertia, F is the constant force associated with the drag torque, $y(t)$ is the periodic displacement function taking into account the engine velocity fluctuation, and j is the constant backlash between teeth. Equation of motion during the idle gear free flight can be written in the following form:

$$m\ddot{x} = -F, \qquad y(t) < x(t) < y(t) + j. \tag{1}$$

A simple and usual law describing stereo-mechanical impact is introduced:

$$\dot{x}_{t+\delta t} - \dot{y}_{t+\delta t} = -r(\dot{x}_t - \dot{y}_t), \tag{2}$$

with

$$\delta t \longrightarrow 0, \tag{3}$$

where superdot denotes derivative respect to time and r is the coefficient of restitution taking into account dissipation during impact.

In addition, a limit impact velocity is defined for which there are no rebounds anymore. Therefore, conditions leading to a permanent contact between driven and driving gears need to be expressed. Beyond this limit velocity, contact between gears is preserved as long as the reaction force acting on the free driven gear $R(t)$ remains positive. Thus, for the active flank, the following condition must be verified:

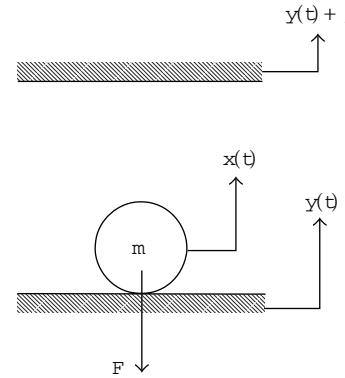

Figure 1: Rattle gear modeling.

$$0 < R(t) = F + m\ddot{y}(t), \tag{4}$$

and for the reverse flank,

$$0 > R(t) = F + m\ddot{y}(t). \tag{5}$$

Finally, the displacement excitation is described in the following subchapter.

3.2. Displacement Excitation. In the case of heat reciprocating engine, torque fluctuations are periodic and characterized by high levels. As example, for a four-stroke internal combustion engine with four cylinders, the fundamental period is twice the period of the rotation of the engine output shaft. Induced dynamic responses of every fixed gear driving the idle gears correspond to periodic functions with a rich spectral content. Then, $y(t)$ can be written as follows:

$$y(t) = \sum_{k=1}^{\infty} H_k \cos(k\omega t - \varphi_k), \tag{6}$$

where ω is the fundamental circular frequency, and H_k and φ_k are, respectively, amplitude and phase of the harmonic components of order k. A stationary regime is considered. Amplitude and phase are assumed to be independent of the rotational speed of the engine and the dynamic response of the entire driveline.

3.3. Impulse. Dimensionless impulse associated with impacts is introduced in order to characterize excitation forces transmitted to the gearbox.

As the impacts duration is assumed to be very short, the impulse can be expressed as follows:

$$I = \lim_{\delta t \to 0} \{m(\dot{x}(t + \delta t) - \dot{x}(t))\}. \tag{7}$$

3.4. Dimensionless Equations. Introducing dimensionless variables,

$$\tilde{x} = \frac{x}{H}, \qquad \tilde{y} = \frac{y}{H},$$
$$\tilde{j} = \frac{j}{H}, \qquad \tilde{t} = \omega t, \tag{8}$$
$$\tilde{R} = \frac{R}{F}.$$

The dimensionless number Λ depends on the equivalent mass m, the constant force associated with the drag torque F, the amplitude of the excitation H, and the fundamental circular frequency ω:

$$\Lambda = \frac{mH\omega^2}{F}. \tag{9}$$

Equations (1), (2), (4), and (5) can be returned as follows:

$$\Lambda\ddot{\tilde{x}} = -1, \qquad \tilde{y} < \tilde{x} < \tilde{y} + \tilde{j},$$
$$\dot{\tilde{x}}_{t+\delta t} - \dot{\tilde{y}}_{t+\delta t} = -r\left(\dot{\tilde{x}}_t - \dot{\tilde{y}}_t\right), \tag{10}$$
$$\tilde{R} = 1 + \Lambda\ddot{\tilde{y}}.$$

And the dimensionless impulse can be written as follows:

$$\tilde{I} = \frac{I}{m\omega H_1}. \tag{11}$$

4. Dynamics Induced by a Purely Harmonic Excitation

Figure 2 displays dimensionless impulse versus parameter Λ for an harmonic excitation. Five parts are observed and, so, five different dynamic responses of the idle gear. The part A corresponds to a permanent contact motion. The part B corresponds to periodic responses with impacts on the active flank followed by a permanent contact. The part C corresponds to a periodic response with one impact on the active flank per period. The part D corresponds to chaotic motion. Finally, the part E corresponds to the periodic response with two impacts per period, one on the active flank (positive impulses) and the other on the reverse one (negative impulses). The idle gear crosses the entire backlash. This kind of response exists for a large range of Λ.

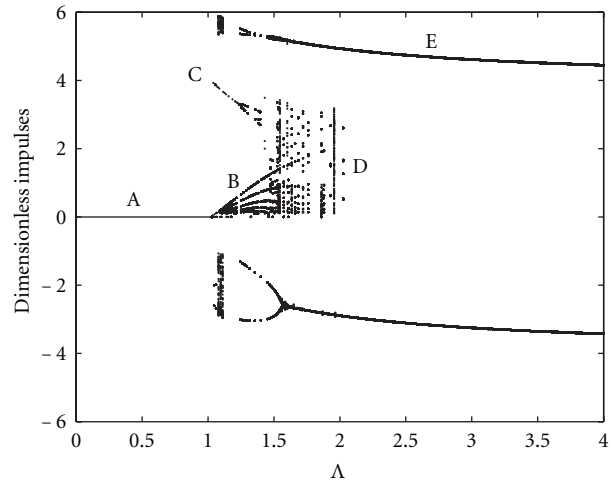

Figure 2: Impulses versus Λ for an excitation purely harmonic, $r = 0.65$ and $j = 8$.

Dynamic response histories are displayed on Figure 3. They correspond to the different parts described on the dimensionless impulse map (except permanent contact motion).

5. Effects of a Multiharmonics Excitation

In this section, the second harmonic component is introduced, in order to impose an excitation more representative of the velocity fluctuation. The ratio of second harmonic H_2 to first harmonic amplitude H_1 is 0.25 and its phase φ_2 is equal to 45°. Compared to purely harmonic case shown in Figure 2, dynamic behavior is very different (see Figure 4). The parts C and E have disappeared. Beyond solutions corresponding to successions of permanent contact and impacts, chaotic responses solutions characterized by impacts on the active and reverse flanks are observed.

The phase of the second harmonic plays also a significant role. Figure 5 displays the dimensionless impulses versus Λ for φ_2 equal to 90°. Periodic responses are observed. The large range of chaotic responses disappears. The effect of the phase on the dynamic response is highlighted on Figure 6 which displays the evolution of the dimensionless intensity versus phase for fixed parameter Λ.

Figure 7 displays the Poincaré map for Λ equal to 3.3 (ratio of H_2 to H_1 is 0.25, φ_2 is 45°). The strange attractor indicates that the idle gear response is chaotic. Time response history and corresponding Poincaré map are displayed on Figure 8 for the dynamic response corresponding to Λ equal to 3.3 (ratio of H_2 to H_1 is 0.25, φ_2 is 90°). The dynamic response of the idle gear is periodic with two impacts per period, one impact on the active flank and the other on the reverse flank, as observed for a purely harmonic excitation with the same value Λ (Figure 3).

Finally, frequency contents and phases of the excitation source play a significant role on the dynamic of the idle gear. Various kinds of responses are observed, from periodic ones with impacts on the active and reverse flanks to chaos.

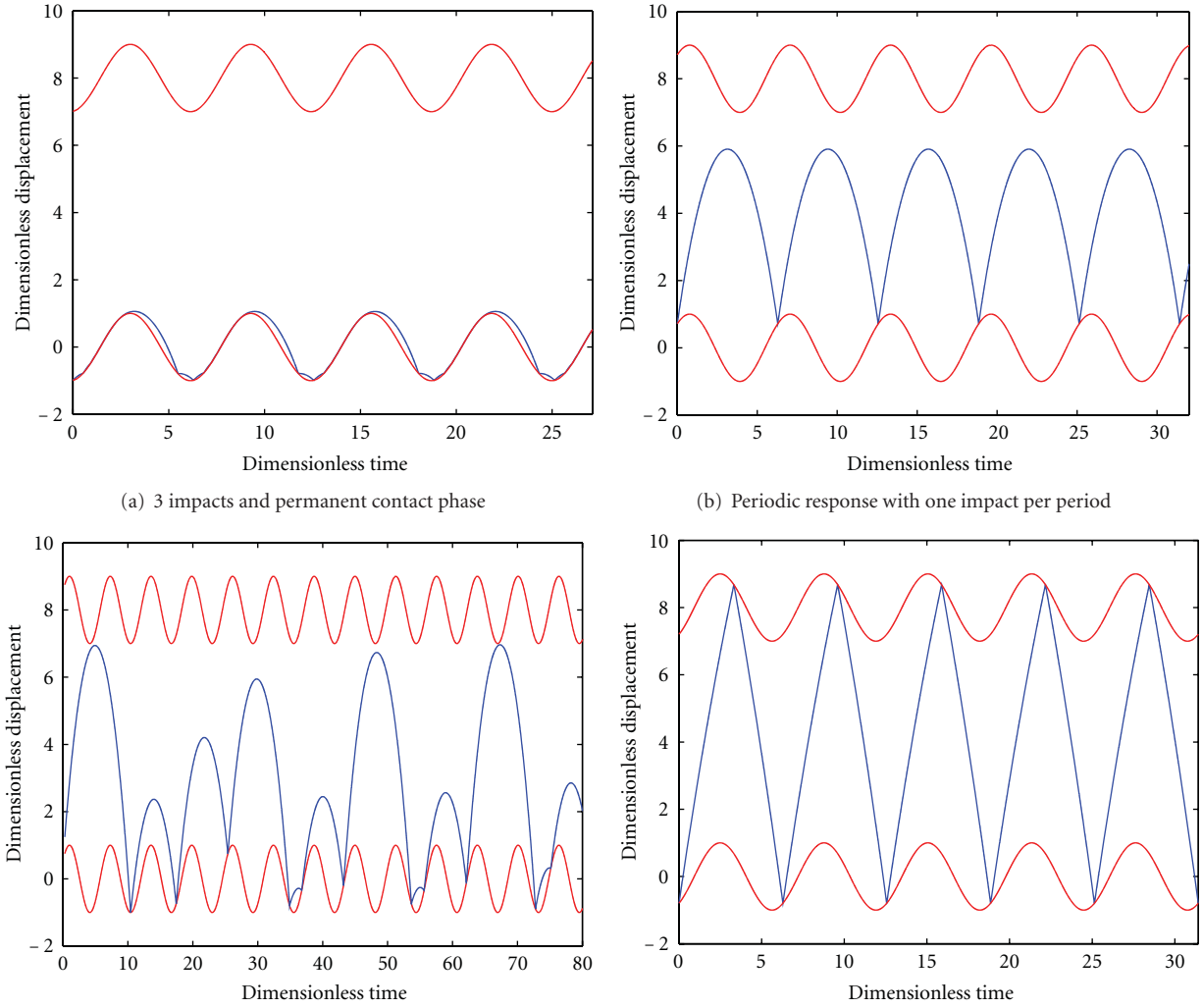

(a) 3 impacts and permanent contact phase

(b) Periodic response with one impact per period

(c) Chaotic response

(d) Periodic response with two impacts per period

FIGURE 3: Time response histories of the idle gear for $r = 0.65$ and $j = 8$. Upper and lower sinusoidal curves correspond to the motion of the driving gear teeth separated by constant clearance.

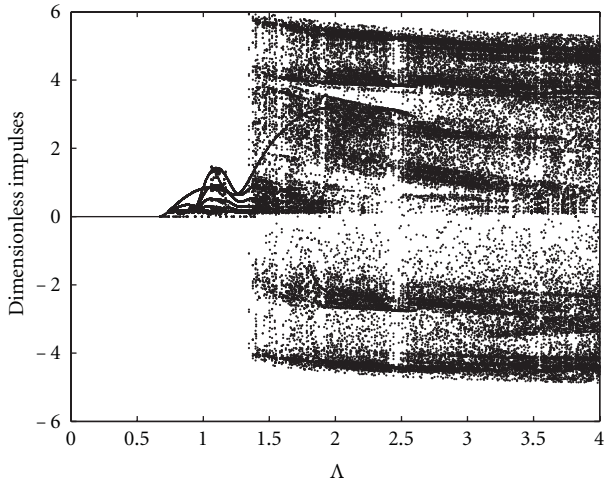

FIGURE 4: Impulses versus Λ for a multiharmonics excitation $\varphi_2 = 45°$, $r = 0.65$, and $j = 8$.

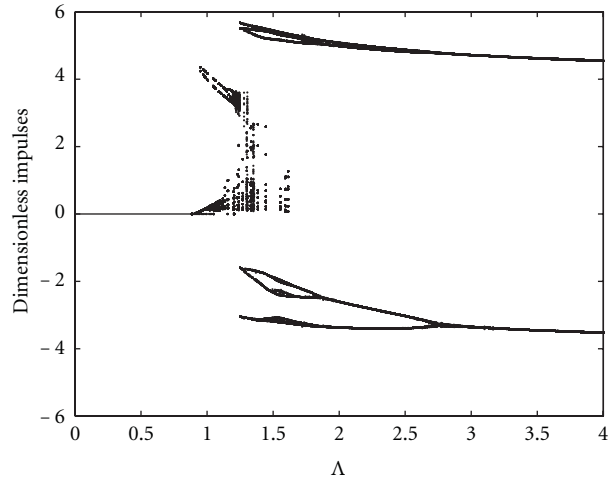

FIGURE 5: Impulses versus Λ for a multiharmonics excitation $\varphi_2 = 90°$, $r = 0.65$, and $j = 8$.

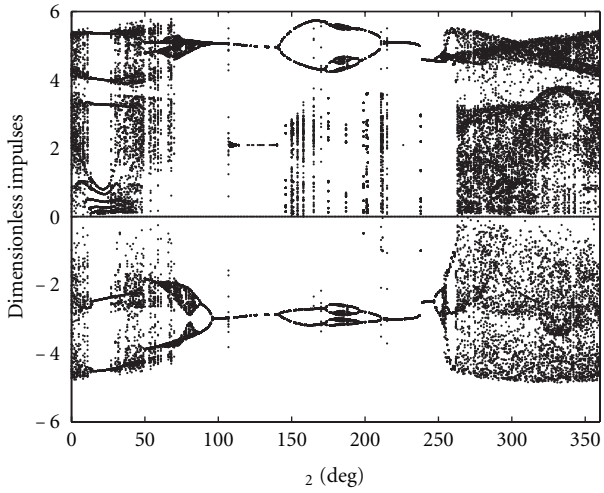

Figure 6: Impulses versus φ_2 for $\Lambda = 1.95$, $r = 0.65$, and $j = 8$.

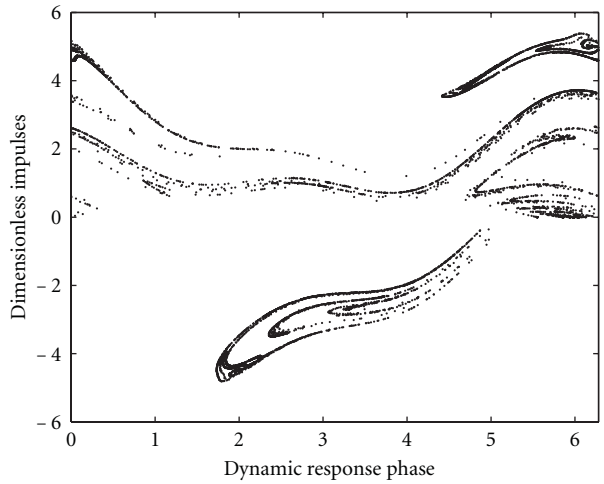

Figure 7: Poincaré map for a multiharmonics excitation $\varphi_2 = 45°$ for $\Lambda = 3.3$, $r = 0.65$, and $j = 8$.

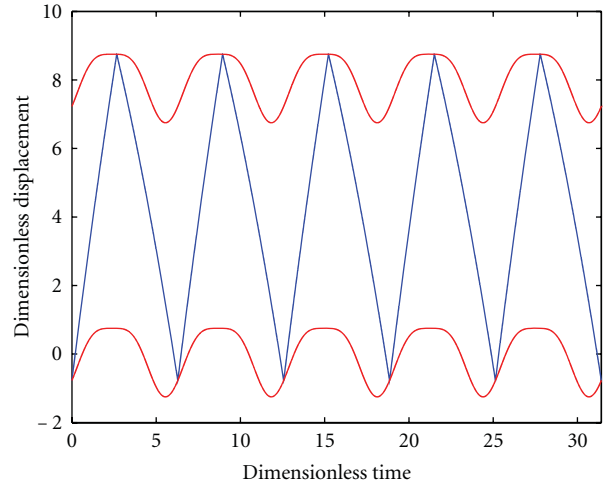

(a)

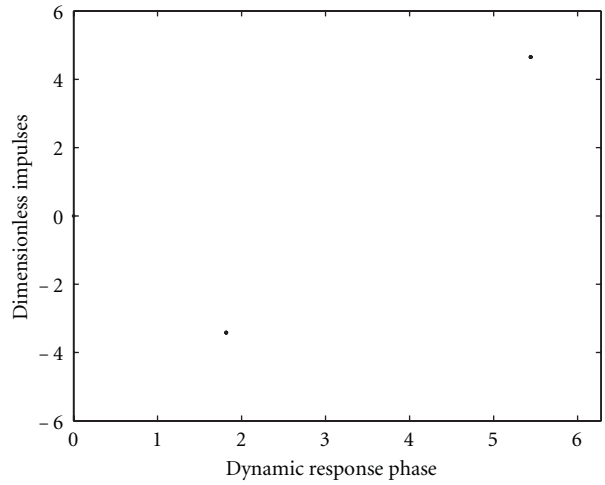

(b)

Figure 8: Time response history (a) and Poincaré map (b) for a multiharmonics excitation $\varphi_2 = 90°$ for $\Lambda = 3.3$, $r = 0.65$, and $j = 8$.

6. Conclusion

Noise and vibration due to gear rattle are an irritating problem. In this paper, a nonlinear single-degree-of-freedom system modeling the idle gear dynamics has been built. Some effects of a multiharmonics excitation are analyzed. Dynamic responses are compared to the ones obtained in the case of a purely harmonic excitation. Results show that, for usual amplitudes of the second harmonic of excitation, significant modifications of responses are observed, including emergence or extinction of chaotic motions. Further, we show that phases play an important role on the dynamic of the idle gear. We can conclude that controlling the rattle noise requires the precise knowledge of the excitation source corresponding to the driving fixed gear response spectral content. Finally, the variety of responses (periodic, chaotic responses, impact occurrences on reverse and active flanks, etc.) play an important effect on the resulting noise emitted from the gearbox, and more particularly on its sound quality.

Acknowledgments

The authors acknowledge Renault S.A.S. for the support of a research grant and the French Research Agency for its financial support (project ANR-06-BLAN-0115).

References

[1] M. A. Trapp and K. K. Hodgdon, "An evaluation of friction and impact induced acoustic behaviour of selected automotive materials, part II: impact induced acoustics," *International Journal of Vehicle Noise and Vibration*, vol. 4, no. 1, pp. 17–34, 2008.

[2] M. S. Qatu, M. K. Abdelhamid, J. Pang, and G. Sheng, "Overview of automotive noise and vibration," *International Journal of Vehicle Noise and Vibration*, vol. 5, no. 1-2, pp. 1–35, 2009.

[3] A. Rust, F. K. Brandl, and G. E. Thien, "Investigations into gear rattle phenomena—key parameters and their influence

on gearbox noise," *Institution of Mechanical Engineers*, pp. 113–120, C404/001, 1990.

[4] T. Sakai, Y. Doi, K. Yamamoto, T. Ogasawara, and M. Narita, "Theoretical and experimental analysis of rattling noise of automotive gearbox," Tech. Rep. 810773, pp. 85–91, Society of Automotive Engineers, 1981.

[5] R. Singh, H. Xie, and R.-J. Comparin, "Analysis of automotive neutral grear rattle," *Journal of Sound and Vibration*, vol. 131, no. 2, pp. 177–196, 1989.

[6] C. Padmanabhan and R. Singh, "Influence of clutch design on the reduction and perception of automotive transmission rattle noise," in *Proceedings of the National Conference on Noise Control Engineering: Noise Control in Aeroacoustics*, Williamsburg, Va, USA, 1993.

[7] F. Pfeiffer, "Modelling problems of rattling in gear-boxes," in *Proceedings of the MPT'91, Japan Society of Mechanical Engineers International Conference on Motion and Power Transmission*, pp. 43–48, Hiroshima, Japan, November 1991.

[8] G. Weidmer and G. Lechner, "Rattling vibrations in automotive transmissions," in *Proceedings of the MPT'91, Japan Society of Mechanical Engineers International Conference on Motion and Power Transmission*, pp. 37–42, Hiroshima, Japan, November 1991.

[9] J. Wang, M. Qatu, and R. Dukkipati, "A metric for automotive transaxle rattle," *International Journal of Vehicle Noise and Vibration*, vol. 5, no. 4, pp. 300–307, 2009.

[10] J. Perret-Liaudet and E. Rigaud, "Some effects of gear eccentricities on automotive rattle noise," in *Proceedings of the 10th ASME International Power Transmission and Gearing Conference*, no. 34794, p. 9, Las Vegas, Nev, USA, September 2007.

[11] J. Perret-Liaudet, Y. Kadmiri, and E. Rigaud, "Automotive rattle noise: some theoretical results associated with the restitution coefficient law modelling teeth impacts," in *Proceedings of the Japan Society of Mechanical Engineers International Conference on Motion and Power Transmission*, Japan, May 2009.

[12] Y. Kadmiri, J. Perret-Liaudet, and E. Rigaud, "Experimental study of rattle noise in automotive gearboxes," in *Proceedings of the VDI International conference on Gears*, Munich, Germany, October 2010.

[13] S. N. Dogan, J. Ryborz, and B. Bertsche, "Rattling and clattering noise in automotive transmissions—simulation of drag torque and noise," in *Transient Processes in Tribology*, G. Dalmaz et al., Ed., pp. 109–119, Elsevier, New York, NY, USA, 2004.

[14] M. Barthod, B. Hayne, J. L. Tébec, and J. C. Pin, "Experimental study of dynamic and noise produced by a gearing excited by a multi-harmonic excitation," *Applied Acoustics*, vol. 68, no. 9, pp. 982–1002, 2007.

[15] M. Barthod and J. L. Tebec, "Auditory perception of noise known as rattle in gearboxes," *Acta Acustica*, vol. 91, no. 1, pp. 180–191, 2005.

[16] L. Irimescu, I. Musca, and S. Alaci, "Aspects theoriques et expérimentaux concernant le coefficient de restitution," The annals of university "Dunarea De Jos" of Galati, fascicle VIII, ISSN 1221-4590, Tribilogy.

Hindawi Publishing Corporation
Advances in Acoustics and Vibration
Volume 2011, Article ID 606087, 10 pages
doi:10.1155/2011/606087

Research Article

Modeling of Self-Vibratory Drilling Head-Spindle System for Predictions of Bearings Lifespan

F. Forestier,[1] V. Gagnol,[2] P. Ray,[2] and H. Paris[3]

[1] *LaMI Laboratory, Clermont Université, UBP, EA 3867, BP2235, 03101 Montlucon, France*
[2] *LaMI Laboratory, Clermont Université, IFMA, EA 3867, BP10448, 63000 Clermont-Ferrand, France*
[3] *G-SCOP Laboratory, G-SCOP, 46 Avenue Félix Viallet, 38031 Grenoble, France*

Correspondence should be addressed to F. Forestier, fabien.forestier@moniut.univ-bpclermont.fr

Received 13 January 2011; Accepted 7 June 2011

Academic Editor: Atma Sahu

The machining of deep holes is limited due to inadequate chip evacuation, which induces tool breakage. To limit this drawback, retreat cycles and lubrication are used. An alternative response to the evacuation problem is based on high-speed vibratory drilling. A specific tool holder induces axial self-maintained vibration of the drill, which enables the chips to be split. The chips are thus of a small size and can be evacuated. To anticipate the potential risk of decreased spindle lifespan associated with these vibrations, a model of the behavior of the system (spindle—self-vibrating drilling head—tool) is elaborated. In order to assess the dynamic behavior of the system, this study develops a rotor-based finite element model, integrated with the modelling of component interfaces. The current results indicate that the simulations are consistent with the experimental measurements. The influence of spindle speed and feed rate on bearing lifespan is highlighted.

1. Introduction

High-speed vibratory drilling allows chips to be split thanks to self-maintained vibration during cutting [1]. When these vibrations have a magnitude greater than the advance per tooth, the drill continuously enters and exits the material, which allows the fragmentation of the chips, as shown by Tichkiewitch et al. [2]. The chips are small and can thus be removed easily without retreat cycles or lubrication. High-speed vibratory drilling enables productivity to increase by a factor of three compared to traditional techniques. Currently, high-speed vibratory drilling is the only process capable of producing deep holes using high-speed machining centers, without lubricants, and with high productivity [3].

However, the excitation generated by the cutting process can also be a source of damage to the self-vibrating drilling head and the spindle. So the industrialization of high-speed vibratory drilling requires the effects of vibration on the machine, and more particularly on the spindle, to be predicted. For this purpose, a model of the dynamic behavior of the system (self-vibrating drilling head spindle) is elaborated from a realistic assembly of the components, in order to predict spindle bearing lifespan.

The SVDH is composed of an axial vibrating system, consisting of the SVDH vibrating subsystem, mounted on a specific HSK 63 taper, and called the SVDH body. The SVDH-vibrating subsystem is composed of the vibrating parts of the drill holder. The SVDH body guides the axial vibrating subsystem through a ball retainer and a classic HSK63 taper connexion with the spindle head. The self-excited vibrations must be tuned and controlled in order to have a magnitude greater than the advance per tooth. Mathematical models of the SVDH dynamics appearing in most of previous works lead to a one-dimensional linear or nonlinear model in the axial vibration direction governed by the mass, damping, and stiffness of the considered system [3]. In these studies, damping, which plays an important role in SVDH dynamic behaviour, is estimated but not experimentally identified. Moreover, the spindle behaviour and the interfaces between the spindle and the SVDH are assumed to be rigid and have not been taken into account. However, many works have showed that tool point dynamics can be significantly influenced by spindle dynamics, as well as the spindle-holder—tool interfaces. This creates a demand for predictive knowledge models that are capable of investigating the influence of cutting conditions on high-speed spindle-SVDH system.

Many authors have investigated the dynamic behaviour of machine tool spindle-bearing systems, both analytically and experimentally. They show that spindle dynamics are influenced by a large number of factors, including holder characteristics [4], spindle shaft geometry and drawbar force [5, 6], and the stiffness and damping provided by the bearings [7]. Most of these factors are independent of spindle speed, contrary to bearing properties [8, 9] and the spindle rotor dynamics, which change according to spindle speed. Such rotating systems have been successfully modelled through rotor-dynamics studies [10, 11]. In previous works [12, 13], a dynamic high-speed spindle-bearing system model based on rotor dynamics prediction was presented. Element kinematics were formulated in a corotational coordinate frame and enabled a special rotor beam element to be developed. Model results showed that spindle dynamics are influenced by the gyroscopic coupling and the spin softening of the rotating shaft due to high rotation speeds.

The literature on the modelling and analysis of spindles shows that the tool tip FRF is also greatly influenced by the contact dynamics of the spindle-holder-tool interfaces. The flexibility of the afore-mentioned interfaces can dominate the dynamics of the spindle. The tool tip FRF is usually obtained using experimental measurements, which require significant testing time to take into account the large number of spindle, holder, and tool combinations. Thus, semi-analytical approaches have been proposed to minimise experimental approaches. Erturk et al. [14] use a receptance coupling (RC) and structural modification method to connect the spindle shaft and the tool holder. Schmitz et al. [15] model the spindle holder experimentally and couple it with an analytical model of the overhang portion of the tool. Recent approaches consider distributed springs and dampers between the tool and the holder along the interface contact. [15, 16]. Contact stiffness and damping values alter the frequencies and peak values respectively of dominant tool tip vibration modes. The fast and accurate identification of contact dynamics in spindle-tool assemblies has become an important issue. Ren and Beards [17], Schmitz et al. [15], and Movahhedy and Gerami [18] treat identification as a nonlinear optimisation problem. Movahhedy and Gerami [18] uses a genetic algorithm to find the global minimum of the optimisation function

$$|g| = \left| \begin{Bmatrix} \mathrm{Re}\left(g_p - g_m\right) \\ \mathrm{Im}\left(g_p - g_m\right) \end{Bmatrix} \right|, \quad (1)$$

where g_p and g_m are, respectively, predicted and measured receptances of the assembly. Ozsahin et al. [19] present an original identification procedure based on experimental measurements. In their work, the elastic RC equations allow the stiffness and damping parameters of the spindle-tool assemblies to be obtained in closed-form expressions. In order to predict the drill dynamics and the adequate cutting conditions that lead to controlled self-excited vibrations, an accurate comprehensive dynamic model of the cutting process and spindle-SVDH dynamics is required.

In this paper, a hybrid model based on numerical and experimental approaches of the dynamic behavior of the system is proposed. This finite element model takes into account rotor dynamics effects, bearing stiffness and the real behavior of interfaces between different system components. The simulation allows achieving the best possible cutting parameters without damaging the bearings of the spindle.

In the second section, the spindle-SVDH rotor dynamics model is presented. A special rotor-beam element is implemented. The rolling bearing stiffness matrices are calculated around a static function point on the basis of Lim and Singh's [20] formulation and then integrated into the global finite element model. The identification of contact dynamics in tool-SVDH-spindle assemblies is carried out using the RC method on the basis of experimental substructure characterisation. The identified models are then integrated into the global spindle-SVDH-tool model. Finally, numerical and experimental tool tip FRF, in radial and axial directions, is compared in order to validate the global assembled model.

Section 3 is dedicated to the definition of optimal cutting conditions with respect to industrial objectives. The studied industrial context requires the maximum material cutting rate and a rational use of the tool-SVDH-spindle set in order to guarantee adequate rolling bearing lifespan. As a result, a recommendation for the use of a spindle-SVDH-tool set which respects the defined zone of interest, combining reli ability and productivity constraints, is proposed.

Finally, conclusions are presented.

2. Model Building

The vibratory drilling system is composed of a SVDH body clamped to the spindle by a standard HSK63A tool-holder interface. A SVDH-vibrating subsystem is jointed to the SVDH body with a specific spring and axially guided by a ball retainer. Finally, a long drill is held in the SVDH-vibrating subsystem with a standard ER25 collet chuck. The spindle has four angular bearings in overall back-to-back configuration (Figure 1).

The spindle-SVDH-tool finite element model is restricted to the rotating system composed of the spindle shaft, the SVDH and the drill. An experimental modal identification procedure was carried out on the different spindle substructures and showed that spindle behaviour can be restricted to rotating structure behaviour [12]. The interfaces represented by the HSK63 taper, spring and ball retainer, and collet chuck were taken into account in the model. The CNC milling machine structure was assumed to be infinitely rigid compared to the other parts of the system.

The numerical model of the spindle SVDH tool is based on the integration of the rotating system's finite element model (FEM), the rolling bearing model, and the interface model. Figure 2 summarises the various stages of model development. The system substructures were modelled through rotor-dynamics formulations. A readjustment procedure was carried out on undefined FEM material properties in order to fit model results to experimental ones. The receptance coupling method was used to identify the dynamic parameters of the system's interfaces. Once each structural subsystem model was validated, the identified interface

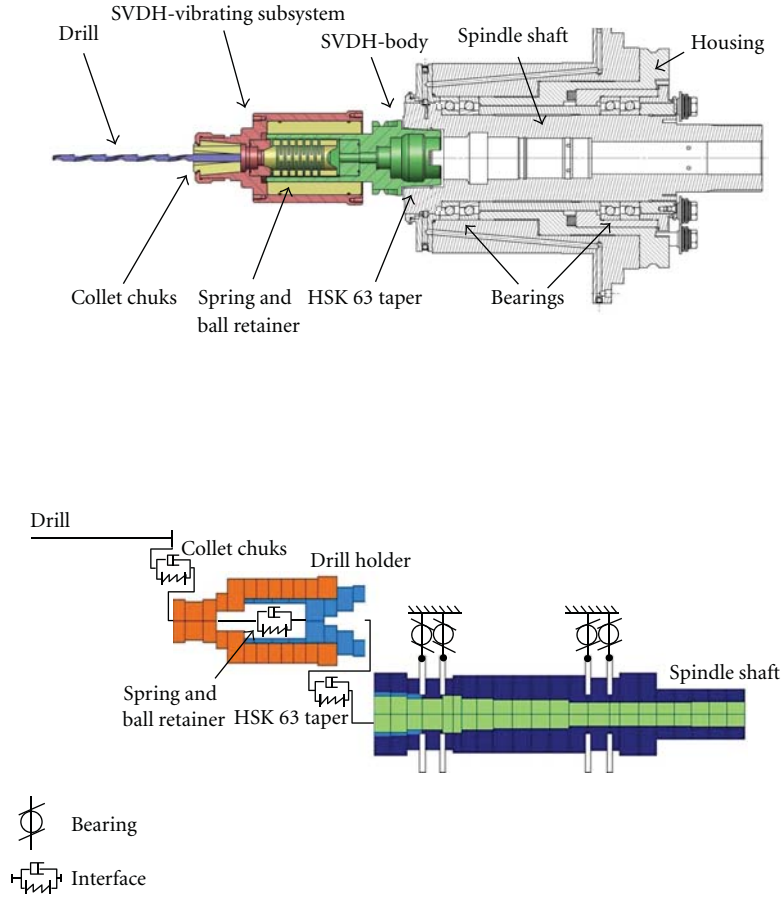

Figure 1: The spindle-SVDH-tool system and its finite element model.

behaviour parameters were integrated to obtain the assembled global model.

2.1. Modelling of Structural Subsystems. The spindle SVDH tool system is composed of four structural subsystems: the drill, the SVDH-vibrating subsystem, the SVDH body, and the spindle. The motion of the rotating structure is considered as the superposition of rigid and elastic body displacements. Dynamic equations were obtained using Lagrange formulation associated with a finite element method. Due to the size of the rotor sections, shear deformations had to be taken into account. Then, the rotating substructure was derived using Timoshenko beam theory. The relevant shape functions were cubic in order to avoid shear locking. A special three-dimensional rotor-beam element with two nodes and six degrees of freedom per node was developed in the corotational reference frame. The damping model used draws on *Rayleigh* viscous equivalent damping, which makes it possible to regard the damping matrix $\mathbf{D}$ as a linear combination of the mass matrix $\mathbf{M}$ and the spindle rigidity matrix $\mathbf{K}$

$$\mathbf{D} = a\mathbf{M} + b\mathbf{K}, \tag{2}$$

where a and b are damping coefficients.

The set of differential equations can be written as

$$\mathbf{M}(\mathbf{q}_N)\ddot{\mathbf{q}}_N + (\mathbf{C}(\mathbf{q}_N, \dot{\mathbf{q}}_N) + \mathbf{D})\dot{\mathbf{q}}_N + \mathbf{K}\mathbf{q}_N = \mathbf{F}(t), \tag{3}$$

where $\mathbf{M}$ is the mass matrix, and $\mathbf{C}$ matrix contains the rotational dynamics effects. $\mathbf{q}_N$ and $\mathbf{F}(t)$ are the nodal displacement and force vectors. An accelerating rotor gives rise to previous time-variant equations (3), but treatment of the rotor using a pseudoconstant speed approach can still be described by means of linear time-invariant models and is valid in many cases (4):

$$\mathbf{M}_0\ddot{\mathbf{q}}_N + (2\Omega\mathbf{G} + \mathbf{D})\dot{\mathbf{q}}_N + \left(\mathbf{K} - \Omega^2\mathbf{N}\right)\mathbf{q}_N = \mathbf{F}(t), \tag{4}$$

where $\mathbf{M}_0$ is the constant part of matrix $\mathbf{M}$, and $\mathbf{G}$ and $\mathbf{N}$ proceed from the decomposition of matrix $\mathbf{C}$.

2.2. Modelling Angular Contact Ball Bearings. The rotating system is supported by four (two front and two rear) hybrid angular contact bearings. The rolling bearing stiffness matrices were calculated using in-house software developed on the basis of Lim and Singh's [20] formulation. The bearing stiffness model represents the load-displacement relation combined with the Hertzian contact stress principle and was calculated around a static function point characterised by the bearing preload: δ. Based on Rantatalo's prediction [9],

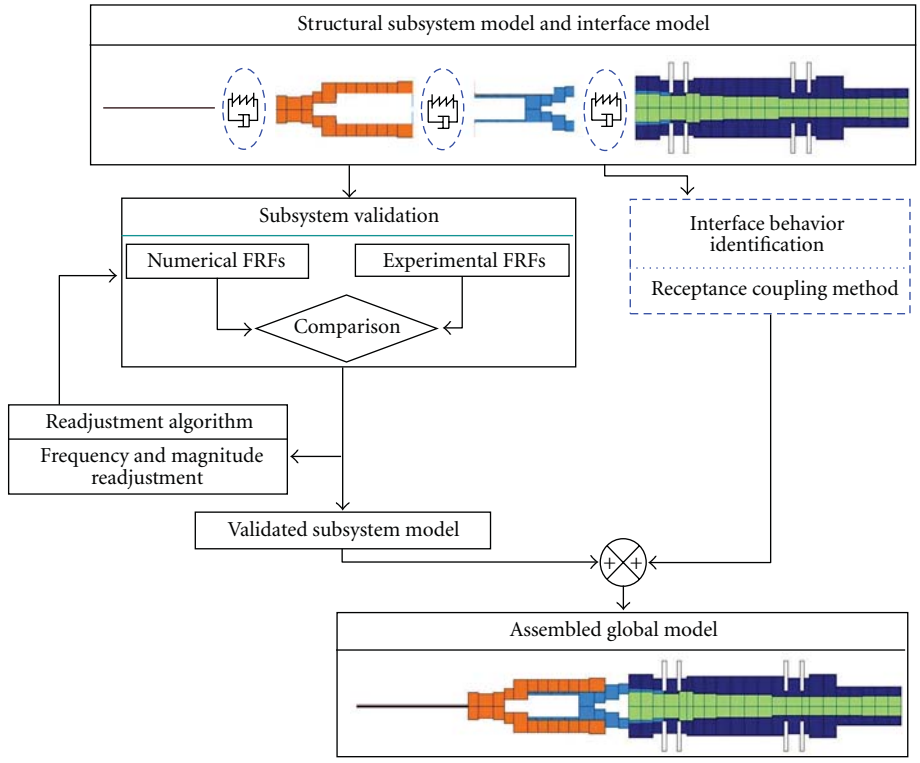

Figure 2: Development of the numerical model.

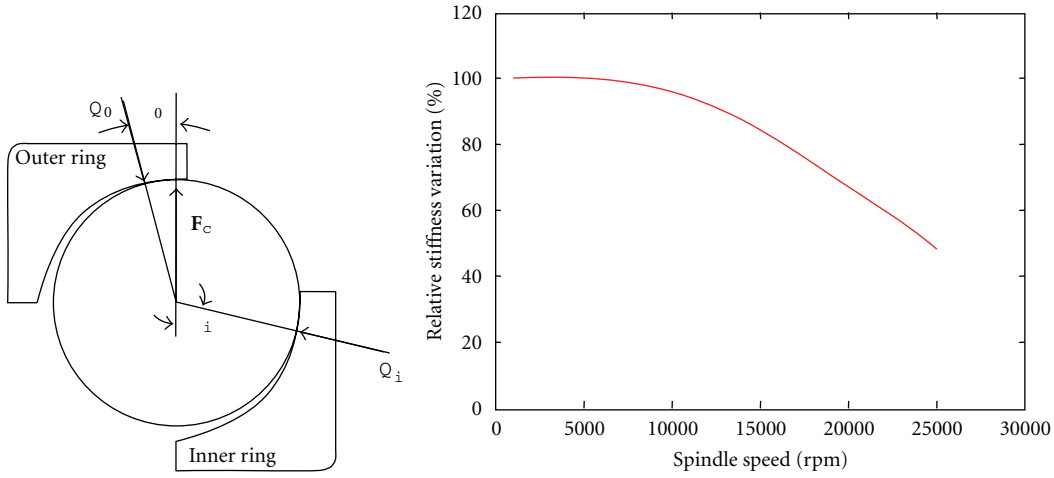

(a) Angular contact ball bearing Hertzian and centrifugal force

(b) Bearing stiffness variation

Figure 3: Bearing stiffness variation depending on spindle speed [12].

the initially calculated bearing stiffness is spindle speed dependent because of the gyroscopic and centrifugal force $\mathbf{F}_c$, which acts on each ball (Figure 3(a)). As the speed increased, the load conditions between the balls and the rings in the bearing changed because of the centrifugal force (Figure 3(a)). Then, speed-dependent bearing stiffness was integrated into the global spindle FEM and influenced the natural frequencies of the spindle-SVDH-tool unit under consideration.

2.3. Structural Systems Dynamic Readjustment. While detailed knowledge of the spindle-SVDH-tool system is in general not available in a manufacturing environment, models need to be readjusted in order to fit experimental results. The readjustment parameters are the Young modulus: E, the damping coefficients: (a, b), and the rolling bearing preload: δ. The readjustment procedure is proposed to tune the previous variable in order to fit the model results to the experimental frequency response function (FRF). These

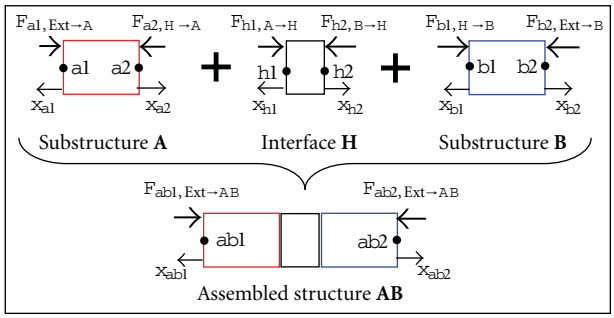

Figure 4: Receptance coupling notation.

parameters are readjusted by minimizing the gap between the measured and the modelled tool tip node FRF for nonrotating components, using an optimisation routine and a least squares type objective function defined as

$$r = \sum_{\omega=\omega_{\min}}^{\omega_{\max}} \left(\mathbf{H}_{\text{num}}(\omega,(E,a,b,\delta)) - \mathbf{H}_{\text{exp}}(\omega)\right)^2, \quad (5)$$

where $\mathbf{H}_{\text{num}}(\omega,(E,a,b,\delta))$ and $\mathbf{H}_{\text{exp}}(\omega)$ are, respectively, the numerical and experimental FRF.

2.4. Modelling and Identification of Spindle-SVDH-Tool Interfaces. The dynamic behaviour of the interfaces represented by the HSK63 taper, spring and ball retainer, and collet chuck was taken into account. The identification procedure of the interface models was based on the receptance coupling method.

2.4.1. Receptance Coupling Background. In this section, the RC equations are established. At the top of Figure 4, the substructure **A** and the substructure **B** are represented, connected by interface **H**. At the bottom of Figure 4, the assembled structure is represented. This figure enables the excitation point and the measurement points used in the receptance coupling approach to be located.

The notation $\mathbf{A_{ij}}(\omega) = (x_{ai}(\omega)/F_{aj,\text{Ext}\to A}(\omega))|_{F_{ak,\text{Ext}\to A}=0,\forall k\neq j}$ refers to the spatial receptance vector, whose output is the translation of point *ai* and whose input is the force at point *aj*, when all other forces applied to substructure **A** are zero. The receptance of the assembled structure $\mathbf{AB_{ij}}$ can be expressed according to the receptance of substructures $\mathbf{A_{ij}}$ and $\mathbf{B_{ij}}$ and the receptance of interface **H**. The movement equations of each end point of substructures **A** and **B** and of structure **AB** are written as shown in (6) to (8). The behaviour of the interface, assuming zero mass, is given in (9), and the compatibility conditions are written in (10).

Substructure **A**:

$$\begin{aligned} x_{a1} &= \mathbf{A_{11}}F_{a1,\text{Ext}\to A} + \mathbf{A_{12}}F_{a2,H\to A},\\ x_{a2} &= \mathbf{A_{21}}F_{a1,\text{Ext}\to A} + \mathbf{A_{22}}F_{a2,H\to A}. \end{aligned} \quad (6)$$

Substructure **B**:

$$\begin{aligned} x_{b1} &= \mathbf{B_{11}}F_{b1,H\to B} + \mathbf{B_{12}}F_{b2,\text{Ext}\to B},\\ x_{b2} &= \mathbf{B_{21}}F_{b1,H\to B} + \mathbf{B_{22}}F_{b2,\text{Ext}\to B}. \end{aligned} \quad (7)$$

Substructure **AB**:

$$\begin{aligned} x_{ab1} &= \mathbf{AB_{11}}F_{ab1,\text{Ext}\to AB} + \mathbf{AB_{12}}F_{ab2,\text{Ext}\to AB},\\ x_{ab2} &= \mathbf{AB_{21}}F_{ab1,\text{Ext}\to AB} + \mathbf{AB_{22}}F_{ab2,\text{Ext}\to AB}. \end{aligned} \quad (8)$$

Interface:

$$\begin{aligned} x_{h2} - x_{h1} &= \mathbf{H}F_{h2,B\to H},\\ F_{h2,B\to H} &= -F_{h1,A\to H}. \end{aligned} \quad (9)$$

Compatibility conditions:

$$\begin{aligned} x_{a1} &= x_{ab1},\\ x_{b2} &= x_{ab2},\\ x_{h1} &= x_{a2},\\ x_{h2} &= x_{b1},\\ F_{a2,H\to A} &= F_{h1,A\to H},\\ F_{b1,H\to \text{B}} &= F_{h2,B\to H},\\ F_{a1,\text{Ext}\to \text{A}} &= F_{ab1,\text{Ext}\to \text{AB}},\\ F_{b2,\text{Ext}\to B} &= F_{ab2,\text{Ext}\to AB}. \end{aligned} \quad (10)$$

By integrating the compatibility and interface equations ((9) and (10)) into (6) to (8), system (11) is obtained

$$\begin{aligned} &F_{ab1,\text{Ext}\to AB}(\mathbf{A_{11}} - \mathbf{AB_{11}}) + F_{a2,H\to A}(\mathbf{A_{12}})\\ &+F_{ab2,\text{Ext}\to AB}(-\mathbf{AB_{12}}) = 0,\\ &F_{ab1,\text{Ext}\to AB}(\mathbf{A_{21}}) + F_{a2,H\to A}(\mathbf{A_{22}} + \mathbf{B_{11}})\\ &+F_{ab2,\text{Ext}\to AB}(-\mathbf{B_{12}}) = 0,\\ &F_{ab1,\text{Ext}\to AB}(-\mathbf{AB_{21}}) + F_{a2,H\to A}(-\mathbf{B_{21}})\\ &+F_{ab2,\text{Ext}\to AB}(\mathbf{B_{22}} - \mathbf{AB_{22}}) = 0, \end{aligned} \quad (11)$$

$\mathbf{AB_{11}}$ and $\mathbf{AB_{21}}$ are elaborated from the definition of $\mathbf{AB_{ij}}(\omega) = (x_{abi}(\omega)/F_{abj,\text{Ext}\to AB}(\omega))|_{F_{abk,\text{Ext}\to AB=0,\forall k\neq j}}$, when $F_{ab2,\text{Ext}\to AB} = 0$ in (11). The receptance equations are obtained ((12)-(13))

$$\mathbf{AB_{11}} = \mathbf{A_{11}} - \mathbf{A_{12}}[\mathbf{B_{11}} + \mathbf{A_{22}} + \mathbf{H}]^{-1}\mathbf{A_{21}}, \quad (12)$$

$$\mathbf{AB_{21}} = \mathbf{A_{21}}[\mathbf{B_{11}} + \mathbf{A_{22}} + \mathbf{H}]^{-1}\mathbf{B_{21}}. \quad (13)$$

Similarly, to obtain $\mathbf{AB_{22}}$ and, $\mathbf{AB_{12}}$ it is sufficient to impose $F_{ab1,\text{Ext}\to AB} = 0$ in (11). Then the standard receptance equations are obtained(14)

$$\begin{aligned} \mathbf{AB_{22}} &= \mathbf{B_{22}} - \mathbf{B_{12}}[\mathbf{B_{11}} + \mathbf{A_{22}} + \mathbf{H}]^{-1}\mathbf{B_{21}},\\ \mathbf{AB_{12}} &= \mathbf{A_{12}}[\mathbf{B_{11}} + \mathbf{A_{22}} + \mathbf{H}]^{-1}\mathbf{B_{12}}. \end{aligned} \quad (14)$$

From the receptance of the system substructures $\mathbf{A_{ij}}, \mathbf{B_{ij}}$, associated with the interface model **H**, the reconstruction of the assembled structure FRF: $\mathbf{AB_{ij}}$ is possible.

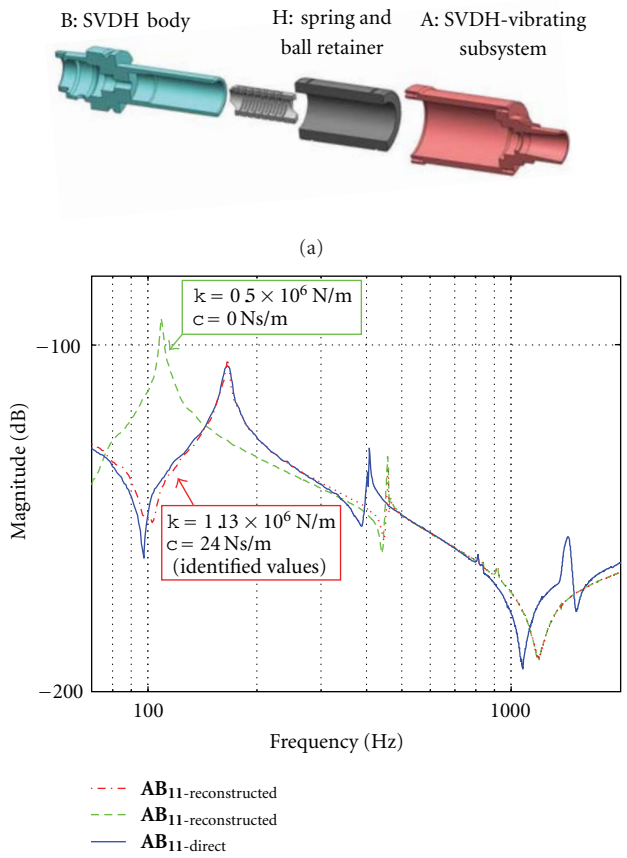

FIGURE 5: (a) Components (SVDH-body, SVDH vibrating subsystem) and interfaces (spring and ball retainer), (b) identification of the stiffness: k and the damping factor: c by minimizing the gap between $\mathbf{AB}_{11\text{-reconstructed}}$ and $\mathbf{AB}_{11\text{-direct}}$.

2.4.2. Application to the SVDH-Vibrating Subsystem/SVDH Body Interface. The interface between the SVDH-vibrating subsystem and the SVDH body is a prismatic joint whose axial stiffness is controlled by a spring. The SVDH-vibrating subsystem is guided in axial translation through a ball retainer, which controls the radial stiffness of the interface. Figure 5(a) shows these components. The axial dynamic behaviour of the interface was modelled using a spring damper: $\mathbf{H}_{\text{model}} = \mathbf{1}/(k + ic\omega)$. This interface was assumed to be rigid in the radial direction.

The k and c values were determined by minimizing the following r criteria:

$$r = \sum_{\omega=\omega_0-\varepsilon}^{\omega_0+\varepsilon} \left(\mathbf{AB}_{11\text{-reconstructed}}(\omega, k, c) - \mathbf{AB}_{11\text{-direct}}(\omega)\right)^2, \tag{15}$$

where $\mathbf{AB}_{11\text{-reconstructed}}$ and $\mathbf{AB}_{11\text{-direct}}$ represent, respectively, the RC-constructed FRF obtained by (12) and the measured FRF on the assembled system. ω_0 is the interface mode pulsation. The optimisation procedure was carried out on a 3 dB bandwidth around ω_0. In Figure 5(b), it can be noticed that the $\mathbf{AB}_{11\text{-reconstructed}}$ and $\mathbf{AB}_{11\text{-direct}}$ curves are in good agreement, which enables the spring-damper interface model and the identified values ($k = 1.13 \times 10^6$ N/m and $c = 24$ Ns/m) to be validated.

2.4.3. Application to the Collet Chuck Interface. The interface between the drill and the SVDH-vibrating subsystem is a collet chuck joint. Receptance $\mathbf{AB}_{21\text{-direct}}$ is preferred to $\mathbf{AB}_{11\text{-direct}}$ in order to facilitate the experimental identification procedure. Moreover, the mass of the accelerometer is not negligible compared to the mass of the drill. In addition, the SVDH-vibrating subsystem is not in the same material configuration when the collet chuck is tightened on a drill as when it is not. For these reasons, receptance $\mathbf{AB}_{21\text{-reconstructed}}$ (13) was obtained using numerical receptance for components A and B. The identification procedure provided collet chuck stiffness and damping factors of, respectively, 14.8×10^6 N/m and 4 Ns/m.

2.4.4. Application to the HSK 63 Taper Interface. The experimental modal analyses carried out on the spindle/SVDH body system in the axial direction allow the HSK 63 interface to be considered as a rigid connection (Figure 6). Indeed, no specific mode for the HSK 63 taper interface appears between 0 and 3000 Hz.

2.5. Model Assembly and Experimental Validation. As in a classic finite element procedure, dynamic equations of the overall system, composed of the drill, the SVDH-vibrating subsystems, the SVDH body, and the spindle, were obtained by assembling element matrices. The spring-damper connection parameters between the drill and the SVDH-vibrating subsystems and between the SVDH-vibrating subsystems and SVDH body, identified by the receptance coupling method, enabled the rotor-beam models of the components to be assembled.

The spindle-SVDH-tool assembled model was validated by comparison between numerical and experimental FRF, as shown in Figure 7.

Figure 7(a) represents experimental and numerical axial FRF of the assembled system. The 60 Hz and 4700 Hz modes are, respectively, due to the spring-ball retainer and collet chuck interfaces as mentioned in the previous subsystem identification procedure. Some parasitical experimental bending modes at 193 Hz, 1237 Hz, and 3433 Hz are present in the experimental FRF.

Figure 7(b) represents experimental and numerical radial FRF of the assembled system. The 193, 1237, and 3433 Hz modes are related to the drill's bending modes. The 376 Hz mode is controlled by the bearings. Additional numerical modes are present at 1830 and 3740 Hz. These frequency peaks are related to the dynamics behaviour of the rear side of the spindle. They do not appear in the experimental FRF since the displacements of the rear side of the real spindle are blocked by the motor. For the axial and radial FRF, a good correspondence between the numerical and experimental curves enabled the numerical model to be used for further investigations.

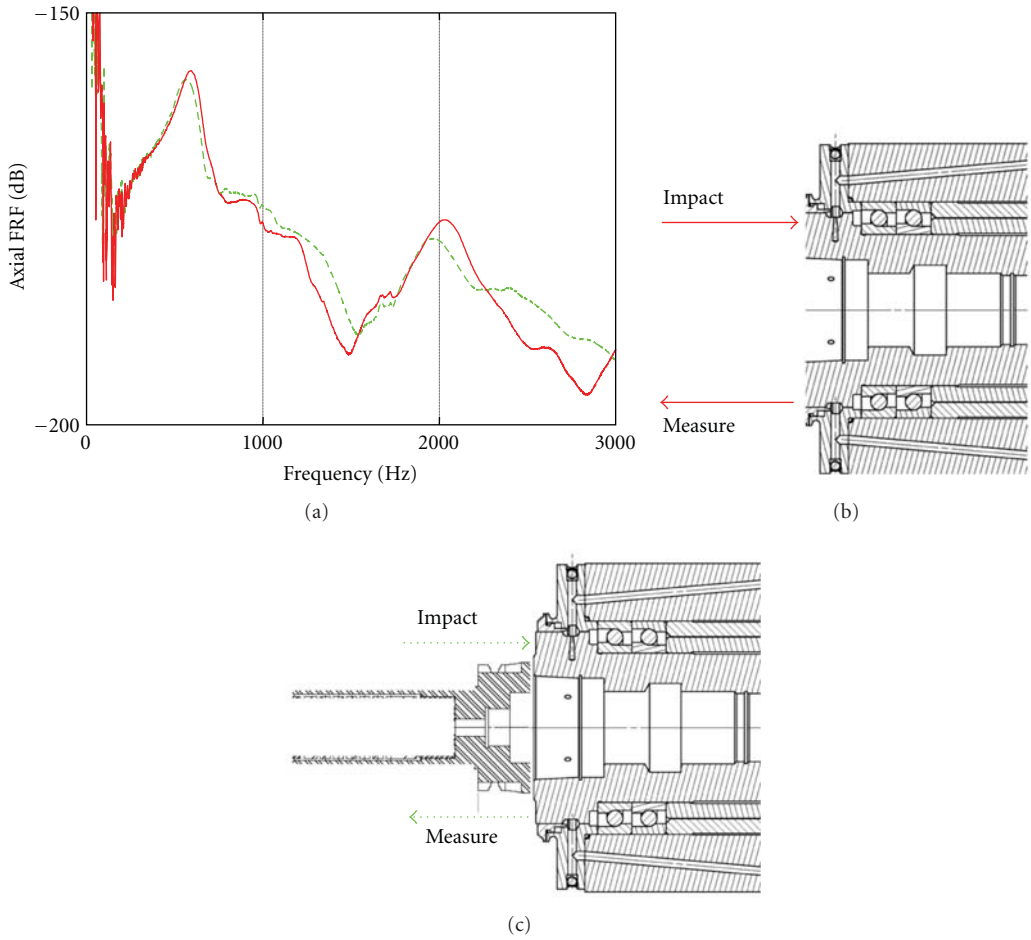

Figure 6: HSK 63 experimental modal analyses and associated axial FRF.

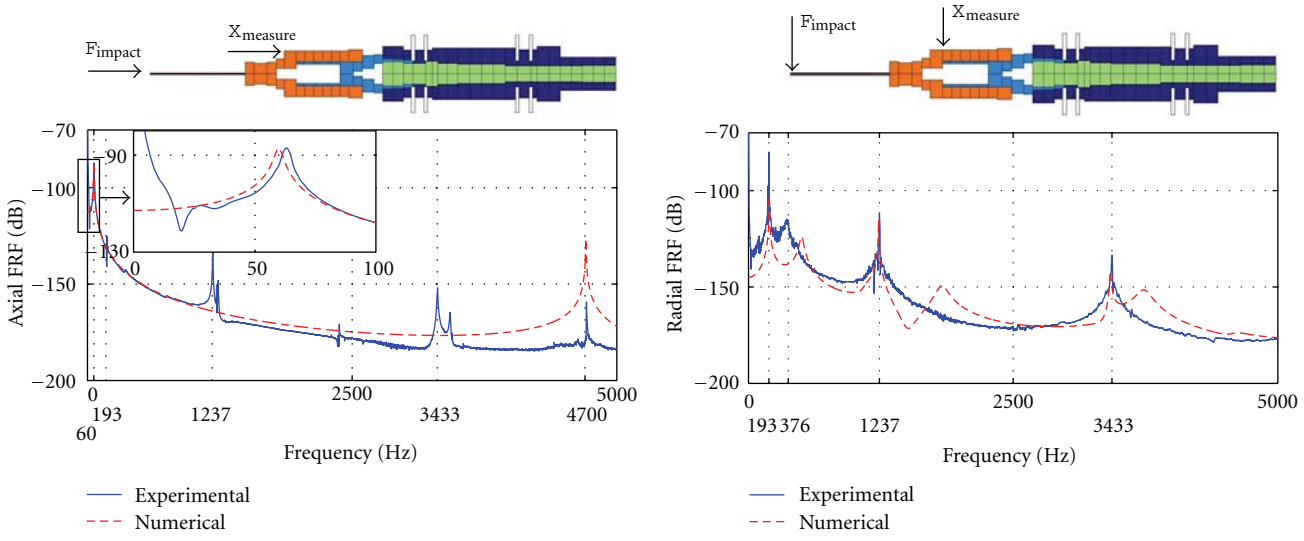

Figure 7: Numerical versus experimental system FRF.

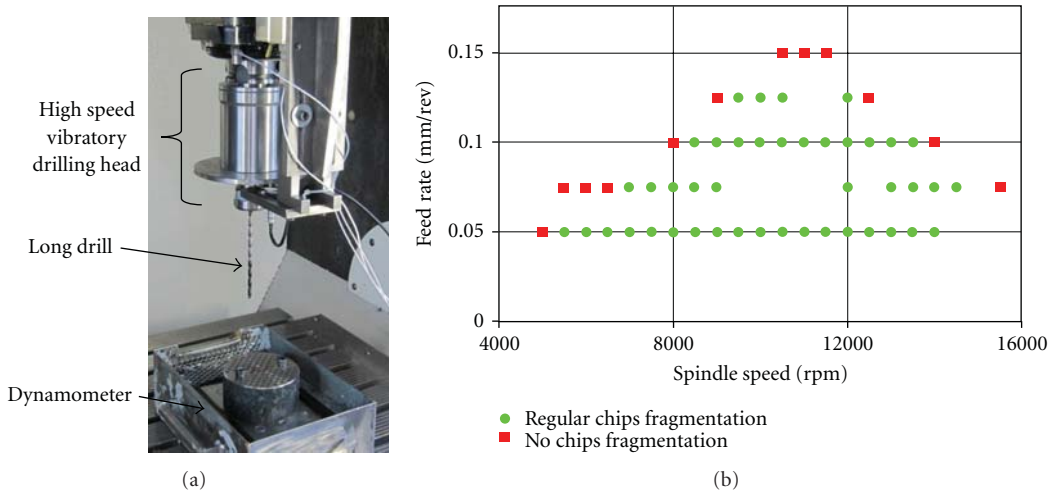

Figure 8: Experimental setup.

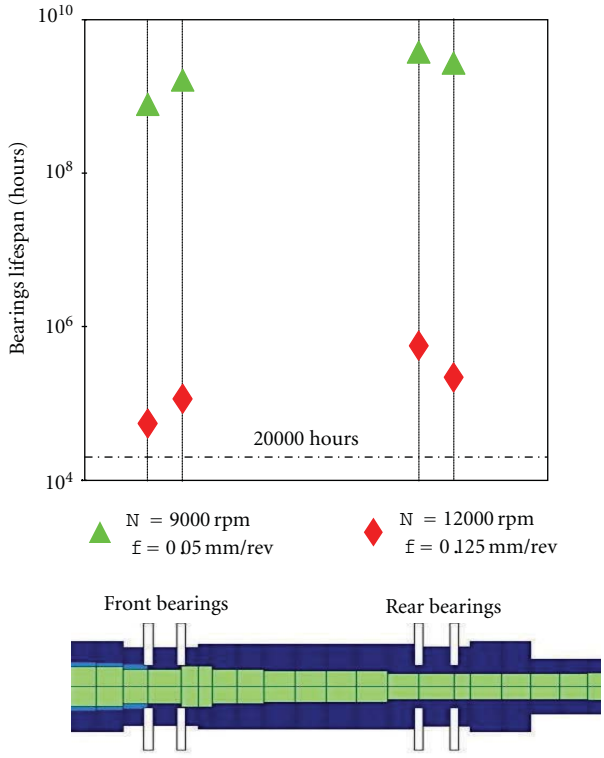

Figure 9: Influence of location and cutting conditions on bearings lifespan.

3. Bearing Lifespan Predictions

The industrial context of the proposed paper is to realize high-speed vibratory drilling operation, with a drill diameter of 5 mm, with a drill depth of 100 mm, without retreat cycles or lubrication, in a mass production system.

In this section, the numerical model will be used to predict bearings lifespan for various cutting conditions, in this context. The calculated bearing lifespan, thanks to experimental data, was compared to industrial recommendations in order to give rules of uses to obtain the maximum removal rate with respect to system lifespan.

For bearing lifespan calculations, experiments were carried out to measure the cutting force for different cutting conditions, using a three-component dynamometer (Kistler dynamometer type 9257B). High-speed vibratory drilling operations, representative of the industrial context, were performed on 35MnV7 steel, with a drill of 116 mm length and of 5 mm diameter. The experimental setup is represented in Figure 8(a). Rotation speed and feed rate were tested, respectively, between 5500 and 15500 rpm and between 0.05 and 0.15 mm/rev. Only the drilling operations that led to regular chips fragmentation were used to predict bearing lifespan, as shown in Figure 8(b). The time-variant value of the radial forces, which depends on the angular orientation of the cutter as it rotates through the cut, was expanded into a Fourier series and then truncated to include only the fundamental frequency. These forces, combined with the numerical FRF of the model, between the excitation node and the bearings nodes, allow the resulting rolling bearings solicitation to be determined. The rolling bearings lifespan is

$$L_h = \frac{10^6}{60N}\left(\frac{C}{P}\right)^3, \tag{16}$$

where C is the basic dynamic load and P the equivalent dynamic load in Newtons. N is the spindle speed in rpm. The values obtained are expressed in hours and can be compared to an industrial objective of 20000 hours.

3.1. Effect of Cutting Conditions on Bearing Lifespan. First, the bearings with the shortest lifespan is sought, because it is the element upon which the lifespan of the entire spindle depends. For all cutting conditions, the bearings with the shortest lifespan is always the front bearings. From Figure 9, which represents the extreme lifespan of the different bearings, the strong influence of the cutting conditions on the bearings lifespan can be noticed. Industrial recommendations for spindle lifespan are 20000 hours. The shortest calculated lifespan is 55000 and corresponds to the cutting

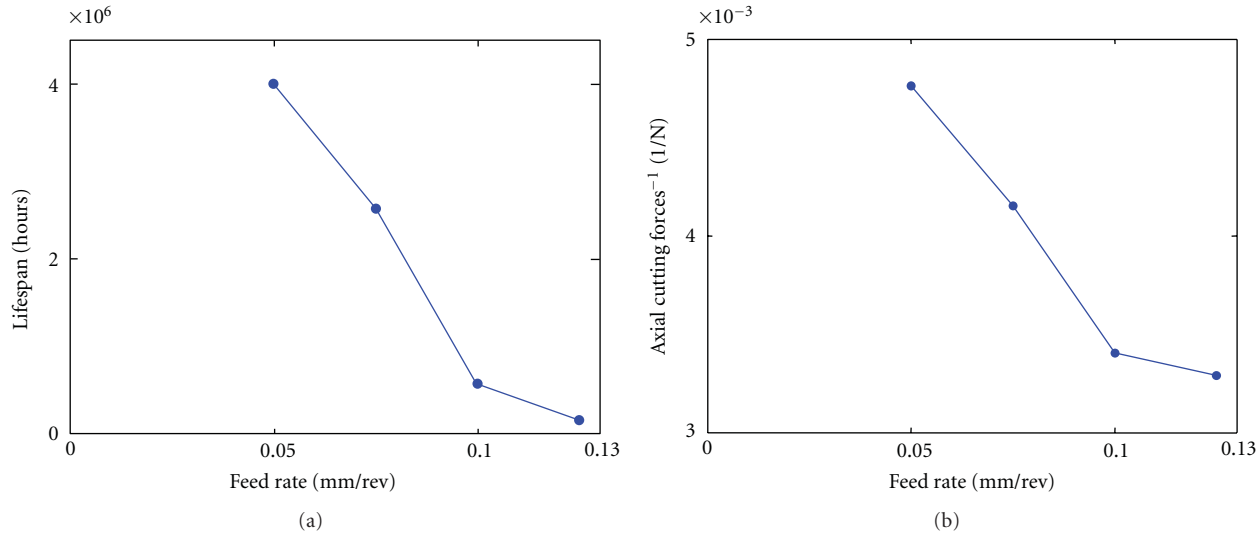

Figure 10: (a) Influence of feed rate on bearings lifespan, for a spindle speed of 12000 rpm, and (b) influence of the feed rate on the inverse of experimental axial cutting force magnitude.

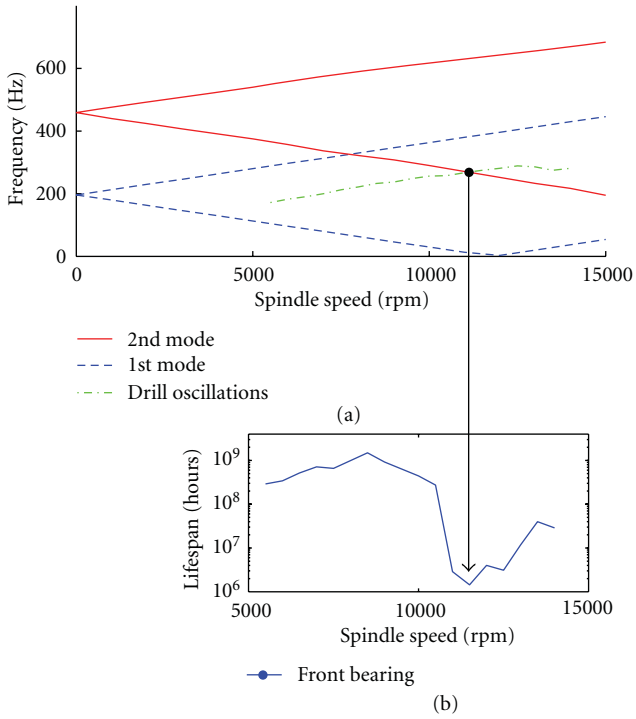

Figure 11: (a) Campbell diagram. (b) Influence of spindle speed on bearings lifespan, for a feed rate of 0.05 mm/rev.

conditions given rise to the best material removal rate (N = 12000 rpm, f = 0.125 mm/rev). Thus, a high-speed vibratory drilling operation is always compatible with industrial standards, even under the best material removal rate cutting conditions.

Figure 10(a) shows the influence of the feed rate on bearings lifespan, for a spindle speed of 12000 rpm. Only feed rates higher than 0.05 mm/rev were tested, because for feed rates below this limit, the productivity is too low and high-speed vibratory drilling loses its relevance. For feed rates higher than 0.125 mm/rev, no stable vibrations of the drill were obtained. The bigger the feed rate, the lower the bearings Lifespan. However, even the shortest bearings Lifespan is compatible with industrial standard. Hence, the optimal feed rate of 0.125 mm/rev is retained. Figure 10(b) shows that cutting forces are modified by the feed rate. Similarities between the curves in Figures 10(a) and 10(b) indicate that the bearing lifespan is mainly influenced by the feed rate.

Figure 11(b) shows the variations in bearing lifespan depending on spindle speed, for a feed rate of 0.05 mm per revolution. The curve enables the determination of a spindle speed at 8500 rpm which maximizes bearing Lifespan and a spindle speed at 11500 rpm which minimizes it. In order to optimize productivity, as shown on Figure 8(b), the recommended cutting spindle speed is 12000 rpm.

The curves of Figure 11 illustrate the dynamic effects due to high rotational speed, such as gyroscopic coupling and spin softening, on system behaviour, and hence on bearing lifespan. Figure 11(a) represents the effect of spindle speed on the first two radial modes of the system. The dotted line indicates the drill oscillation frequency and is plotted from experimental data measured during high-speed vibratory drilling operations. The critical speed, at 11500 rpm, corresponds to the intersection of the radial mode frequencies with the excitation line due to the drill oscillations.

4. Conclusions

In this paper, a comprehensive approach to developing a hybrid model of the dynamic behavior of the spindle self-vibratory drilling head—tool system has been proposed. This approach has resulted in a numerical model enriched with physical data. The various components of the system are modelled using a specific beam element, taking into account the gyroscopic effects, centrifugal forces, and shear deflection. The receptance coupling method is used to identify the dynamic behavior of the interface. The complete system is

then obtained by assembling the beam model of each component using spring-damper elements. Finally, the assembled model is validated by comparisons between numerical and experimental FRFs. The model is used to predict the influence of a high-speed vibratory drilling operation on the bearing lifespan. The predictions of bearing lifespan are used to give rules of uses of the high-speed vibratory drilling head.

Nomenclature

$\mathbf{A_{ij}}$:	receptance vector of system A
x_{ai}:	translation of point i of system A
$F_{aj,\text{Ext}\to A}$:	force applied to system A at point j
$\mathbf{H}_{\text{model}}$:	interface model receptance
k:	interface stiffness
c:	interface damping factor
$\mathbf{AB_{ij}}_{\text{-reconstructed}}$:	system AB receptance, reconstructed using receptance-coupling equations
$\mathbf{AB_{ij}}_{\text{-direct}}$:	system AB receptance, directly measured
$\mathbf{D}$:	damping matrix
a, b:	damping coefficients
$\mathbf{M}$:	mass matrix
$\mathbf{K}$:	stiffness matrix
$\mathbf{C}$:	rotational dynamic effects matrix
$\mathbf{G}$:	gyroscopic matrix
$\mathbf{N}$:	spin softening effects matrix
$\mathbf{\Omega}$:	rotor angular velocity
$\mathbf{q}_N$:	nodal displacement
$\mathbf{F}$:	force vector
E:	Young modulus
δ:	rolling bearing preload
N:	spindle speed in rpm
L_h:	bearing lifespan
C:	basic dynamic load
P:	equivalent dynamic bearing load.

References

[1] A. M. Gouskov, S. A. Voronov, and S. A. Batzer, "Chatter synchronization in vibratory drilling," in *Proceedings of the American Society of Mechanical Engineers*, vol. 68, pp. 263–270, 2000.

[2] S. Tichkiewitch, G. F. Moraru, D. Brun-Picard, and A. Gouskov, "Self-excited vibration drilling models and experiments," *CIRP Annals*, vol. 51, no. 1, pp. 311–314, 2002.

[3] N. Guibert, H. Paris, and J. Rech, "A numerical simulator to predict the dynamical behavior of the self-vibratory drilling head," *International Journal of Machine Tools and Manufacture*, vol. 48, no. 6, pp. 644–655, 2008.

[4] J. Agapiou and C. Rivin, "Toolholder/spindle interfaces for CNC machine tools," *CIRP Annals*, vol. 44, no. 1, pp. 383–387, 1995.

[5] S. Smith, W. R. Winfough, and J. Halley, "The effect of drawbar force on metal removal rate in milling," *CIRP Annals*, vol. 48, no. 1, pp. 293–296, 1998.

[6] S. Jiang and S. Zheng, "A modeling approach for analysis and improvement of spindle-drawbar-bearing assembly dynamics," *International Journal of Machine Tools and Manufacture*, vol. 50, no. 1, pp. 131–142, 2010.

[7] A. Erturk, H. N. Ozguven, and E. Budak, "Effect analysis of bearing and interface dynamics on tool point FRF for chatter stability in machine tools by using a new analytical model for spindle-tool assemblies," *International Journal of Machine Tools and Manufacture*, vol. 47, no. 1, pp. 23–32, 2007.

[8] B. R. Jorgensen and Y. C. Shin, "Dynamics of spindle-bearing systems at high speeds including cutting load effects," *Journal of Manufacturing Science and Engineering*, vol. 120, no. 2, pp. 387–394, 1998.

[9] M. Rantatalo, J. O. Aidanpaa, B. Goransson, and P. Norman, "Milling machine spindle analysis using FEM and non-contact spindle excitation and response measurement," *International Journal of Machine Tools and Manufacture*, vol. 47, no. 7–8, pp. 1034–1045, 2007.

[10] H. Li and Y. C. Shin, "Integrated dynamic thermo-mechanical modeling of high speed spindles, part 1: model development," *Journal of Manufacturing Science and Engineering*, vol. 126, no. 1, pp. 148–158, 2004.

[11] Y. Cao and Y. Altintas, "Modeling of spindle-bearing and machine tool systems for virtual simulation of milling operations," *International Journal of Machine Tools and Manufacture*, vol. 47, no. 9, pp. 1342–1350, 2007.

[12] V. Gagnol, C. B. Bouzgarrou, P. Ray, and C. Barra, "Model-based chatter stability prediction for high-speed spindles," *International Journal of Machine Tools and Manufacture*, vol. 47, no. 7-8, pp. 1176–1186, 2007.

[13] I. Mane, V. Gagnol, B. C. Bouzgarrou, P. Ray, and C. Berra, "Stability-based spindle speed control during flexible workpiece high-speed milling," *International Journal of Machine Tools and Manufacture*, vol. 48, no. 2, pp. 184–194, 2008.

[14] A. Erturk, H. N. Ozguven, and E. Budak, "Analytical modeling of spindle-tool dynamics on machine tools using Timoshenko beam model and receptance coupling for the prediction of tool point FRF," *International Journal of Machine Tools and Manufacture*, vol. 46, no. 15, pp. 1901–1912, 2006.

[15] T. L. Schmitz, K. Powell, D. Won, G. S. Duncan, W. G. Sawyer, and J. C. Ziegert, "Shrink fit tool holder connection stiffness/damping modeling for frequency response prediction in milling," *International Journal of Machine Tools and Manufacture*, vol. 47, no. 9, pp. 1368–1380, 2007.

[16] H. Ahmadian and M. Nourmohammadi, "Tool point dynamics prediction by a three-component model utilizing distributed joint interfaces," *International Journal of Machine Tools and Manufacture*, vol. 50, no. 11, pp. 998–1005, 2010.

[17] Y. Ren and C. F. Beards, "Identification of joint properties of a structure using FRF data," *Journal of Sound and Vibration*, vol. 186, no. 4, pp. 567–587, 1995.

[18] M. Movahhedy and J. Gerami, "Prediction of spindle dynamics in milling by sub-structure coupling," *International Journal of Machine Tools and Manufacture*, vol. 46, no. 3-4, pp. 243–251, 2006.

[19] O. Ozsahin, A. Erturk, H. N. Ozguven, and E. Budak, "A closed-form approach for identification of dynamical contact parameters in spindle-holder-tool assemblies," *International Journal of Machine Tools and Manufacture*, vol. 49, no. 1, pp. 25–35, 2009.

[20] T. C. Lim and R. Singh, "Vibration transmission through rolling element bearings, part I to part III," *Journal of Sound and Vibration*, vol. 139, no. 2, pp. 179–199, 201–225, 1990.

Hindawi Publishing Corporation
Advances in Acoustics and Vibration
Volume 2011, Article ID 952407, 12 pages
doi:10.1155/2011/952407

Research Article

Stochastic BEM for the Vibroacoustic Analysis of Three-Dimensional Structures

R. D'Amico, A. Pratellesi, M. Pierini, and N. Baldanzini

Dipartimento di Meccanica e Tecnologie Industriali, Università degli Studi di Firenze, Via di Santa Marta 3, 50139 Firenze, Italy

Correspondence should be addressed to R. D'Amico, roberto.damico@unifi.it

Received 14 January 2011; Revised 24 April 2011; Accepted 24 May 2011

Academic Editor: Kok Keong Choong

Nowadays, extending the NVH prediction reliability to the whole frequency range is an attractive goal of vibroacoustics. Deterministic methodologies are well established for the low-frequency range, but, decreasing the wavelength, energy-based methods are necessary. In such a range, a crucial role is played by small perturbations which highly influence the response sensitivity. Moreover, taking into account these variations allows to make the product design more robust and even quicker. Introducing geometrical uncertainties within the classic BEM formulation allows to obtain the so-called stochastic BEM. As a result, the solution shows deterministic behaviour at low frequencies; decreasing the wavelength, the effect of the uncertainties smooths the response. Consequently, it is possible to obtain an averaged trend over the whole frequency range which asymptotically tends to the deterministic one. In this paper, we deal with three-dimensional acoustic SBEM. First, the formulation and its basic assumptions are presented. Secondly, they are applied to academic cases to show its potentialities in predicting vibroacoustic behaviour over a wide frequency range.

1. Introduction

To correctly predict the midfrequency behaviour of structures is a crucial objective of vibro-acoustics. Generally, a mechanical structure is a system made by several components with different geometrical and material properties which consequently exhibit different vibro-acoustic behaviours. The prediction becomes even more problematic if uncertainties and perturbations are taken into account in the analysis.

Depending on the structure dimension, the whole frequency range can be split in three domains. The low-frequency domain is characterized by a long wavelength in in respect to the system dimension. In the high-frequency range, the wavelength is much smaller respect to such a dimension. Finally, a transition region exists, the so-called midfrequency range.

Deterministic techniques as finite element method (FEM) [1] and boundary element method (BEM) [2, 3] guarantee a reliable prediction at low-frequencies. The current computational resources allow these numerical methods to be efficient even for complex structures as far as the low-frequency domain is concerned. Nevertheless, the smaller the wavelength, the more refined the discretization required and is obtaining an accurate prediction becomes very demanding. However, deterministic methods can be pushed up in frequency by means of stabilization and accelerating techniques, and it becomes possible to use them in the middle range. Fast multipole methods [4] and domain decomposition and stabilized FE [5] are enhancements of, respectively, classic BEM and FEM to shift their usage up to higher frequencies. A novel wave based method (WBM) [6] allows avoiding large computational resources and model discretization.

At low frequencies, material properties and geometry behaviour are known with sufficient precision and the response is not so sensitive to variations. At high-frequencies model properties are highly uncertain, and the solution is very sensitive to small perturbations. Manohar and Keane [7, 8] highlight these effects computing the eigenfrequency density functions of a beam whose mass density is affected by random uncertainty. Moreover, according to Fahy and Mohammed [9], the differences among systems, which share the same design characteristics and the effects of these

differences on vibrational behaviour, are individually unpredictable in the high-frequency range, therefore a probabilistic model is appropriate. The effect of this sensitiveness can be seen in Figure 1. The FRFs of a plane plate, obtained with a Monte Carlo simulation, varying the geometrical and physical parameters (length, thickness, width, Young modulus, and density), show that above 100 Hz it is no more possible to have a precise and defined response, but a spread of results [10]. The average of the spread can be efficiently represented by a smoothened curve which neglects the local peak but predicts the overall trend. Consequently, using deterministic techniques over the whole frequency range becomes meaningless.

The statistical energy analysis (SEA) [11] is a widely employed tool to solve many acoustic and vibration problems in the high frequency range [12]. For SEA, the power transfer between subsystems is proportional to the difference of the model energy levels in the subsystems. As a hypothesis, the structure has to be nonzero damped, input powers uncorrelated, and the subsystems weakly coupled. Moreover, the modal density of each subsystem has to be high. In addition, even if large literature exists, the determination of coupling loss factors, which regulate the energy exchange between subsystems, and the discretization of systems are still crucial aspects to build a reliable model [13]. Moreover, variations in energy density within the subsystem are not taken in account and it is not possible to control directly the uncertainties on the model. To tackle the first issue, the virtual SEA [14] has been carried out. The novelty of the method consists of the development of a frequency dependent procedure for defining the classic SEA subsystem.

Promising approaches are the wave and finite element method (WFE) [15] and the waveguide finite element method [16] to model the structure dynamics which are piecewise homogeneous or periodic in one or two dimensions or which are axisymmetric. The wave methods allow to reduce considerably the dimension of the problem and thus the effort for calculations.

In the midfrequency range complex structures can be classified as comprised of two classes of subsystems, respectively, exhibiting an LF and a HF behaviour. To deal with the modelling requirements, hybrid approaches, which merge deterministic and energy methods, have been developed. Shorter and Langley [17] developed the a hybrid method to couple FE and SEA. Stiff components are modelled with FE since they have low modal density, flexible components are analysed with SEA since they have high modal density [18].

In the high-frequency range it has been proven that the flow of vibrational energy between weakly coupled subsystems is analogous to the way in which heat flows between two bodies of different temperature in a thermal analysis. Starting from the previous assumption, the Energy Flow Method (EFM) approaches the vibro-acoustic analysis in the HF range using a heat-conduction analogy. The method is derived from a local energy balance leading to a constitutive relationship analogous to the heat conduction equation [19]. Energy variations are smoother than displacement, thus an energy flow approach is more efficient even for high-order modes. Moreover, the numerical cost for solving

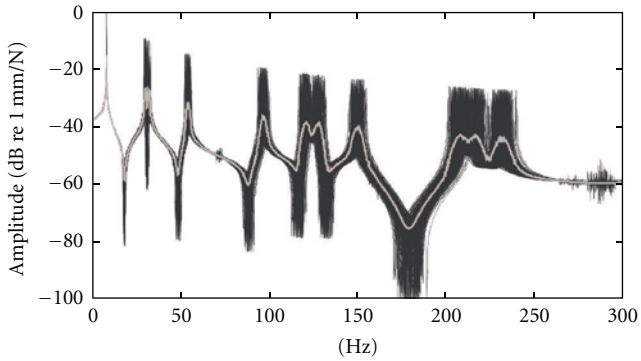

Figure 1: From [10], FRFs functions of a plane plate, varying the geometrical and physical parameters. Mean value (grey line) and spread (black).

the thermal problem is reduced compared to the wave-based approach. Many applications of these methods were proposed in the past. In particular, Wohlever, Bouthier, and Bernhard give some results regarding the energy models of rods, Euler-Bernoulli beams [20], membranes [21] and Kirchoff-Love plates [22] applying the power flow analysis. This formulation is obtained computing the real part of the harmonic energy flow balance. The near field contribution is assumed equal to zero, finally the spatial average operation allows obtaining a relation between the total energy density and the active power flow. Lase et al. [23], Ichochou et al. [24] developed the General Energy Method (GEM) for rods and beams. This method consists of expliciting the different terms of the harmonic complex energy flow balance. In this way, energy density, active power flow, Lagrangian density, and reactive power flow are obtained using a wave description. The application of some high-frequency assumptions leads to a simplified energy method (SEM). Lagrangian density and reactive power flow are assumed negligible, since their frequency average are equal to zero. This corresponds to neglecting the evanescent wave field far from the loadings and structure discontinuities, and the interfaces between the propagative waves are not taken for granted.

Solving the problem using these formulations requires the definition of power boundary conditions which are difficult to evaluate. Usually they are replaced by the power associated to infinite or semi-infinite structure. Viktorovitch et al. [25, 26] shows that the same power flow analysis and simplifed energy method formulations can be obtained introducing random parameters in the description of the geometrical parameters of the structure. The stochastic approach leads to a smooth response which is strongly influenced by the uncertainty. As a result, the higher the uncertainty, the smoother the response. Moreover, at high frequencies this formulation converges asymptotically to the SEM curve which is the response of the infinite system.

The capability to predict effects of uncertainties also has a direct impact on the product design. Indeed, during the industrialization process, small variations and irregularities are present and influence the vibro-acoustic behaviour of the whole structure, especially at high frequencies. This makes

the classical deterministic approaches not reliable. Obtaining the average behaviour allows to avoid a demanding Monte Carlo analysis or other sampling procedure, but still to deliver a robust design.

Viktorovitch et al. [27, 28] also introduced the so-called Smooth Integral Formulation (SIF) for one- and two-dimensional cases. This approach leads to a boundary integral formulation coupled with a statistical approach to account for uncertainties in the structural parameters. Introducing randomness to the geometrical or/and material properties of the structure leads to a precise description of the deterministic low frequency response and a smooth response in the high frequency field. This corresponds to the average of the strongly oscillating vibratory response which is solved in one go instead of using a sampling procedure. The starting point for SIF is the direct BEM formulation with the addition of supplementary equations which represent the energetic part of the problem. Differently from the well-known statistical methods, SIF allows to directly control the uncertainties on the model shape. As a result, when the frequency increases and the deterministic solution of the nominal structure starts to be meaningless, the SIF response allows to take into account effects of uncertainties presenting a smoothing behaviour towards an energetic description. On the other hand, if we want to use the energy methods in the midfrequency range, their assumptions become no longer valid. On the contrary, the SIF provides an averaged behaviour of the perturbed system. Since the stochastic approach is applied to a standard BEM formulation, the method is called stochastic boundary element method (SBEM).

Pratellesi et al. [29, 30] and Viktorovitch and Pratellesi [31] developed a hybrid formulation to couple SBEM, employed for the high-frequency part, with the finite element description of the low frequency behaving subsystems. The coupling allows to account for both deterministic and statistical contributions in the response of the structure and therefore to obtain a consistent formulation for the midfrequency range. Application cases were extended to one and two dimensions.

In this paper, SBEM methodology is applied to three-dimensional vibro-acoustic cases. First of all, a description of the methodology is presented. Uncertainties are applied to the expectation of the classic BEM formulation. Successively, additional relations are used to model the energetic part of the system. To prove the applicability of SBEM, a rectangular and a spherical acoustic cavity, with different degree of uncertainty, are investigated using SBEM. Results are shown both as deformed shape of a field mesh plane and response function computed at a solution point. Finally, conclusions are drawn, and further steps in research are highlighted.

2. The Boundary Element Method

Many problems related to steady-state oscillations lead to the Helmholtz equation,

$$\nabla^2 p(\mathbf{x}) + k^2 p(\mathbf{x}) = 0 \quad \text{on } D, \tag{1}$$

where p is the acoustic pressure at $\mathbf{x}$, k is the wavenumber ω/c, ω is the circular frequency, c is the speed of sound and D is the domain. The boundary element method allows to find an approximate solution to the problem in (1) with proper boundary conditions. In order to obtain the boundary integral formulation, (1) is integrated twice via Green's theorem over one side of the domain, using free space Green's functions

$$G(\mathbf{x},\mathbf{y}) = \frac{e^{-ikr}}{4\pi r}, \tag{2}$$

where $r = |\mathbf{x} - \mathbf{y}|$. This leads to the Helmholtz integral equation

$$c_s(\mathbf{x})p(\mathbf{x}) = \int_{D_f} f(\mathbf{y})G(\mathbf{x},\mathbf{y})dV + \int_{\partial D} p(\mathbf{y})dG(\mathbf{x},\mathbf{y})ds - \int_{\partial D} G(\mathbf{x},\mathbf{y})dp(\mathbf{y})ds, \tag{3}$$

denoting with dp the derivative of the pressure p and dG the derivative of the Green kernel, both with respect to the variable $\mathbf{x}$. D_f is the domain in which f is defined. Moreover, $c_s(\mathbf{x})$ is a coefficient dependent on the position of the point $\mathbf{x}$. If $\mathbf{x}$ is inside the domain c_s is equal to 1, if it is outside the domain c_s is equal to 0, and if it is on an approximately smooth boundary ∂D, c_s is equal to 1/2. Let us apply on ∂D_p pressure boundary condition

$$p(\mathbf{x}) = \hat{p}(\mathbf{x}) \quad \text{on } \partial D_p, \tag{4}$$

and velocity boundary condition on ∂D_v

$$dp(\mathbf{x}) = \hat{d}p(\mathbf{x}) \quad \text{on } \partial D_v. \tag{5}$$

∂D_p and ∂D_v constitute partitions of ∂D. A proper discretization of the boundary allows to write the fundamental BEM equation

$$c_s p(\mathbf{x}) = \int_{D_f} f(\mathbf{y})G(\mathbf{x},\mathbf{y})dV + \sum_{j=1}^{N_v} \int_{\partial D_v} \left[p_j dG(\mathbf{x},\mathbf{y}) - d\hat{p}_j G(\mathbf{x},\mathbf{y}) \right] ds + \sum_{k=1}^{N_p} \int_{\partial D_p} [\hat{p}_k dG(\mathbf{x},\mathbf{y}) - dp_k G(\mathbf{x},\mathbf{y})] ds. \tag{6}$$

Firstly the unknowns are computed at the nodes of the boundary, secondly the response is evaluated projecting these boundary contributions at a field solution point.

3. The Stochastic Boundary Element Method

3.1. Overview of the Random Formulation. Classic BEM provides a deterministic and reliable prediction in a low-frequency range. Decreasing the wavelength, sensitivity to small perturbation becomes higher and BEM fails to provide a useful representation of the vibro-acoustic phenomena.

The SBEM formulation allows to obtain an averaged behaviour over the whole frequency range. Indeed, the prediction is deterministic at low frequencies, where effect of perturbations are negligible. Increasing the frequency, the SBEM takes into account uncertainties achieving a smoothened response.

Many kinds of uncertainties can affect the structure characteristics. In this work we deal with geometrical ones, thus we suppose that the shape of the model and excitation points are perturbed. This is due to the fact that introducing other kind of uncertainties would produce a formulation much more difficult to handle.

Randomized boundary parameters and force application points are expressed as follows

$$\widetilde{x}_i = x_i + \epsilon_i, \tag{7}$$

where x_i is the deterministic value of the parameter while ϵ_i is the zero mean random variable. To solve the formulation, a statistic probability distribution should be introduced. It can assume different shapes, Gaussian, triangular, rectangular, hyperbolic, and so forth. The overall density function of the random variables can be evaluated for n independent random variables as

$$f_{\epsilon_1,\ldots,\epsilon_n}(y_1,\ldots,y_n) = \prod_{i=1}^{n} f_{\epsilon_i}(y_i). \tag{8}$$

The expectation of a generic function of n variables $h(\widetilde{y}_1,\ldots,\widetilde{y}_n)$, where each variable y_i has a distribution $f(y_i)$, is

$$\langle h(\widetilde{y}_1,\ldots,\widetilde{y}_n)\rangle = \int_{-\infty}^{+\infty}\cdots\int_{-\infty}^{+\infty} h(y_1,\ldots,y_n)\prod_{i=1}^{n} f_{\epsilon_i}(y_i)\,ds. \tag{9}$$

Directly computing the expectation of the boundary element formulation (6), we can evaluate the first-order moment (FOM) of the variable. This quantity does not give interesting information about the system behaviour because increasing the frequency, the first order moment vanishes to zero. Multiplying FOM equations by well-chosen variables, it is possible to obtain the second order Moments of the unknowns. As we previously said, energy variations are smoother than displacement and using an energy flow to evaluate the response is more efficient. Since the second order moments are quantities strictly related to an energy description of the vibrational behaviour, they do not converge to zero but, as the frequency increases, give a smooth trend. Moreover, the high the uncertainty level, the smoother the prediction.

In order to obtain the second order moments of the variables, let us consider (6) computed at point $\widetilde{\mathbf{x}}_i \in \partial\widetilde{\Omega}_v$, multiply it by the complex conjugate of the unknown variable $\widetilde{p}_i^*$ and finally compute the expectation of the product. Using the linearity property of the expectation operator, we obtain (10) expression

$$\begin{aligned}
\frac{1}{2}\left\langle |\widetilde{p}_i|^2\right\rangle &= \left\langle \widetilde{p}_i^* \int_{\widetilde{D}_f} f(\mathbf{y})G(\mathbf{y},\widetilde{\mathbf{x}}_i)\,dV\right\rangle \\
&+ \left\langle \widetilde{p}_i^* \sum_{\substack{j=1\\ j\neq i}}^{N_v} \widetilde{p}_j \int_{\partial\widetilde{D}_j} dG(\mathbf{y},\widetilde{\mathbf{x}}_i)\,ds\right\rangle \\
&- \left\langle \widetilde{p}_i^* \sum_{j=1}^{N_v} \int_{\partial\widetilde{D}_j} \widehat{d}p_j G(\mathbf{y},\widetilde{\mathbf{x}}_i)\,ds\right\rangle \\
&+ \left\langle \widetilde{p}_i^* \sum_{k=1}^{N_p} \int_{\partial\widetilde{D}_k} \widehat{p}_k dG(\mathbf{y},\widetilde{\mathbf{x}}_i)\,ds\right\rangle \\
&- \left\langle \widetilde{p}_i^* \sum_{k=1}^{N_p} \widetilde{d}p_k \int_{\partial\widetilde{D}_k} G(\mathbf{y},\widetilde{\mathbf{x}}_i)\,ds\right\rangle \\
&+ \left\langle |\widetilde{p}_i|^2 \int_{\partial\widetilde{D}_i} dG(\mathbf{y},\widetilde{\mathbf{x}}_i)\,ds\right\rangle.
\end{aligned} \tag{10}$$

On the other hand, we can consider (6) computed at point $\widetilde{\mathbf{x}}_i \in \partial\widetilde{\Omega}_p$, multiply it by the complex conjugate of the unknown variable $\widetilde{d}p_i^*$ and finally compute the expectation of the product

$$\begin{aligned}
\frac{1}{2}\left\langle \left|\widetilde{d}p_i\right|\right\rangle \widehat{p}_i &= \left\langle \widetilde{d}p_i^* \int_{\widetilde{D}_f} f(\mathbf{y})G(\mathbf{y},\widetilde{\mathbf{x}}_i)\,dV\right\rangle \\
&+ \left\langle \widetilde{d}p_i^* \sum_{j=1}^{N_v} \widetilde{p}_j \int_{\partial\widetilde{D}_j} dG(\mathbf{y},\widetilde{\mathbf{x}}_i)\,ds\right\rangle \\
&- \left\langle \widetilde{d}p_i^* \sum_{j=1}^{N_v} \int_{\partial\widetilde{D}_j} \widehat{d}p_j G(\mathbf{y},\widetilde{\mathbf{x}}_i)\,ds\right\rangle \\
&+ \left\langle \widetilde{d}p_i^* \sum_{k=1}^{N_p} \int_{\partial\widetilde{D}_k} \widehat{p}_k dG(\mathbf{y},\widetilde{\mathbf{x}}_i)\,ds\right\rangle \\
&- \left\langle \widetilde{d}p_i^* \sum_{\substack{k=1\\ k\neq i}}^{N_p} \widetilde{d}p_k \int_{\partial\widetilde{D}_k} dG(\mathbf{y},\widetilde{\mathbf{x}}_i)\,ds\right\rangle \\
&+ \left\langle \left|\widetilde{d}p_i\right|^2 \int_{\partial\widetilde{D}_i} dG(\mathbf{y},\widetilde{\mathbf{x}}_i)\,ds\right\rangle.
\end{aligned} \tag{11}$$

Equations (10) and (11) contain high-order statistical moments and a large number of unknowns. Since the problem has much more unknowns than equations, cross-products have to be simplified and some statistical assumptions have to be introduced.

3.2. Assumptions. To reduce the number of unknown cross-products and the amount of supplementary equations needed to solve the problem, we introduce three assumptions based on physical considerations.

The first two assumptions are related to isolated systems and define the dependence between contributions coming from different sources. On the other hand, considering systems which mutually exchange power, a third assumption for nonisolated structures has to be used. This assumption defines the coupling condition between two or more systems and allows to model the power exchange from one to the other.

To introduce the assumptions, we define two kind of sources: power inputs as external loadings or velocity boundary conditions are considered as primary sources; boundary conditions which not describe a power transfer are named secondary sources. The latter are constituted by the multiple wave reflections of the wave stemming from the loadings.

Assumption 1. The contributions of two sources are statistically independent when the positions of the sources or the target points are distinct. The physical reasons behind this assumption are the following: positions of different sources and target points are statistically independent because the two contributions can be supposed independent; each unknown is naturally correlated only to the power inputs and then to loadings and velocity boundary conditions.

Assumption 2. It is considered that a force or a displacement variable expressed at any point of the structure is only correlated with the contribution of the primary sources at that point. This assumption states that Green's function and the related intensity of a secondary source are independent and the average of the product is equal to the product of the averages. It is important to explain the physical meaning of this assumption. Let us consider two frequency-dependent functions A and B. Each of them can be expressed as

$$\begin{aligned} A(\omega) &= \langle A(\omega)\rangle + \epsilon_A(\omega), \\ B(\omega) &= \langle B(\omega)\rangle + \epsilon_B(\omega), \end{aligned} \tag{12}$$

where the average of the fluctuation ϵ is equal to zero. If we compute the expectation of the product, we obtain

$$\langle A(\omega)B(\omega)\rangle = \langle A(\omega)\rangle\langle B(\omega)\rangle + \langle \epsilon_A(\omega)\epsilon_B(\omega)\rangle. \tag{13}$$

The cross-products are suppressed form (13) because they are equal to zero since they are defined as fluctuating functions. We can discuss the physical reasons which cause the vanishing of the second term on the right-hand side. The convergence towards zero depends on their correlation, amplitude, and frequency of oscillations. Let us consider the Green functions $G(x, y_1)$ and $G(x, y_2)$ instead of A and B. When $y_1 \approx y_2$, the difference of amplitude fluctuations are small and the two functions overlap as frequency increases. On the other hand, when $y_1 \neq y_2$, $G(x, y_1)$ and $G(x, y_2)$ are different, independent and rapidly oscillate at medium and high frequencies. If y_1 is far away from y_2, the randomness introduced at y_1 it is not directly correlated to the randomness introduced at y_2. In general, approaching the mid- and high-frequency range the high modal overlap, the high modal density and the low amplitude fluctuations allow to state that the sources are independent.

Assumption 3. The boundaries connecting two substructures, of which one contains a primary source, become primary sources for the other substructure. This assumption allows to model the power flow from one system to the other. Finally, we can state a general rule which can synthesize all of them: unknowns are only dependent on sources which contribute to the power flow within the system.

3.3. Final Formulation. Applying the first two assumptions, the fundamental SBEM equations are obtained. For $\tilde{\mathbf{x}}_i \in \partial\tilde{\Omega}_v$, (10) becomes

$$\begin{aligned} \frac{1}{2}\left\langle |\tilde{p}_i|^2 \right\rangle = {} & \left\langle \tilde{p}_i^* \int_{\tilde{D}_f} f(\mathbf{y}) G(\mathbf{y}, \tilde{\mathbf{x}}_i)\, dV \right\rangle \\ & + \langle \tilde{p}_i^* \rangle \sum_{\substack{j=1 \\ j\neq i}}^{N_v} \left\langle \tilde{p}_j \right\rangle \left\langle \int_{\partial\tilde{D}_j} dG(\mathbf{y}, \tilde{\mathbf{x}}_i)\, ds \right\rangle \\ & - \langle \tilde{p}_i^* \rangle \sum_{j=1}^{N_v} \left\langle \int_{\partial\tilde{D}_j} \hat{d}p_j G(\mathbf{y}, \tilde{\mathbf{x}}_i)\, ds \right\rangle \\ & + \langle \tilde{p}_i^* \rangle \sum_{k=1}^{N_p} \left\langle \int_{\partial\tilde{D}_k} \hat{p}_k dG(\mathbf{y}, \tilde{\mathbf{x}}_i)\, ds \right\rangle \\ & - \langle \tilde{p}_i^* \rangle \sum_{k=1}^{N_p} \left\langle \tilde{d}p_k \right\rangle \left\langle \int_{\partial\tilde{D}_k} G(\mathbf{y}, \tilde{\mathbf{x}}_i)\, ds \right\rangle \\ & + \left\langle |\tilde{p}_i|^2 \right\rangle \left\langle \int_{\partial\tilde{D}_i} dG(\mathbf{y}, \tilde{\mathbf{x}}_i)\, ds \right\rangle. \end{aligned} \tag{14}$$

Applying the assumptions to (11) at point $\tilde{\mathbf{x}}_i \in \partial\tilde{\Omega}_p$, it becomes

$$\begin{aligned} \frac{1}{2}\left\langle \left|\tilde{d}p_i\right| \right\rangle \hat{p}_i = {} & \left\langle \tilde{d}p_i^* \int_{\tilde{D}_f} f(\mathbf{y}) G(\mathbf{y}, \tilde{\mathbf{x}}_i)\, dV \right\rangle \\ & + \left\langle \tilde{d}p_i^* \right\rangle \sum_{j=1}^{N_v} \left\langle \tilde{p}_j \right\rangle \left\langle \int_{\partial\tilde{D}_j} dG(\mathbf{y}, \tilde{\mathbf{x}}_i)\, ds \right\rangle \\ & - \left\langle \tilde{d}p_i^* \right\rangle \sum_{j=1}^{N_v} \left\langle \int_{\partial\tilde{D}_j} \hat{d}p_j G(\mathbf{y}, \tilde{\mathbf{x}}_i)\, ds \right\rangle \\ & + \left\langle \tilde{d}p_i^* \right\rangle \sum_{k=1}^{N_p} \left\langle \int_{\partial\tilde{D}_k} \hat{p}_k dG(\mathbf{y}, \tilde{\mathbf{x}}_i)\, ds \right\rangle \\ & - \left\langle \tilde{d}p_i^* \right\rangle \sum_{\substack{k=1 \\ k\neq i}}^{N_p} \left\langle \tilde{d}p_k \right\rangle \left\langle \int_{\partial\tilde{D}_k} G(\mathbf{y}, \tilde{\mathbf{x}}_i)\, ds \right\rangle \\ & + \left\langle \left|\tilde{d}p_i\right|^2 \right\rangle \left\langle \int_{\partial\tilde{D}_i} dG(\mathbf{y}, \tilde{\mathbf{x}}_i)\, ds \right\rangle. \end{aligned} \tag{15}$$

One can observe that the number of unknowns are equal to $3(N_p + N_v)$. They are as follows.

(i) First order moments (FOM): $\langle \widetilde{p}_i \rangle$ and $\langle \widetilde{d}p_i \rangle$.

(ii) Second order moments (SOM): $\langle |\widetilde{p}_i|^2 \rangle$ and $\langle |\widetilde{d}p_i|^2 \rangle$.

(iii) Correlated unsplittable products of kinematic variables multiplied by primary source: $\langle \widetilde{p}_i^* \int_{\widetilde{D}_f} f(\mathbf{y}) G(\mathbf{y}, \widetilde{\mathbf{x}}_i) dV \rangle$ and $\langle \widetilde{d}p_i^* \int_{\widetilde{D}_f} f(\mathbf{y}) G(\mathbf{y}, \widetilde{\mathbf{x}}_i) dV \rangle$.

To solve the system, other $2(N_p + N_v)$ equations have to be added. $(N_p + N_v)$ equations are obtained by considering the expectation of the classical boundary integral equations (6). Finally, the last $(N_p + N_v)$ equations are obtained by multiplying each side of the conjugate of (6) by the contribution of the external loading. As a result, the problem

$$A\mathbf{p} = \mathbf{b} \tag{16}$$

is solved directly: $\mathbf{p}$ is the unknown vector $3(N_p + N_v) \times 1$, A is a martix $3(N_p + N_v) \times 3(N_p + N_v)$, and $\mathbf{b}$ is a vector $3(N_p + N_v) \times 1$. Due to the equations, matrix A has sparse form and elements are complex.

After the computation of the unknowns, Second-order Moments are evaluated at the field solution point.

Looking at (14) and (15), we can easily understand that the SBEM code is penalized in the low-frequency and small model applications, but it has some advantages over the classical methods when dealing with high frequencies. Even if the number of equation increases, the mesh coarsening process reduces the computational effort. As a rule of thumb, using standard BEM at least 6 element/wavelength are needed in order to obtain a reliable solution. With SBEM things are slightly different. Increasing the frequency, the wavelength reach the size of the small perturbations and uncertainties start to influence the response. This means that the mesh does not need to be refined to reach higher frequency values as happens for BEM but only to reach frequencies at which the uncertainties start playing their role. Moreover, the SBEM gives a statistical result which gives much more details and robustness than a classical deterministic result. As reported in Section 4, using a few elements allows moving up to ranges where standard BEM fails to provide accurate solutions. Moreover, if compared to classic sampling methods for uncertainties modelling it does not require to calculate and average over a population of structures, since the averaging effect is included in the expected terms. Only one run of the program for each frequency step is necessary to obtain an averaged statistical response. Finally, it allows easy coupling with FEM or BEM [30, 31].

It is important to note that boundary conditions play a crucial role as power inputs. Since all the unknowns are dependent on power inputs, a nonzero-velocity boundary condition applied on a large amount of nodes drastically increases the system dimension. Indeed, each node has to be considered as primary source for the system. In this paper we focus our attention only on cases with zero-velocity (or rigid walls) boundary condition.

3.4. Integrals and Integration. In order to solve the SBEM set of equations, the numerical evaluation of the expectations of boundary and domain integrals must be carried out as indicated in (9). The integration path in two- and three-dimensional applications is random, therefore it is not possible to commutate the expectation and the integral operators (as it is possible for rods and beams, one-dimensional elements). To simplify this evaluation, it can be shown that the random variable can be judiciously chosen in order to get rid of the randomness in the integration path by means of a change of a variable [29]. Using a parameter ϵ, the integration path on the right side of (9) does not depend on the random variable anymore. Therefore, it is possible to switch the integration and the expectation operators. In the following cases integrals are solved by means of Gauss quadrature rule: 4 points have been chosen for the surface integration and 3 to 7 points on the uncertain parameter range for the double integration of the probability distribution, depending on the shape of the function and on the required accuracy. The chosen probability distribution has triangular distribution, zero centered, crisp value equal to $1/a$, lower limit $-a$ and upper limit a, and unitary area. Node locations are kept fixed for numerical reasons: this enables easy coupling with FEM velocity for structure models and allows the parametric description of the boundary. This means that the model preserves its shape and only local variability is introduced. The variability in the distance between the field and source points interacts with the wavelength in the high-frequency range and affects the response of the structure.

The introduction of uncertainties in the material, which strongly influences the response of the structure, cannot be taken into account with the current formulation and assumptions. This is mainly due to the fact that the material properties affect all the responses at a nodal location and correlation/decorrelation rules cannot be introduced for them as explained previously.

4. Application Cases

In this section we present two academic application cases: a rectangular and a spheric acoustic cavity. Both of them present zero velocity as a condition over the whole boundary and unit monopole inside the cavity. Source intensity is constant with frequency. Models are studied with three different uncertainty values. The cases have, respectively, characteristic value of the uncertain parameter u equal to 0.02, 0.05, and 0.10 scaled to the characteristic dimension of the element (a value of 1 corresponds to the element dimension). The perturbation is supposed to be constant over the whole boundary and source positions. The fluid is air with density equal to 1.3 kg/m^3 and speed of sound equal to 330 m/s. The solution is evaluated over a field mesh placed in the inner side of the cavity.

The code used is in-house-made and it has been developed in MATLAB.

4.1. Rectangular Acoustic Cavity. This simple application can be useful for instance to model acoustic behaviour of

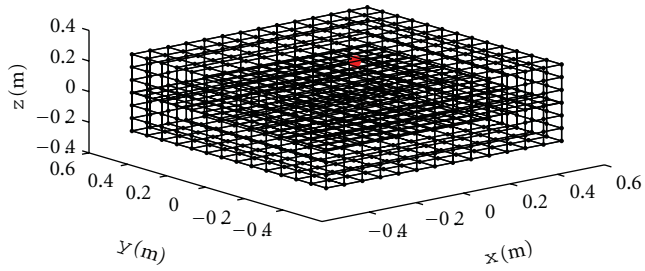

Figure 2: Rectangular acoustic cavity, source and field mesh.

Table 1: Rectangular acoustic cavity: model characteristics and analysis details.

Box dimensions	$1 \times 1 \times 0.5$ m
Elements	650 QUAD
Nodes	652
Position of the acoustic source	(0.2, 0.2, 0.1) m
Characteristic value of the uncertainties, a	0.02–0.05–0.10
Frequency range of analysis	100–3000 Hz
Frequency step	10 Hz

a room in which a loudspeaker excites the fluid generating wave motion. Walls are modelled as rigid since zero velocity boundary condition is applied.

Model characteristics are specified in Table 1 and its geometry in Figure 2.

It can be immediately noted that 650 elements, with 0.077 m as main dimension, are not enough to reach 3000 Hz. Indeed, this model can reach about 700 Hz. To correctly simulate up to such a frequency, we need 0.018 m elements which seriously increase the problem dimension up to around 12 000 degrees of freedom.

The field mesh is composed by 441 points, is planar, and is placed at 0.225 m from the ground. It is rectangular and has the same dimensions of the box. Coordinates of the field solution point are (−0.0990 m, −0.3465 m, 0 m; the box is centered in the origin).

Figure 3 shows the effect of the uncertainties in the evaluation of Green's functions. Functions with different values of uncertainties are compared with the deterministic ones. Increasing the frequency, the effect of uncertainties starts to smooth the response.

From Figures 4, 5, 6, and 7, it is possible to note the effects of the uncertainties on pressure values over the field point mesh. As the value u increases, the response shape becomes smoother. It is worth noting that in Figure 7 there is an irregularity close to the monopole position. This is a shortcoming of the formulation highlighted in [27], indeed approaching to a sources the SBEM may present some inaccuracies because the assumptions proposed in Section 3.2 are valid as far as the location of the secondary and primary sources are distinct.

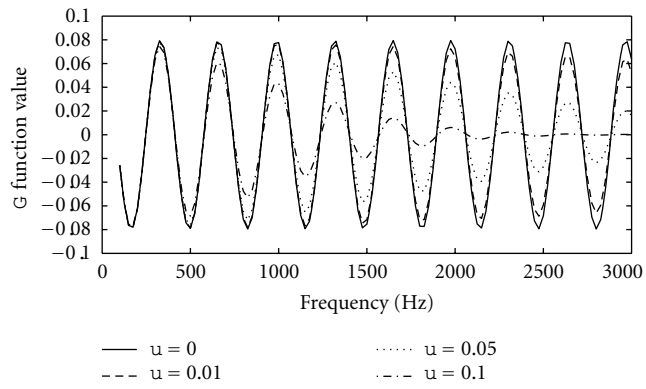

Figure 3: Influence of the uncertainties on Green's functions. Three different values are compared with the deterministic one.

Figures 8, 9, and 10 report the response curve at the receiver point. Standard BEM solution, FOM and SOM, obtained with an SBEM, are plotted with three different value of uncertainty. Some considerations can be done. It is clear that using low values of uncertainty BEM and SBEM provides similar results, indeed the curves are almost superposed. Increasing the uncertainty value FOM and SOM have different behaviours. Increasing the frequency, the former vanishes to zero and the latter becomes smoother and asymptotically converges to the smoothed mean value of the deterministic curve which is the response of the nominal system.

Especially, analyzing Figure 10, it is evident that the SOM curve gives a precise representation of the modal behaviour in the low-frequency range. On the other hand, the high-frequency solution is smooth and only delivers information about the general trend.

4.2. Spherical Acoustic Cavity. Model characteristics are specified in Table 2 and its geometry in Figure 11.

Even is this case the mesh is appropriate to accurately predict the acoustic behaviour up to 800 Hz. Results are similar to the ones obtained in the previous case. From Figures 12, 13, and 14, it can be seen that results surface becomes smoother increasing the uncertain parameter u. As we already noted, with a high level of uncertainty, if the source is placed near the field mesh, it can produce inaccuracies in the results; see Figure 15.

Analyzing the response functions from Figures 16, 17, and 18, it is possible to conclude that SOM give an averaged and smooth trend of the prediction. On the other hand FOM vanishes to zero increasing the frequency.

4.3. Discussion. The first set of results presented the results over a field point mesh. Then frequency response functions have been computed at an interior solution point. Observing them is possible to note as FOMs vanish and SOMs become smooth as the frequency increases. Moreover, in the high-frequency range the only contributions that allow to

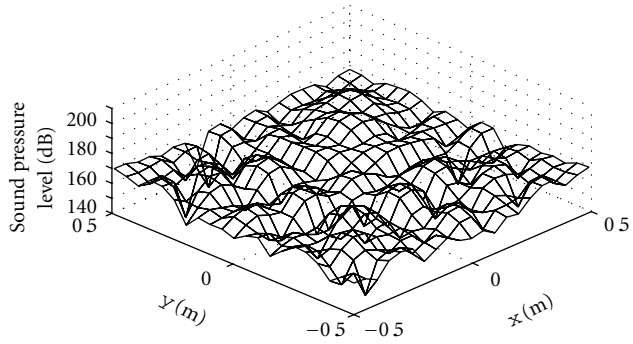

Figure 4: Rectangular acoustic cavity. Second-order moments computed in correspondence of the field point mesh at 1200 Hz. No uncertainties are taken into account.

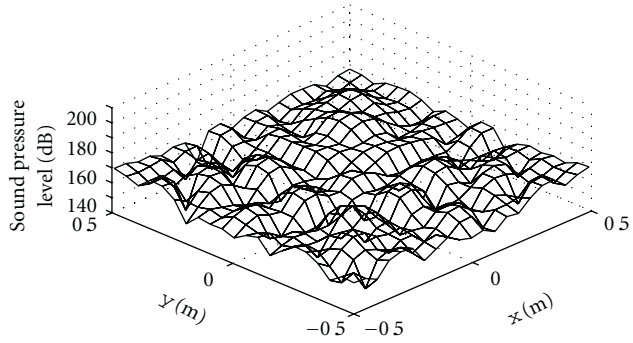

Figure 5: Rectangular acoustic cavity. Second Order Moments computed in correspondence of the field point mesh at 1200 Hz. Uncertainty parameter u is equal to 0.02.

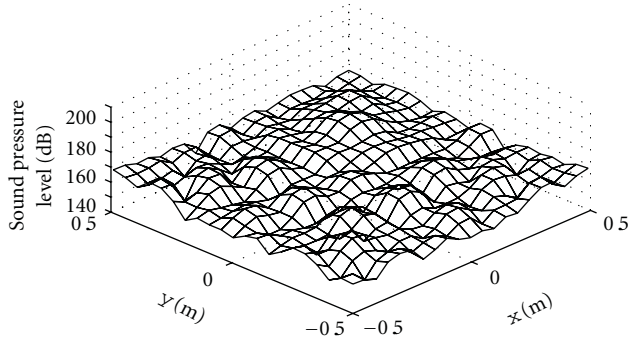

Figure 6: Rectangular acoustic cavity. Second Order Moments computed in correspondence of the field point mesh at 1200 Hz. Uncertainty parameter u is equal to 0.05.

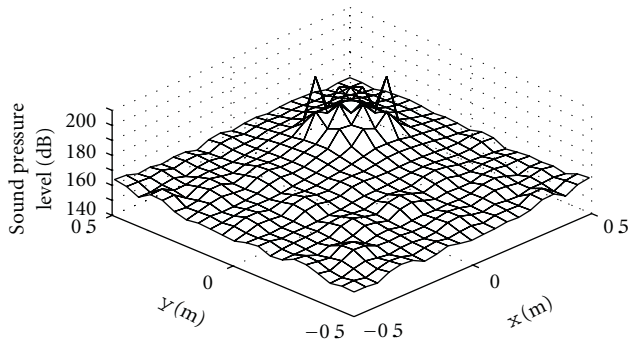

Figure 7: Rectangular acoustic cavity. Second Order Moments computed in correspondence of the field point mesh at 1200 Hz. Uncertainty parameter u is equal to 0.10.

represent the general trend are the ones that introduce power into the system. Consequently, boundary conditions which do not introduce power do not contribute to the solution and vanish.

It is interesting to compare the presented methodology with the other well-known approaches for vibro-acoustics. A reliable technique to predict the averaged response of a system affected by uncertainties is the Monte Carlo method. Nevertheless, in order to obtain a reliable prediction a large amount of computations is needed, and when models are large, obtaining a result would be very demanding. On the contrary, SBEM allows to avoid the sampling procedure and solve the problem in one go.

If compared with the well-known deterministic techniques, SBEM allows to represent a deterministic behaviour in the low-frequency range. Nevertheless, increasing the frequency, uncertainties start to influence the solution and using those techniques becomes meaningless. Instead, SBEM allows to tackle this problem providing a solution which becomes smoother as function of the perturbations. Nevertheless, the computational effort is increased with respect to the methodologies for the low-frequency range.

We can compare the SBEM formulation with the well-known methodology for high frequencies. First of all, pulling down SEA weakens its assumptions and consequently the solution may be no longer reliable. On the contrary pushing up the SBEM to SEA validity range may be very computationally demanding. Moreover, SEA allows to obtain a global response, while SBEM provides local details. Finally, SBEM allows a direct control on the geometrical uncertainty of the model shape while SEA does not.

Regarding the applications shown in the previous paragraph, is worth noting that results obtained with classic BEM are not accurate, since the mesh it is not appropriate for the whole frequency range of analysis. Indeed as we previously observed, using SBEM allows a mesh coarsening process. The following examples are carried out using meshes not refined enough to predict the response over such a wide frequency range. Nevertheless, at high frequencies, a coarse model present matrices with high ill-conditioning number. Since resonance is due to matrix ill-conditioning near the eigenfrequency the behaviour of a model with a very coarse mesh is only mathematically similar to a model with high modal density at high frequencies. This can justify an interest in using coarse meshes at high frequencies in order to validate the SBEM. It is also interesting to highlight the relation between the mesh refinement and the degree of uncertainty. With a very coarse mesh the solution is smoothened and

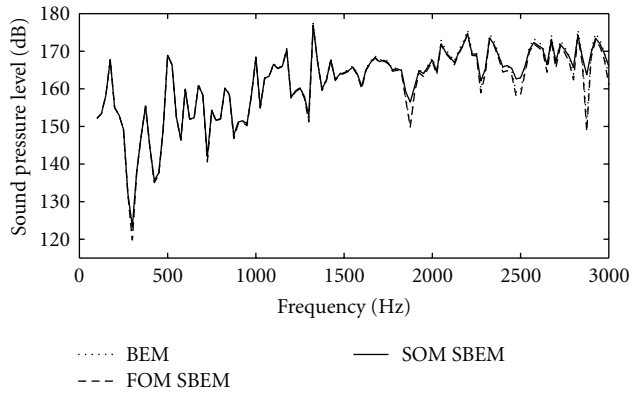

Figure 8: Rectangular acoustic cavity. SPL at the solution point (−0.0990, −0.3465, 0): comparison between standard BEM, First Order Moment (FOM) of SBEM and Second Order Moments (SOM) of SBEM. Uncertainty parameter u is equal to 0.02.

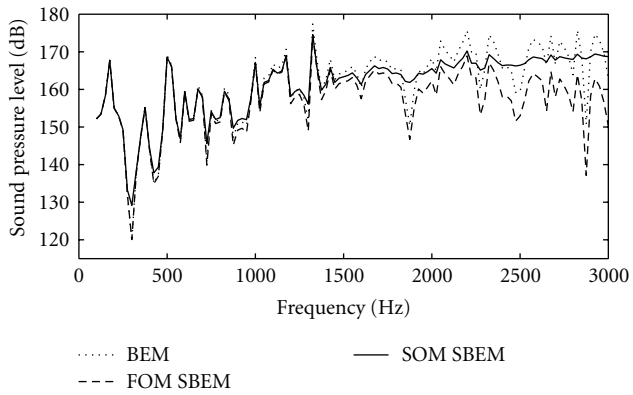

Figure 9: Rectangular acoustic cavity. SPL at the solution point (−0.0990, −0.3465, 0): comparison between standard BEM, First Order Moment (FOM) of SBEM and Second Order Moments (SOM) of SBEM. Uncertainty parameter u is equal to 0.05.

reliable only if the uncertainty degree is high. On the other hand, if perturbations are small, the geometry is almost deterministic and consequently the mesh results inappropriate to predict vibro-acoustic behaviour at high frequencies. A good balance between mesh refinement and degree of uncertainty allows to also reduce the computational effort. Even if the SBEM algorithm has a higher complexity respect to classic BEM, it requires much less elements to predict the smooth trend. Anyhow, matrices are large and complex and handling the problem may be very demanding.

5. Conclusion

Predicting structure behaviour of the whole frequency is one of the most appealing objective in vibro-acoustics. Deterministic methods as FEM and BEM are reliable in the low range, but, decreasing the wavelength, small perturbations play a significant role and their use becomes meaningless.

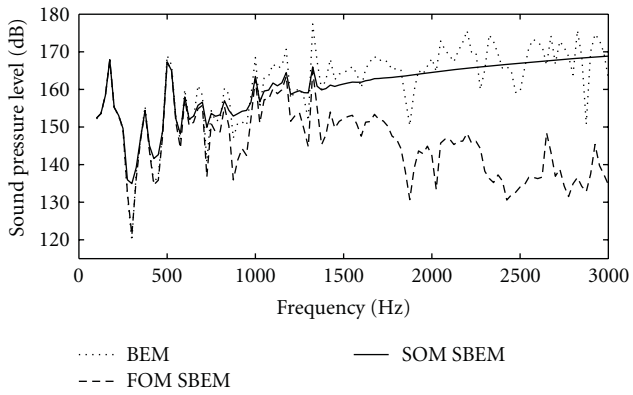

Figure 10: Rectangular acoustic cavity. SPL at the solution point (−0.0990, −0.3465, 0): comparison between standard BEM, First Order Moment (FOM) of SBEM and Second Order Moments (SOM) of SBEM. Uncertainty parameter u is equal to 0.10.

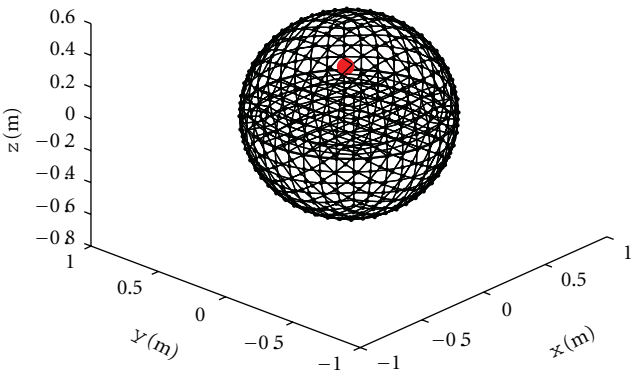

Figure 11: Spherical acoustic cavity, source and field mesh.

Table 2: Spherical acoustic cavity: model characteristics and analysis details.

Radius of the sphere	0.6 m
Elements	600 QUAD
Nodes	602
Position of the acoustic source	(0.3, 0.3, 0.1) m
Characteristic value of the uncertainties, a	0.02–0.05–0.10
Frequency range of analysis	100–3000 Hz
Frequency step	10 Hz

The formulations presented in this paper deal with an enhanced BEM approach, the so-called stochastic BEM. Uncertainties are applied to the geometrical properties of the models under proper assumptions. As a result, increasing the frequency of analysis, the prediction becomes smoother and tends to asymptotically converge to the smoothed mean value of the nominal deterministic curve.

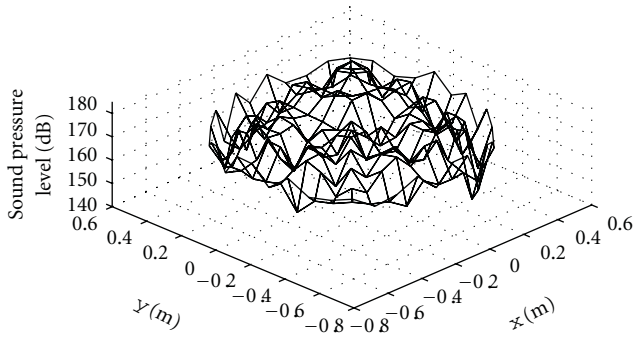

Figure 12: Acoustic spherical cavity. Second-order moments computed in correspondence of the field point mesh at 1200 Hz. No uncertainties are taken into account.

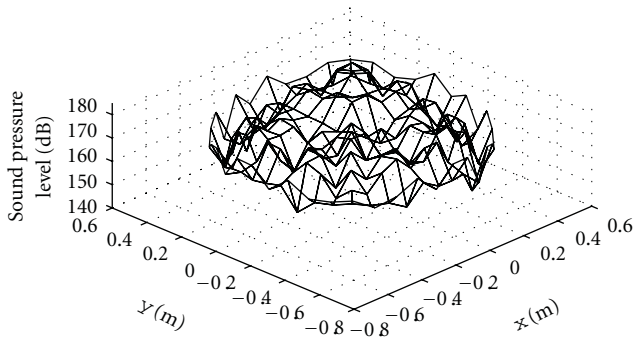

Figure 13: Acoustic spherical cavity. Second-order moments computed in correspondence of the field point mesh at 1200 Hz. Uncertainty parameter u is equal to 0.02.

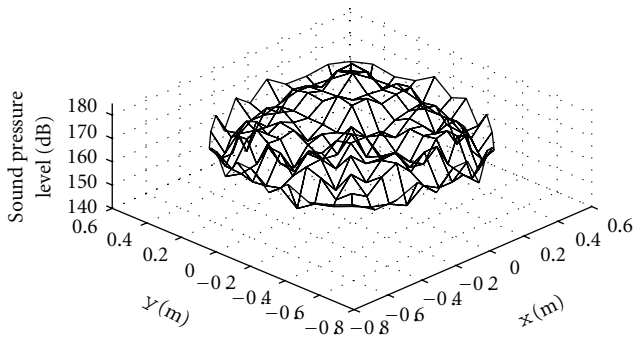

Figure 14: Acoustic spherical cavity. Second-order moments computed in correspondence of the field point mesh at 1200 Hz. Uncertainty parameter u is equal to 0.05.

SBEM has been applied to two three-dimensional academic cases: a rectangular and a spherical acoustic cavity with zero-velocity boundary condition and a unit source inside. For both of them, the response functions has been studied. Low-frequency behaviour is accurately described and, increasing the frequency, the effects of uncertainties smooth the response and the prediction asymptotically tends

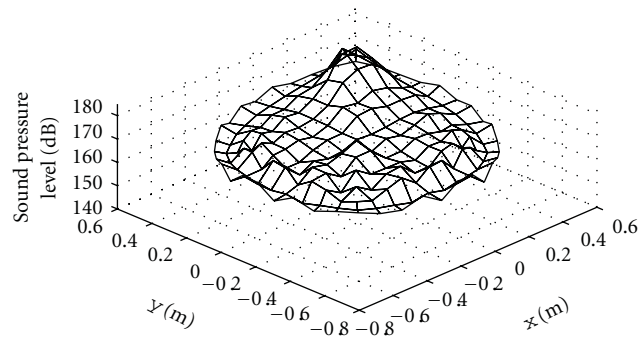

Figure 15: Acoustic spherical cavity. Second-order moments computed in correspondence of the field point mesh at 1200 Hz. Uncertainty parameter u is equal to 0.10.

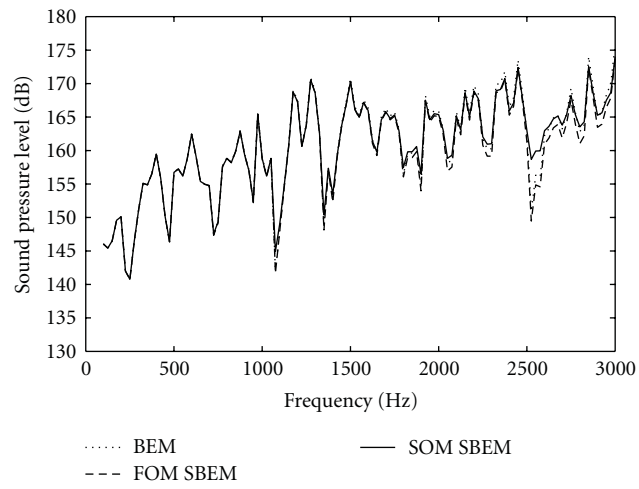

Figure 16: Acoustic spherical cavity. SPL at the solution point (−0.2894, 0.3726, 0): comparison between standard BEM, First Order Moment (FOM) of SBEM and Second-order moments (SOM) of SBEM. Uncertainty parameter u is equal to 0.02.

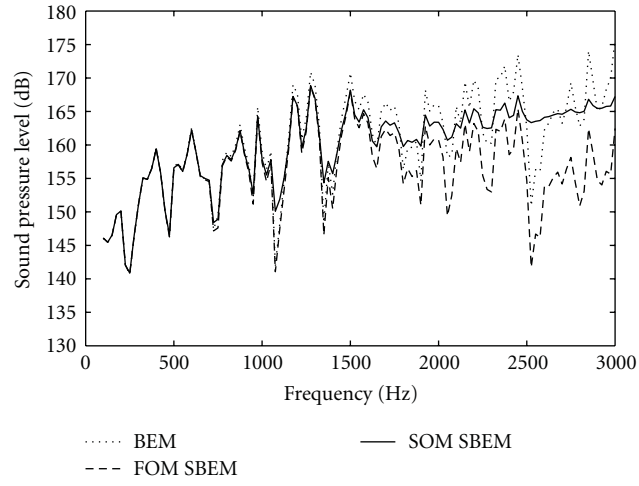

Figure 17: Acoustic spherical cavity. SPL at the solution point (−0.2894, 0.3726, 0): comparison between standard BEM, First Order Moment (FOM) of SBEM and Second-order moments (SOM) of SBEM. Uncertainty parameter u is equal to 0.05.

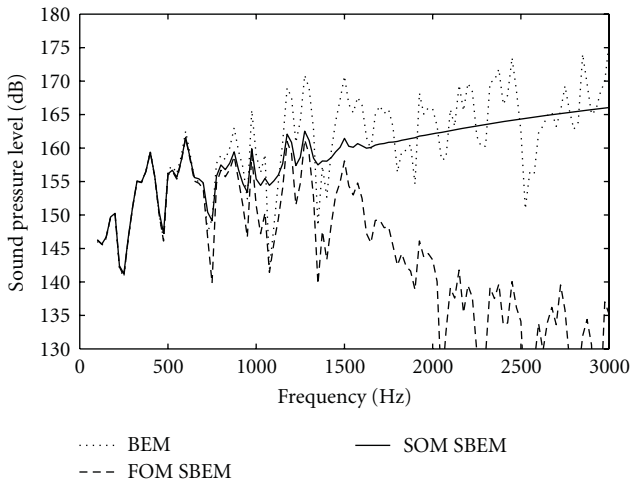

Figure 18: Acoustic spherical cavity. SPL at the solution point (−0.2894, 0.3726, 0): comparison between standard BEM, First Order Moment (FOM) of SBEM and Second-order moments (SOM) of SBEM. Uncertainty parameter u is equal to 0.10.

to the deterministic one. From a computational point of view the effort is decreased in respect to the traditional BEM, thanks to the mesh coarsening process. On the other hand, the number of equations required drastically increases.

Nevertheless, some questions are still open. No rule of thumb exists to correlate the prediction accuracy to the mesh refinement. Moreover, applying a nonzero-velocity boundary condition drastically increases system dimensions because power sources are always connected to the other variables. Research has to be done also in this direction. A computationally less demanding method has to be investigated in order to find a solution to the nonzero problem with reasonable efforts. Finally, up till now, only interior problems have been solved: one of the next step in research is to apply the methodology to exterior cases.

Acknowledgment

This paper has been cofunded by the European Commission within the MID-MOD project under the 7th Framework Programme (GA-2009-218508).

References

[1] O. C. Zienkiewicz and R. L. Taylor, *The Finite Element Method*, vol. 1, 2, McGraw–Hill, London, UK, 4th edition, 1991.

[2] R. Butterfield and K. Bannerjee, *Boundary Element Methods in Engineering Science*, McGraw–Hill, New York, NY, USA, 1991.

[3] R. D. Ciskowski and C. A. Brebbia, *Boundary Element Methods in Acoustics*, WIT Press, Southampton, UK, 1991.

[4] R. Hallez and K. De Langhe, "Solving large industrial acoustic models with the Fast Multipole Method," in *Proceedings of the International Congress on Sound and Vibration (ICSV '09)*, Krakow, Poland, July 2009.

[5] H. Briot, M. Tournour, and G. Massa, "On a few recent advances offinite element methods for the Helmholtz equation," in *Proceedings of the 16th International Congress on Sound and Vibration (ICSV '09)*, Krakow, Poland, July 2009.

[6] W. Desmet, *A wave based prediction technique for coupled vibro-acoustic analysis*, Ph.D. thesis, KU Leuven, Division PMA, Leuven, Belgium, 1998.

[7] C. S. Manohar and A. J. Keane, *Statistics of Energy Flows in Spring-Coupled One-Dimensional Systems*, MIT Press, Cambridge, UK, 1997.

[8] A. J. Keane and C. S. Manohar, "Energy flow variability in a pair of coupled stochastic rods," *Journal of Sound and Vibration*, vol. 168, no. 2, pp. 253–284, 1993.

[9] F. J. Fahy and A. D. Mohammed, "A study of uncertainty in applications of sea to coupled beam and plate systems, part I: computational experiments," *Journal of Sound and Vibration*, vol. 158, no. 1, pp. 45–67, 1992.

[10] N. Baldanzini, "Progettazione meccanica per la riduzione del rumore e delle vibrazioni: lo strumento della Statistical Energy Anlysis," in *Proceedings of the 30th Convegno Nazionale Associazione Italiana Analisi delle Sollecitazioni (AIAS '01)*, Alghero, Italy, Settembre 2001.

[11] R. H. Lyon, *Statistical Energy Analysis of Dynamical Systems*, MIT Press, Cambridge, Mass, USA, 1975.

[12] R. J. M. Craik, *Sound Transmission through Buildings Using Statistical Energy Analysis*, Gower, London, UK, 1996.

[13] K. De Langhe, *High-frequency vibrations: contribuitons to experimental and computational SEA parameter identification techniques*, Ph.D. thesis, KU Leuven, Division PMA, Leuven, Belgium, 1996.

[14] G. Borello and L. Gagliardini., "Virtual SEA: towards an industrial process," in *Proceedings of the SAE Noise and Vibration Conference*, St. Charles, Ill, USA, 2007.

[15] B. R. Mace and E. Manconi, "Modelling wave propagation in two-dimensional structures using finite element analysis," *Journal of Sound and Vibration*, vol. 318, no. 4-5, pp. 884–902, 2008.

[16] S. Finnveden and M. Fraggstedt, "Waveguide finite elements for curved structures," *Journal of Sound and Vibration*, vol. 312, no. 4-5, pp. 644–671, 2008.

[17] P. J. Shorter and R. S. Langley, "Vibro-acoustic analysis of complex systems," *Journal of Sound and Vibration*, vol. 288, no. 3, pp. 669–699, 2005.

[18] P. Ragnarsson, B. Pluymers, S. Donders, and W. Desmet, "Subcomponent modelling of input parameters for statistical energy analysis by using a wave-based boundary condition," *Journal of Sound and Vibration*, vol. 329, no. 1, pp. 96–108, 2010.

[19] D. J. Nefske and S. H. Sung, "Power flow finite element analysis of dynamic systems: basic theory and application to beams," in *Proceedings of the Statistical Energy Analysis*, vol. 3, pp. 47–54.

[20] J. C. Wohlever and R. J. Bernhard, "Mechanical energy flow models of rods and beams," *Journal of Sound and Vibration*, vol. 153, no. 1, pp. 1–19, 1992.

[21] O. M. Bouthier and R. J. Bernhard, "Simple models of energy flow in vibrating membranes," *Journal of Sound and Vibration*, vol. 182, no. 1, pp. 129–147, 1995.

[22] O. M. Bouthier and R. J. Bernhard, "Simple models of energy flow in vibrating plates," *Journal of Sound and Vibration*, vol. 182, no. 1, pp. 149–166, 1995.

[23] Y. Lase, M. N. Ichchou, and L. Jezequel, "Energy flow analysis of bars and beams: theoretical formulations," *Journal of Sound and Vibration*, vol. 192, no. 1, pp. 281–305, 1996.

[24] M. N. Ichchou, A. Le Bot, and L. Jezequel, "Energy models of one-dimensional, multi-propagative systems," *Journal of Sound and Vibration*, vol. 201, no. 5, pp. 535–554, 1997.

[25] M. Viktorovitch, P. Moron, F. Trouverez, and L. Jézéquel, "A stochastic approach of the energy analysis for one-dimensional structures," *Journal of Sound and Vibration*, vol. 216, no. 3, pp. 361–377, 1998.

[26] M. Viktorovitch, F. Thouverez, and L. Jezequel, "A stochastic reformulation of the power flow equations for membranes and plates," *Journal of Sound and Vibration*, vol. 211, no. 5, pp. 910–917, 1998.

[27] M. Viktorovitch, F. Thouverez, and L. Jezequel, "A new random boundary element formulation applied to high frequency phenomena," *Journal of Sound and Vibration*, vol. 223, no. 2, pp. 273–296, 1999.

[28] M. Viktorovitch, F. Thouverez, and L. Jezequel, "An integral formulation with random parameters adapted to the study of the vibrational behaviour of structures in the middle- and high-frequency field," *Journal of Sound and Vibration*, vol. 247, no. 3, pp. 431–452, 2001.

[29] A. Pratellesi, *Noise and vibration analysis in the mid frequency range*, Ph.D. thesis, Università degli Studi di Firenze, Firenze, Italy, 2007.

[30] A. Pratellesi, M. Viktorovitch, N. Baldanzini, and M. Pierini, "A hybrid formulation for mid-frequency analysis of assembled structures," *Journal of Sound and Vibration*, vol. 309, no. 3–5, pp. 545–568, 2008.

[31] M. Viktorovitch and A. Pratellesi, "A hybrid mid-frequency formulation for vibro-acoustic predictions," *Noise Control Engineering Journal*, vol. 56, no. 1, pp. 71–84, 2008.

Hindawi Publishing Corporation
Advances in Acoustics and Vibration
Volume 2011, Article ID 926271, 10 pages
doi:10.1155/2011/926271

Research Article

Highly Accurate Solution of Limit Cycle Oscillation of an Airfoil in Subsonic Flow

Y. P. Zhang,[1] Y. M. Chen,[2] J. K. Liu,[2] and G. Meng[3]

[1] *Nari Technology Development Limited Company, 20 High-Tech Road, Nanjing 210061, China*
[2] *Department of Mechanics, Sun Yat-sen University, 135 Xingang Road, Guangzhou 510275, China*
[3] *State Key Laboratory of Mechanical System and Vibration, Shanghai Jiao Tong University, 800 Dongchuan Road, Shanghai 200240, China*

Correspondence should be addressed to J. K. Liu, jikeliu@hotmail.com

Received 22 September 2010; Accepted 20 April 2011

Academic Editor: Kok Keong Choong

The homotopy analysis method (HAM) is employed to propose a highly accurate technique for solving strongly nonlinear aeroelastic systems of airfoils in subsonic flow. The frequencies and amplitudes of limit cycle oscillations (LCOs) arising in the considered systems are expanded as series of an embedding parameter. A series of algebraic equations are then derived, which determine the coefficients of the series. Importantly, all these equations are linear except the first one. Using some routine procedures to deduce these equations, an obstacle would arise in expanding some fractional functions as series in the embedding parameter. To this end, an approach is proposed for the expansion of fractional function. This provides us with a simple yet efficient iteration scheme to seek very-high-order approximations. Numerical examples show that the HAM solutions are obtained very precisely. At the same time, the CPU time needed can be significantly reduced by using the presented approach rather than by the usual procedure in expanding fractional functions.

1. Introduction

Predicting amplitude and frequency of flutter oscillations of an airfoil via analytical and/or semianalytical techniques has been an active area of research for many years. The describing function technique [1], sometimes referred to as the harmonic balance (HB) or as linearization method, is a widely used method for obtaining an equivalent linear system such that traditional linear aeroelastic methods of analysis can then be employed [2, 3]. According to the number of considered harmonics, the HB method is called HB1 method when only the first harmonic is included, otherwise as the high-dimensional HB method. Lee et al. [4] studied the aeroelastic system by considering two dominant harmonics and by an improved HB1 method, respectively. Recently, the high-dimensional HB method was further improved to investigate the aeroelastic motions of an airfoil [5, 6]. Essentially, the incremental harmonic balance (IHB) method is a semianalytical method for nonlinear dynamic systems. It was used by Shahrzad and Mahzoon [7] and Cai et al. [8], respectively, to predict the amplitudes and frequencies of the LCOs of an airfoil in steady impressible flow. Recently, Chung et al. proposed a new incremental method and applied it to solve aeroelastic problems with freeplay [9] and hysteresis [10] structural nonlinearities, respectively. In addition, the center manifold theory, originally developed to qualitatively analyze nonlinear vibrations, was employed to obtain the approximations of airfoil LCOs [11, 12].

The approximations obtained by HB1 method are relatively accurate for low wind speeds. However, the errors become larger and larger as the speed increases. In some nonlinear flutter cases, the HB1 method may cease to be valid. In principle, the high-dimensional HB method and the IHB method can give approximate solutions with any desired accuracy as long as enough harmonics are taken into account. Unfortunately, however, it becomes more and more difficult to implement either one of them when the number of considered harmonics increases. Likewise, using the center manifold theory can provide us with satisfactory approximations for the LCOs only in a small range of

bifurcation values. When far away from the bifurcation points, results loose accuracy significantly or even become completely incorrect [13]. Thus, it is necessary to develop new easier-to-use methods which can guarantee accuracy for high flow speeds and in more flutter cases, for example, weakly and strongly nonlinear systems.

Over the past decades, Liao developed the homotopy analysis method (HAM), which does not require small parameters and thus can be applied to solve nonlinear problems without small or large parameters [14–16]. The main procedure is to construct a class of deformation equations in a quite general form by introducing an auxiliary parameter. Through these equations, nonlinear problems can be transformed into a series of linear subproblems, which can be solved much more easily step by step. Recently, the HAM has been used in various nonlinear problems [17–21].

In this study, the HAM is employed to propose an efficient and highly accurate approach for nonlinear aeroelastic motions of an airfoil. A major obstacle is met when deducing the high-order deformation equations, because the Taylor expansion of fractal functions is rather cumbersome. An approach is proposed to deal with this problem. This simple yet efficient method ensures an excellent efficiency of the HAM; hence, highly accurate solutions can be easily obtained for both weakly and strongly nonlinear aeroelastic systems.

2. Equations of Motions

The physical model shown in Figure 1 is a two-dimensional airfoil, oscillating in pitch and plunge, which has been employed by many authors. The pitch angle about the elastic axis is denoted by α, positive with the nose up; the plunge deflection is denoted by $\bar{h}$, positive in the downward direction. The elastic axis is located at a distance $a_h b$ from the midchord, while the mass center is located at a distance $x_\alpha b$ from the elastic axis. Both distances are positive when measured towards the trailing edge of the airfoil.

For cubic restoring forces with subsonic aerodynamics, the coupled equations for the airfoil in nondimensional form can be written as follows:

$$\begin{aligned}
&\ddot{\xi} + x_\alpha \ddot{\alpha} + 2\zeta_\xi \frac{\overline{\omega}}{U^*}\dot{\xi} + \left[\frac{\overline{\omega}}{U^*}\right]^2 \xi = -\frac{1}{\pi\mu} C_L(t) + \frac{P(t)b}{mU^2},\\
&\frac{x_\alpha}{r_\alpha^2}\ddot{\xi} + \ddot{\alpha} + 2\zeta_\alpha \frac{1}{U^*}\dot{\alpha} + \left[\frac{1}{U^*}\right]^2 (\alpha + \eta\alpha^3)\\
&\quad = \frac{2}{\pi\mu r_\alpha^2} C_M(t) + \frac{Q(t)}{mU^2 r_\alpha^2},
\end{aligned} \tag{1}$$

where the superscript denotes the differentiation with respect to the nondimensional time t, defined as $t = Ut_1/b$, and t_1 is the real time. $\xi = \bar{h}/b$ is the nondimensional plunge displacement; η is the coefficient of cubic pitching stiffness; $U^* \longleftarrow$ is a nondimensional flow velocity defined as $U^* = U/(b\omega_\alpha)$, and $\overline{\omega}$ is given by $\overline{\omega} = \omega_\xi/\omega_\alpha$, where ω_ξ and ω_α are the natural frequencies of the uncoupled plunging and pitching modes, respectively; ζ_ξ and ζ_α ψ are the damping ratios; r_α is the radius of gyration about the elastic axis. $P(t)$ and $Q(t)$ are the externally applied force and moment,

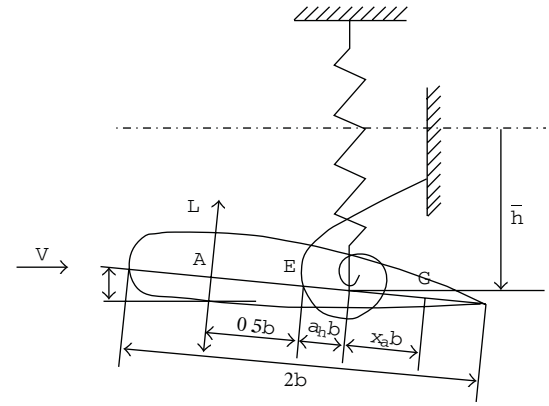

Figure 1: Sketch of a two-dimensional airfoil.

m is the airfoil mass per unit length and μ ψ is the airfoil-air mass ratio. $C_L(t)$ and $C_M(t)$ are the lift and pitching moment coefficients, respectively. For an incompressible flow, the expressions for $C_L(t)$ and $C_M(t)$ are given by

$$\begin{aligned}
C_L(t) &= \pi\left(\ddot{\xi} - a_h \ddot{\alpha} + \dot{\alpha}\right)\\
&\quad + 2\pi\left[\alpha(0) + \dot{\xi}(0) + \left(\frac{1}{2} - a_h\right)\dot{\alpha}(0)\right]\phi(\tau)\\
&\quad + 2\pi \int_0^t \phi(t-\sigma)\\
&\quad \times \left[\dot{\alpha}(\sigma) + \ddot{\xi}(\sigma) + \left(\frac{1}{2} - a_h\right)\ddot{\alpha}(\sigma)\right] d\sigma,
\end{aligned} \tag{2}$$

$$\begin{aligned}
C_M(t) &= \pi\left(\frac{1}{2} + a_h\right)\left[\alpha(0) + \dot{\xi}(0) + \left(\frac{1}{2} - a_h\right)\dot{\alpha}(0)\right]\phi(\tau)\\
&\quad + \pi\left(\frac{1}{2} + a_h\right)\int_0^t \phi(t-\sigma)\\
&\quad \times \left[\dot{\alpha}(\sigma) + \ddot{\xi}(\sigma) + \left(\frac{1}{2} - a_h\right)\ddot{\alpha}(\sigma)\right] d\sigma\\
&\quad + \frac{\pi}{2} a_h\left(\ddot{\xi} - a_h \ddot{\alpha}\right) - \left(\frac{1}{2} - a_h\right)\frac{\pi}{2}\dot{\alpha} - \frac{\pi}{16}\ddot{\alpha},
\end{aligned} \tag{3}$$

where the Wagner function $\phi(t)$ is given by Jone's approximation, $\phi(t) = 1 - \psi_1 e^{-\varepsilon_1 t} - \psi_2 e^{-\varepsilon_2 t}$ with the constants as $\psi_1 = 0.165$, $\psi_2 = 0.335$, $\varepsilon_1 = 0.0455$, and $\varepsilon_2 = 0.3$.

Due to the existence of the integral terms in (3), (1) is a system of integrodifferential equations. In practice, the integral and the nonlinear terms make it difficult to analytically study the dynamic behavior of the system. In order to eliminate the integral terms, Lee et al. [4–6] introduced the following four new variables

$$\begin{aligned}
w_1 &= \int_0^t e^{-\varepsilon_1(t-\sigma)}\alpha(\sigma)d\sigma, \qquad w_2 = \int_0^t e^{-\varepsilon_2(t-\sigma)}\alpha(\sigma)d\sigma,\\
w_3 &= \int_0^t e^{-\varepsilon_1(t-\sigma)}\xi(\sigma)d\sigma, \qquad w_4 = \int_0^t e^{-\varepsilon_2(t-\sigma)}\xi(\sigma)d\sigma.
\end{aligned} \tag{4}$$

System (1) can then be rewritten in a general form containing only differential operators as

$$\begin{aligned} &c_0\,\ddot{\xi} + c_1\,\ddot{\alpha} + c_2\dot{\xi} + c_3\dot{\alpha} + c_4\xi + c_5\alpha + c_6 w_1 \\ &\quad + c_7 w_2 + c_8 w_3 + c_9 w_4 + c_{10} G(\xi) = f(t), \\ &d_0\,\ddot{\xi} + d_1\,\ddot{\alpha} + d_2\dot{\xi} + d_3\dot{\alpha} + d_4\xi + d_5\alpha + d_6 w_1 \\ &\quad + d_7 w_2 + d_8 w_3 + d_9 w_4 + d_{10} M(\alpha) = g(t). \end{aligned} \tag{5}$$

The coefficients $c_0, c_1, \ldots, c_{10}$; $d_0, d_1, \ldots, d_{10}$ are given in the appendix, $f(t)$ and $g(t)$ are functions depending on initial conditions, Wagner's function, and the forcing terms. The nonlinear restoring forces, $G(\xi)$ and $M(\alpha)$, are expressed as $G(\xi) = \gamma\xi^3$ and $M(\alpha) = \eta\alpha^3$, respectively, with γ and η as coefficients.

By introducing a variable vector $\mathbf{X} = (x_1, x_2, \ldots, x_8)^{\mathrm{T}}$, where the superscript "T" denotes the transpose of a matrix, with $x_1 = \alpha$, $x_2 = \dot{\alpha}$, $x_3 = \xi$, $x_4 = \dot{\xi}$, $x_5 = w_1$, $x_6 = w_2$, $x_7 = w_3$, and $x_8 = w_4$, the coupled equations given in (5) can be written as a set of eight first-order ordinary differential equations written in vector form

$$\dot{\mathbf{X}} = \mathbf{Y}(\mathbf{X}, t). \tag{6}$$

This approach allows existing methods suitable for the study of ordinary differential equations to be used in the analysis. *For more details of* (5) *and* (6), *please refer to [4–6].*

3. Homotopy Analysis Method

It is assumed that there is no external forces, that is, $Q(t) = P(t) = 0$ in (1). For large values of t when transients are damped out and steady solutions are obtained, we can let $f(t) = g(t) = 0$. Then, (5) can be rewritten in vector form as

$$\mathbf{M}\,\ddot{\mathbf{x}} + \boldsymbol{\mu}\dot{\mathbf{x}} + \mathbf{K}\mathbf{x} + \mathbf{C}\mathbf{W}(\mathbf{x}) + \mathbf{F}(\mathbf{x}) = 0, \tag{7}$$

where $\mathbf{x} = [\xi, \alpha]^{\mathrm{T}}$, $\mathbf{W}(\mathbf{x}) = [\mathrm{W}_1 \quad \mathrm{W}_2 \quad \mathrm{W}_3 \quad \mathrm{W}_4]^{\mathrm{T}}$,

$$\mathbf{M} = \begin{bmatrix} c_0 & c_1 \\ d_0 & d_1 \end{bmatrix}, \qquad \boldsymbol{\mu} = \begin{bmatrix} c_2 & c_3 \\ d_2 & d_3 \end{bmatrix},$$

$$\mathbf{K} = \begin{bmatrix} c_4 + c_{10} & c_5 \\ d_4 & d_5 + d_{10} \end{bmatrix}, \qquad \mathbf{C} = \begin{bmatrix} c_6 & c_7 & c_8 & c_9 \\ d_6 & d_7 & d_8 & d_9 \end{bmatrix}, \tag{8}$$

and $\mathbf{F}(\mathbf{x}) = \begin{bmatrix} 0 & d_{10}\eta\alpha^3 \end{bmatrix}^{\mathrm{T}}$.

Firstly, introduce a new time scale

$$\tau = \omega t, \tag{9}$$

where ω denotes the frequency of the LCO. Then, (7) becomes

$$\omega^2\mathbf{M}\mathbf{x}'' + \omega\boldsymbol{\mu}\mathbf{x}' + \mathbf{K}\mathbf{x} + \mathbf{C}\mathbf{W}(\mathbf{x}, \omega) + \mathbf{F}(\mathbf{x}) = 0, \tag{10}$$

where the superscript denotes the differentiation with respect to τ. Considering that LCOs are independent of initial conditions, one can adopt the following initial conditions:

$$\mathbf{x}(0) = \begin{bmatrix} h & a \end{bmatrix}^{\mathrm{T}}, \qquad \mathbf{x}'(0) = \begin{bmatrix} \beta & 0 \end{bmatrix}^{\mathrm{T}}. \tag{11}$$

The LCOs of system (10), (11) are periodic motions with frequency ω; thus, $\mathbf{x}$ can be expressed in a Fourier series

$$\mathbf{x} = \sum_{k=0}^{\infty} (\mathbf{c}_k \cos k\tau + \mathbf{s}_k \sin k\tau), \tag{12}$$

where $\mathbf{c}_k, \mathbf{s}_k$ are the coefficients in 2×1 vector form.

Let $a_0, h_0, \omega_0, \beta_0$, and $\mathbf{x}_0(\tau)$ denote the initial approximations of a, h, ω, β, and $\mathbf{x}(\tau)$, respectively. Due to solution expression (12) and initial conditions (11), the initial guess of solution can be chosen as

$$\mathbf{x}_0(\tau) = \begin{bmatrix} h_0 \cos\tau + \beta_0 \sin\tau & a_0 \cos\tau \end{bmatrix}^{\mathrm{T}}. \tag{13}$$

The homotopy analysis method is based on such continuous variations, $A(p)$, $H(p)$, $\Omega(p)$, $B(p)$, and $\mathbf{u}(\tau, p)$, that, as the embedding parameter p increases from 0 to 1, $\mathbf{u}(\tau, p)$ varies from the initial guess $\mathbf{x}_0(\tau)$ to the exact solution, so do $A(p)$, $H(p)$, $\Omega(p)$, $B(p)$ from the initial approximations $a_0, h_0, \omega_0, \beta_0$ to a, h, ω, β, respectively.

Based on (12), one may choose the linear auxiliary operator as

$$L[\mathbf{u}(\tau, p)] = \omega_0^2 \left[\frac{\partial^2 \mathbf{u}(\tau, p)}{\partial \tau^2} + \mathbf{u}(\tau, p) \right]. \tag{14}$$

Thus

$$L\left[\begin{pmatrix} \cos\tau \\ \sin\tau \end{pmatrix} \right] = 0. \tag{15}$$

One may define the nonlinear operator according to (10),

$$\begin{aligned} N[\mathbf{u}(\tau, p), \Omega(p)] &= \Omega^2(p)\mathbf{M}\frac{\partial^2 \mathbf{u}(\tau, p)}{\partial \tau^2} + \Omega(p)\boldsymbol{\mu}\frac{\partial \mathbf{u}(\tau, p)}{\partial \tau} \\ &\quad + \mathbf{K}\mathbf{u}(\tau, p) + \mathbf{C}\mathbf{W}(\mathbf{u}(\tau, p), \Omega(p)) \\ &\quad + \mathbf{F}(\mathbf{u}(\tau, p)). \end{aligned} \tag{16}$$

Using the two operators, a family of equations can then be constructed as

$$(1 - p)L[\mathbf{u}(\tau, p) - \mathbf{x}_0(\tau)] = \lambda p N[\mathbf{u}(\tau, p), \Omega(p)] \tag{17}$$

subject to the initial conditions

$$\begin{aligned} \mathbf{u}(0, p) &= \begin{bmatrix} H(p) & A(p) \end{bmatrix}^T, \\ \left.\frac{\partial \mathbf{u}(\tau, p)}{\partial \tau}\right|_{\tau=0} &= \begin{bmatrix} B(p) & 0 \end{bmatrix}^T, \end{aligned} \tag{18}$$

where the auxiliary parameter λ is a nonzero constant. Equations (17) and (18) are called the zeroth-order deformation equation.

When $p = 0$, (17) and (18) have the solution

$$\mathbf{u}(\tau, 0) = \mathbf{x}_0(\tau). \tag{19}$$

When $p = 1$, they are exactly the same as (10) and (11) provided that

$$\begin{aligned} &\mathbf{u}(\tau, 1) = \mathbf{x}(\tau), \qquad A(1) = a, \qquad H(1) = h, \\ &\Omega(1) = \omega, \qquad B(1) = \beta. \end{aligned} \tag{20}$$

Expand $A(p)$, $H(p)$, $\Omega(p)$, $B(p)$, and $\mathbf{u}(\tau, p)$ as the series

$$\begin{aligned} \mathbf{u}(\tau, p) &= \sum_{k=0}^{\infty} \mathbf{u}_k(\tau) p^k, \qquad A(p) = \sum_{k=0}^{\infty} a_k p^k, \\ H(p) &= \sum_{k=0}^{\infty} h_k p^k, \qquad \Omega(p) = \sum_{k=0}^{\infty} \omega_k p^k, \\ B(p) &= \sum_{k=0}^{\infty} \beta_k p^k. \end{aligned} \tag{21}$$

As long as the parameter λ is properly chosen, all of these series are convergent at $p = 1$. Then, the nth-order HAM solutions can be given as

$$\begin{aligned} \mathbf{x}(\tau) &= \sum_{k=0}^{n} \mathbf{u}_k(\tau), \qquad a = \sum_{k=0}^{n} a_k, \qquad h = \sum_{k=0}^{n} h_k, \\ \omega &= \sum_{k=0}^{n} \omega_k, \qquad \beta = \sum_{k=0}^{n} \beta_k. \end{aligned} \tag{22}$$

Substituting (21) into (17) and (18), differentiating (17) and (18) k times, dividing the differentiations by $k!$ and then letting $p = 0$, one can obtain the kth-order ($k \geq 1$) deformation equation

$$L\left[\mathbf{u}_{k+1}(\tau) - \chi_{k-1}\mathbf{u}_k(\tau)\right] = \lambda \mathbf{R}_k(\tau) \tag{23}$$

subject to the initial conditions

$$\mathbf{u}_k(0) = \begin{bmatrix} h_k & a_k \end{bmatrix}^T, \qquad \mathbf{u}_k'(0) = \begin{bmatrix} \beta_k & 0 \end{bmatrix}^T, \tag{24}$$

where

$$\mathbf{R}_k(\tau) = \frac{1}{(k-1)!} \frac{\partial^{k-1} N[\mathbf{u}(\tau, p), \Omega(p)]}{\partial p^{k-1}}\bigg|_{p=0}, \tag{25}$$

$$\chi_k = \begin{cases} 0, & k = 1, \\ 1, & k \geq 2. \end{cases} \tag{26}$$

Due to the rule of solution expression and the linear operator L, the right hand side of (23) should not contain the first harmonics $\sin\tau$ and $\cos\tau$, because they can result in the so-called secular terms as $\tau\cos\tau$ and $\tau\sin\tau$, respectively. To this end, let

$$\begin{aligned} \mathbf{\Gamma}_k^c(a_k, h_k, \omega_k, \beta_k) &= \frac{1}{\pi}\int_0^{2\pi} \mathbf{R}_k(\tau)\cos\tau d\tau = 0, \\ \mathbf{\Gamma}_k^s(a_k, h_k, \omega_k, \beta_k) &= \frac{1}{\pi}\int_0^{2\pi} \mathbf{R}_k(\tau)\sin\tau d\tau = 0. \end{aligned} \tag{27}$$

Solving (27), a_k, h_k, ω_k, and β_k are determined step by step as k increases.

Note that when $k = 0$, $\mathbf{R}_{k+1}(\tau)$ is essentially the right hand side of (10) with $\mathbf{x} = \mathbf{x}_0$, and the integrations in essence correspond to a harmonic balancing procedure. Therefore, (27) is actually the algebraic equation deduced by the HB1 method. It is nonlinear and independent upon λ. The solutions of a_0, h_0, ω_0, and β_0 can be obtained by using the Newton-Raphson method. Importantly, (27) is always linear as $k \geq 1$, which implies it is rather easy to obtain high-order approximations [22].

4. Expansion of Fractional Functions

A key procedure of implementing the HAM is to deduce the high-order deformation equation, that is, to obtain $R_k(\tau)$ in our study. In most literature about the HAM, authors suggest differentiating the zeroth-order deformation equations (i.e., (17) and (18) in this paper) k times, dividing them by $k!$, and then setting $p = 0$. This kind of approach is based on the classical theories of the Taylor series. In our study, however, using this method to expand $\mathbf{CW}(\mathbf{u}(\tau, p), \Omega(p))$ will cost a large amount of computational resources. For example, substitution of $\alpha = \cos\tau$ into $w_1 = \int_0^t e^{-\varepsilon_1(t-\sigma)}\alpha(\sigma)d\sigma$ yields a simple illustration

$$\begin{aligned} \int_0^t e^{-\varepsilon_1(t-\sigma)}\cos(i\omega\sigma)d\sigma &= \frac{\varepsilon_1\cos(i\omega t) + i\omega\sin(i\omega t)}{\varepsilon_1^2 + i^2\omega^2} \\ &\quad - \frac{\varepsilon_1}{\varepsilon_1^2 + i^2\omega^2}e^{-\varepsilon_1 t}. \end{aligned} \tag{28}$$

For large values of t, the second term in (28) approaches to zero and is neglected since only steady solutions (LCOs) are taken into account. Therefore, the integrations $\mathbf{W}(\cos(i\omega t))$ and $\mathbf{W}(\sin(i\omega t))$ can be expressed as follows, respectively:

$$\begin{aligned} \mathbf{W}_1(\cos(i\omega t)) &= \mathbf{W}_3(\cos(i\omega t)) \\ &= \frac{\varepsilon_1\cos(i\omega t) + i\omega\sin(i\omega t)}{\varepsilon_1^2 + i^2\omega^2}, \\ \mathbf{W}_2(\cos(i\omega t)) &= \mathbf{W}_4(\cos(i\omega t)) \\ &= \frac{\varepsilon_2\cos(i\omega t) + i\omega\sin(i\omega t)}{\varepsilon_2^2 + i^2\omega^2}, \\ \mathbf{W}_1(\sin(i\omega t)) &= \mathbf{W}_3(\sin(i\omega t)) \\ &= \frac{-i\omega\cos(i\omega t) + \varepsilon_1\sin(i\omega t)}{\varepsilon_1^2 + i^2\omega^2}, \\ \mathbf{W}_2(\sin(i\omega t)) &= \mathbf{W}_4(\sin(i\omega t)) \\ &= \frac{-i\omega\cos(i\omega t) + \varepsilon_2\sin(i\omega t)}{\varepsilon_2^2 + i^2\omega^2}, \end{aligned} \tag{29}$$

where $\mathbf{W}_j$, $j = 1, 2, 3, 4$ correspond to the jth component of vector $\mathbf{W}$, and $i = 1, 2, \ldots$, Differentiating k times $1/[\varepsilon_1^2 + (\sum_{i=0}^{n}\omega_i p^i)^2]$ with respect to p will result in a complicated term (i.e., $[\varepsilon_1^2 + (\sum_{i=0}^{n}\omega_i p^i)^2]^k$) in the denominator. Thereby,

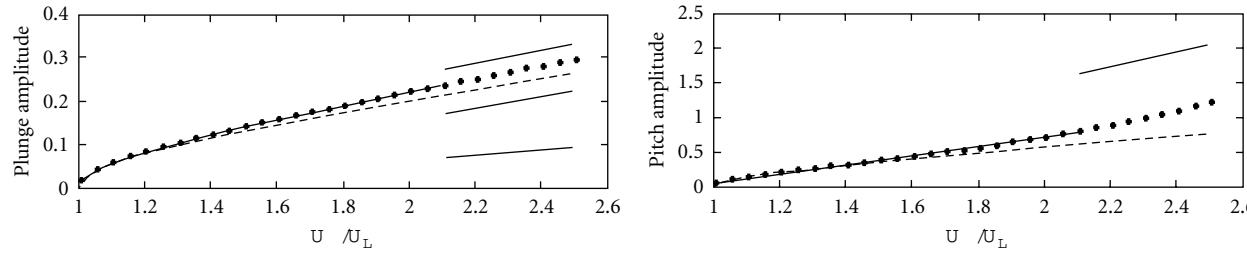

Figure 2: Comparisons of the 50th-order HAM solutions for LCO amplitudes with HB1 results and numerical ones. Dots denote the HAM solutions obtained with $\lambda = -1$, dashed lines represent HB1 results, and real lines denote numerical solutions.

the expression of $\partial^k \mathbf{W}/\partial p^k$ becomes more and more complex as k increases, which makes it quite tough to deduce high-order deformation equations.

We take $1/[\varepsilon_1^2 + (\sum_{i=0}^{n} \omega_i p^i)^2]$ as an illustrative example to propose a means for expanding fractional functions. First of all, denote the denominator as

$$\varepsilon_1^2 + \left(\sum_{i=0}^{n} \omega_i p^i\right)^2 = \varepsilon_1^2 + \omega_0^2 + \sum_{k=1}^{n} \left(\sum_{i=0}^{k} \omega_i \omega_{k-i}\right) p^k := \sum_{k=0}^{n} \sigma_k p^k, \tag{30}$$

where $\sigma_0 = \varepsilon_1^2 + \omega_0^2$ and $\sigma_k = \sum_{i=0}^{k} \omega_i \omega_{k-i}$, $1 \le k \le n$. Taking the nth-order Taylor series of $1/(\sum_{k=0}^{n} \sigma_k p^k)$ as $\sum_{k=0}^{n} \theta_k p^k$, then one has

$$\frac{1}{\sum_{k=0}^{n} \sigma_k p^k} = \sum_{k=0}^{n} \theta_k p^k + O\left(p^{k+1}\right). \tag{31}$$

Rewrite (31) as

$$\begin{aligned} &\left(\sum_{k=0}^{n} \sigma_k p^k\right)\left[\sum_{k=0}^{n} \theta_k p^k + O(p^{n+1})\right] \\ &\quad = \sum_{k=0}^{n} \left(\sum_{i=0}^{k} \sigma_i \theta_{k-i}\right) p^k + O\left(p^{k+1}\right) = 1. \end{aligned} \tag{32}$$

Equating the coefficients of p^k results in

$$\sigma_0 \theta_0 = 1, \qquad \sum_{i=0}^{k} \sigma_i \theta_{k-i} = 0, \quad k = 1, 2, \ldots, n. \tag{33}$$

Interestingly, (33) is always linear. That means it is rather easy to determine θ_k if σ_i are all known, $i = 0, 1, 2, \ldots, k$.

5. Numerical Examples

5.1. Main Results. The system parameters under consideration are $\mu = 100$, $r_\alpha = 0.5$, $a_h = -0.5$, $\zeta_\alpha = \zeta_\xi = 0$, $\overline{\omega} = 0.25$, $x_\alpha = 0.25$, $\gamma = 0$, and $\eta = 80$.

Numerical solutions of (6) can be obtained by the fourth-order Runge-Kutta method. Without special statement, the numerical solutions in this paper are obtained

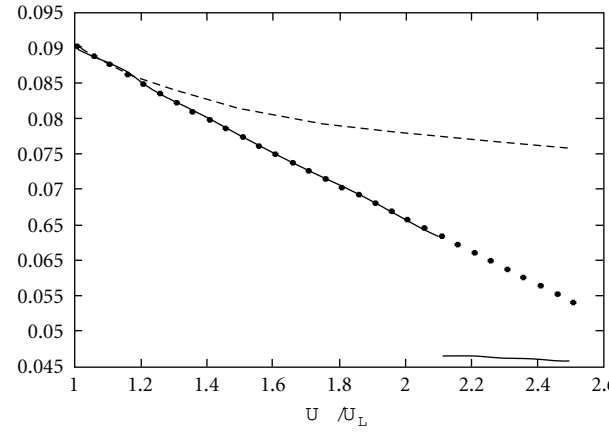

Figure 3: Comparisons of the 50th-order HAM solutions for LCO frequencies with HB1 results and numerical ones. Dots denote the HAM solutions obtained with $\lambda = -1$, dashed lines represent HB1 results, and real lines denote numerical solutions.

subject to the initial conditions as $\alpha(0) = 1^\circ$ and $\dot{\alpha}(0) = \xi(0) = \dot{\xi}(0) = 0$.

Using analytical techniques developed for nonlinear dynamical systems, the linear flutter speed is found at $U^* = U_L^* = 6.0385$ [4, 5]. As U^* increases beyond U_L^*, LCO arises, and thus U_L^* is a Hopf bifurcation point. Note that the flutter boundary U_L^* is independent of the nonlinear coefficient η. Lee et al. [4] found a secondary Hopf bifurcation as U^* increases further, where a jump of the amplitudes is detected (see Figures 2 and 3). Liu et al. [6] used the high- dimensional HB method to study the secondary Hopf bifurcation and found that to capture the secondary bifurcation, as many as 9 (or 5 dominant) harmonics have to be considered.

In the proposed method, the zeroth-order HAM approximation is essentially given by the HB1 method. The higher-order approximations only contribute a higher precision. Thus, it is not capable of detecting the second bifurcation at the present state. Even so, validity and high efficiency of the proposed method can be observed when U^* is in $[U_L^*, 2U_L^*]$ or so. Figures 2 and 3 show the comparisons of the 50th-order HAM solutions with the HB1 and the numerical results. The HAM solutions are almost the same as

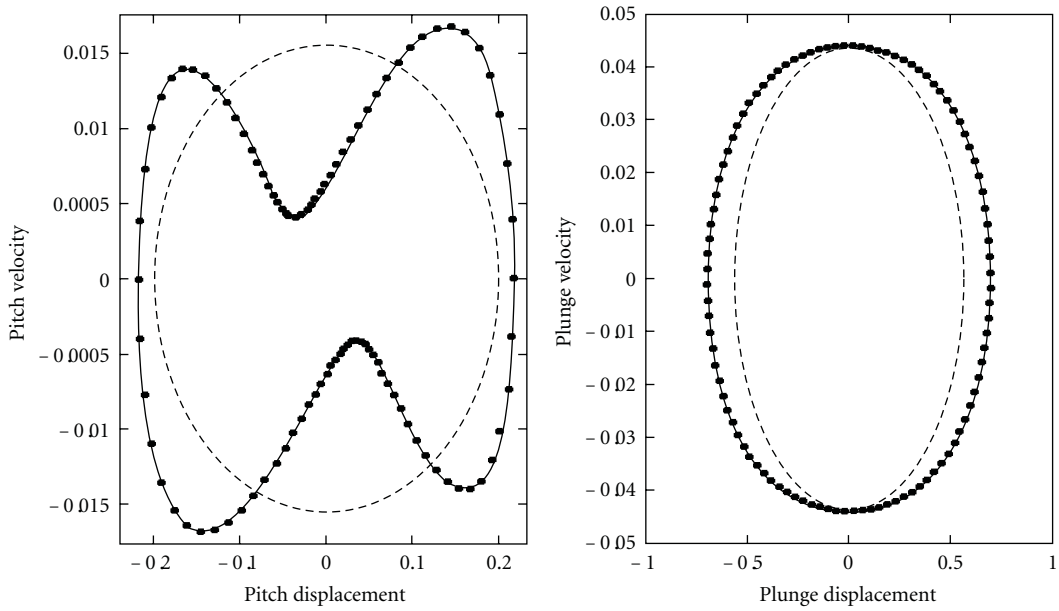

Figure 4: The phase planes of LCOs of system (1) with $U^* = 2U_L^*$. Dots denote the 50th-order HAM solution with $\lambda = -1$, real lines the numerical result, and dashed lines the HB1 one.

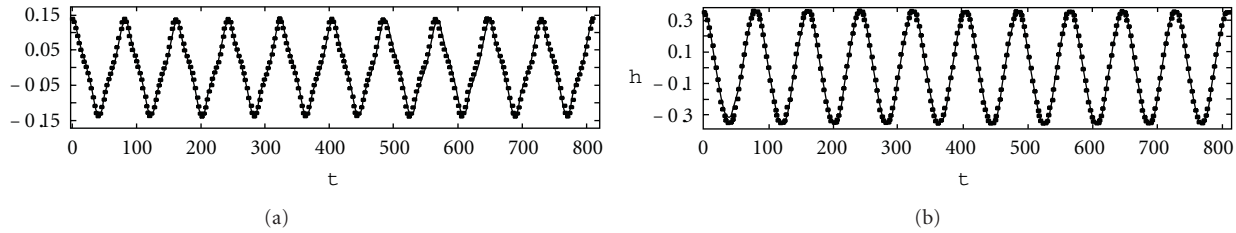

Figure 5: The time history responses of system (1) with $U^* = 1.5U_L^*$. Dots denote the 50th-order HAM solutions with $\lambda = -1$ and real lines the numerical results.

the numerical ones, while the differences of the HB1 results increase rapidly with increasing U^*.

The HAM approximation is based on the first HB method, because the first HAM approximation is the HB1 solution. Since the HB1 method is incapable of tracking the LCOs when U^* is larger than the secondary bifurcation value, about $2U_L^*$, so is the presented approach, as shown in Figures 2 and 3.

Figures 4 and 5 show the phase planes of LCOs and the time history responses of the nonlinear aeroelastic system, respectively. Again, the accuracy of the HAM solution can be demonstrated. Even though the phase plane is very complex, for example, the pitch LCO, the HAM is still capable of tracking it. Note that the numerical solution plotted in Figure 5 is obtained using the fourth-order Runge-Kutta method with initial values given by the HAM solution.

More precisely, the 120th-order HAM solutions shown in Table 1 are compared with the numerical ones. Excellent agreement can also be observed. The higher the order the HAM approximations are obtained to, the more accurate the solution is. For example, the relative difference between the 120th-order HAM solution and the numerical one is less than 0.001%. As shown in Figure 6, the residues of (6) with HAM solutions converge rapidly to 0. The absolute errors of residues with respect to the 40th-order, 80th-order, and 120th-order HAM solutions are at the order of 10^{-8}, 10^{-12}, and 10^{-16}, respectively. Furthermore, as $n > 120$, a_n, h_n, ω_n, and β_n are all small quantities compared with 10^{-16}. Roughly speaking, the 120th-order HAM solution can be considered to be correct to 15 decimal places. Note that it is tough to obtain such a highly accurate solution using some numerical techniques, including the RK method.

Very interestingly, it is found that ω_i is independent of η, while a_i, β_i, and h_i are in inverse proportion to $\sqrt{\eta}$. Thus, the convergence of series (21) is independent of η, and the proposed method can work for both weakly and strongly nonlinear problems. Furthermore, it is proved that the frequency of the LCOs of aeroelastic system (5) is independent of η, while the amplitudes are in inverse proportion to $\sqrt{\eta}$.

Table 1: Comparisons of the amplitudes and frequencies obtained by the HAM ($\lambda = -1$) with numerical solutions.

U^*	$U^* = 1.5U_L^*$			$U^* = 2U_L^*$		
HAM	Frequency	Pitch	Plunge	Frequency	Pitch	Plunge
$N = 40$	0.077563656128	0.13738145786	0.356858	0.0658609	0.2184836	0.6945022
$N = 80$	0.077563606476	0.13738151172	0.35685814	0.0657867	0.2185646	0.6964279
$N = 120$	0.07756360647090	0.13738151173	0.35685815	0.0657833	0.2185685	0.6965209
Numerical	0.0775635	0.1373816	0.3568590	0.0657829	0.2185689	0.6965298

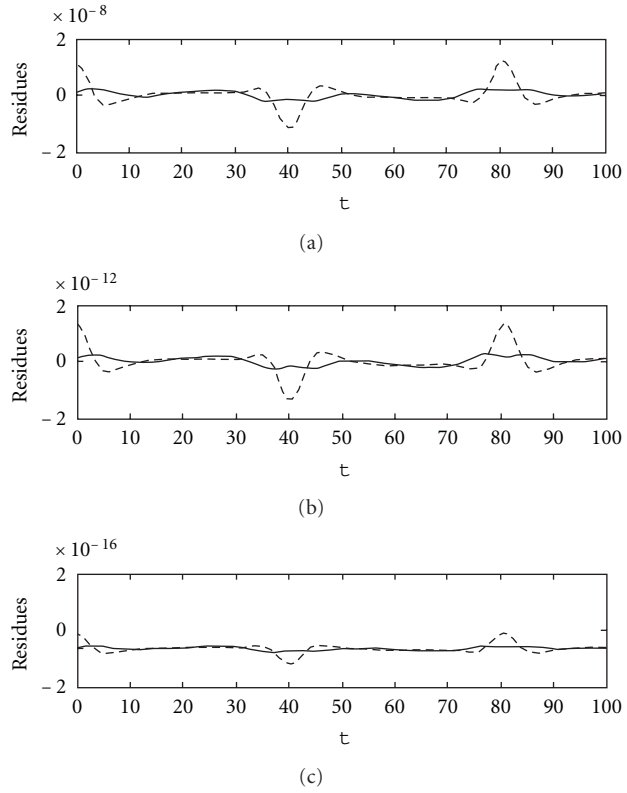

Figure 6: Residues of (6) ($U^* = 1.5U_L^*$) with HAM solutions attained with $\lambda = -1$, (a): $N = 40$; (b): $N = 80$; (c): $N = 120$, where the real and dash lines denote the residues of the first and the second equations, respectively.

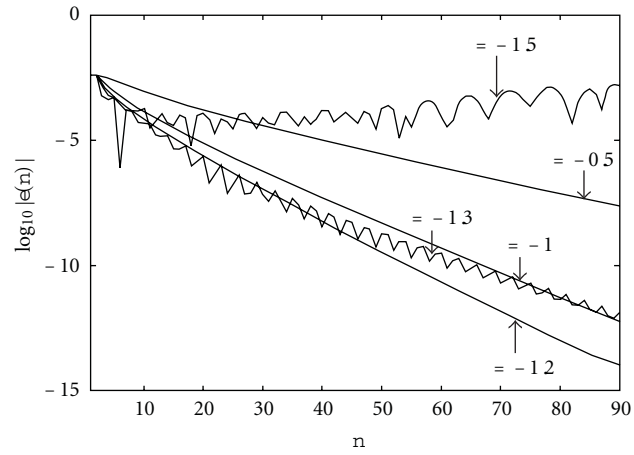

Figure 7: The λ-curves with respect to ω, where $U^* = 1.5U_L^*$.

5.2. Choosing the Auxiliary Parameter. The HAM series are dependent upon the auxiliary parameter λ. For the choice of the value of λ, one should think about two aspects, that is, whether the series converge and the convergent rate. Liao [16] suggested a technique via plotting the curves of the attained HAM solutions versus different values of λ, namely, the λ-curves. From Table 1, one can assume the angular frequency of system (1) with $U^* = 1.5U_L^*$ as $\varpi = 0.07756360647090$. Denote the discrepancy between the nth-order HAM frequency solution and ϖ as $e(n) = (\sum_{k=0}^{n} \omega_k) - \varpi$. Figure 7 shows the λ-curves with respect to ω. Considering that the longitudinal coordinate refers to the logarithm of $|e(n)|$, one knows the HAM solutions attained with $\lambda = -0.5$, $\lambda = -1$, $\lambda = -1.2$, and $\lambda = -1.3$ all approach to ϖ, while the one with $\lambda = -1.5$ does not. As λ decreases from -0.5 to -1 and further to -1.2, the convergent rate of the HAM solution increases. However, as $\lambda = -1.2$ decreases even a little, the convergent rate decreases ($\lambda = -1.3$). It can even lead to the misconvergence of the HAM series ($\lambda = -1.5$). Therefore, on one hand one would expect to choose λ small enough to accelerate the convergence of the HAM series. On the other hand, it is prone to choose an improper one. In this study, $\lambda = -1$ is a good choice.

5.3. Homotopy-Padé Technique. In order to achieve faster convergence of HAM series, currently, researchers introduced some optimal approaches and developed the optimal approaches [23, 24]. Also, the homotopy-Padé technique was proposed to accelerate the convergence of HAM series, [25]. In order to obtain the [m, n] Pade approximation of the HAM series, one should first compute all (m+n)th-order HAM approximations. Therefore, the [m, n] Pade approximations for the frequency and the pitch amplitudes are compared with their corresponding (m+n)th-order HAM solutions, respectively, as shown in Tables 2 and 3. Table 2 shows that the Pade approximations are more accurate than the corresponding HAM solutions, especially when m and n are relatively large. That implies the homotopy-Padé technique can really accelerate the convergence of the HAM series. As Table 3 shows, when $U^* = 2U_L^*$ and $\lambda = -2$, the HAM series are disconvergent at $p = 1$. While the HAM-Pade approximations can still approach to the highly accurate solution. In such a case, the convergent region of the HAM series is enlarged by the homotopy-Padé technique.

Table 2: Comparisons of the amplitudes and frequencies given by the HAM Pade approximations ($\lambda = -1$) with the numerical solutions, where $U^* = 1.5U_L^*$.

$[m, n]$ HAM Pade	Frequency	Relative error (%)	Pitch	Relative error (%)
[5, 5]	0.07765100977663	0.11	0.13745051052294	0.05
HAM 10	0.07770384628505	0.18	0.13726535168074	−0.08
[7, 8]	0.07756746357388	$5e-3$	0.13737312674052	$-6e-3$
15	0.07759388593952	$4e-2$	0.13735291378024	$-2e-2$
[10, 10]	0.07756394500764	$4e-4$	0.13738142730826	$-6e-5$
HAM 20	0.07757112740482	$1e-2$	0.13737399877222	$-5e-3$
HAM $N = 120$	0.07756360647090		0.13738151173287	

Table 3: Comparisons of the amplitudes and frequencies given by the HAM Pade approximations ($\lambda = -2$) with the numerical solutions, where $U^* = 2U_L^*$.

$[m, n]$ HAM Pade	Frequency	Pitch
[5, 5]	0.067011196	0.221689949
HAM 10	0.0730367	0.156371061
[8, 8]	0.06595560	0.21807163
16	0.5207506	3.48085267
[10, 10]	0.0658774	0.21854332
HAM 20	7.63500	−28.477895
HAM $N = 120$,	0.0657829	0.2185689

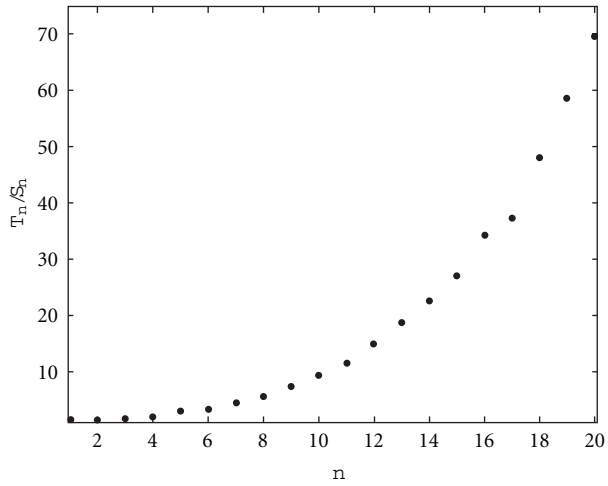

Figure 8: The ratio between the CPU times T_n and S_n, where $\lambda = -1$ and $U^* = 1.5U_L^*$.

5.4. About the CPU Time. Next, we will discuss why it is necessary and worthwhile to employ the approach for series expansion of fractional function, as shown in Section 4. The usually adopted procedure for deducing the higher-order deformation equations is differentiating the zeroth-order deformation equations k times, dividing them by $k!$, and then setting $p = 0$. Denote the CPU time needed in seeking the nth-order HAM approximations by T_n when using the routine procedure, and by S_n when employing the means presented in Section 4. Figure 8 shows the ratio between T_n and S_n versus varying n. When $n > 10$, T_n is more than S_n by one order of magnitude. Moreover, it increases more and more rapidly as n increases. The presented technique can indeed save a large amount of computational effort. Table 4 shows the comparison of the respective CPU time needed in obtaining the nth-order HAM solution, even seeking the 120th-order solution.

6. Conclusions

Based on the HAM, we have proposed an approach for obtaining highly accurate approximations for LCOs of strongly nonlinear aeroelastic systems. An easy-to-use approach is proposed to tackle the difficulty in expanding fractional functions into the Taylor series. With the help of this approach, the HAM approximations can be obtained to a very high order and hence can provide solutions to any desired accuracy. The attained HAM solutions are almost the same as the numerical results. Since it is tough to achieve solutions to such high precision, even via the numerical solutions, thus our approaches can be used to validate other solution methods. Also, numerical examples demonstrate that the presented approaches are valid for both weakly and strongly nonlinear aeroelastic systems. These imply that the presented approaches could be applicable in more nonlinear problems, especially those with fractional functions.

As mentioned above, the first HAM approximation is in essence the HB1 solution. Note also that the HB1 method is incapable of obtaining the LCO solutions, when U^* increases beyond the secondary point, that is, $U^* = 2.1U_L^*$. Therefore, the presented HAM fails in seeking the solution after the secondary point. In order to do so, one could give the initial solution guess (i.e., (11)) with the third harmonics, so that the initial solution can be determined.

Table 4: The CPU time needed in seeking the nth-order HAM approximations, the parameter values are $U^* = 1.5U_L^*$ and $\lambda = -1$.

The nth HAM solution	The CPU time needed (second)	
n	The routine procedure	The presented approach
10	14	2.8
15	58	4.6
20	196	6.8
50	/	46
80	/	239
120	/	1393

In addition, both Figure 8 and Table 4 show that the presented technique can indeed save a large amount of computational effort. The HAM approximations can be obtained to as high as 120th-order within less than half an hour at a microcomputer. As long as the auxiliary parameter is properly chosen, the 100th-order HAM solutions are precise to more than 14 decimals, as implied by Figures 6 and 7, respectively. It is fair to say the presented approach is capable of providing solution to very high precision.

As for the proposed approach for expanding fractional functions, the problem about the robustness of the calculation should be paid special attention in practicing. For example, the coefficient matrix of θ_i's could be illconditioned or singular, which could result in additional numerical error.

Appendix

We have the following Expressions of the Coefficients in (5):

$$c_0 = 1 + \frac{1}{\mu}, \qquad c_1 = x_\alpha - \frac{a_h}{\mu},$$

$$c_2 = \frac{2}{\mu}(1 - \psi_1 - \psi_2) + 2\zeta_\xi \frac{\overline{\omega}}{U^*},$$

$$c_3 = \frac{1}{\mu}(1 + (1 - 2a_h)(1 - \psi_1 - \psi_2)),$$

$$c_4 = \frac{2}{\mu}(\varepsilon_1\psi_1 + \varepsilon_2\psi_2),$$

$$c_5 = \frac{2}{\mu}\left(1 - \psi_1 - \psi_2 + \left(\frac{1}{2} - a_h\right)(\varepsilon_1\psi_1 + \varepsilon_2\psi_2)\right),$$

$$c_6 = \frac{2}{\mu}\varepsilon_1\psi_1\left(1 - \varepsilon_1\left(\frac{1}{2} - a_h\right)\right),$$

$$c_7 = \frac{2}{\mu}\varepsilon_2\psi_2\left(1 - \varepsilon_2\left(\frac{1}{2} - a_h\right)\right),$$

$$c_8 = -\frac{2}{\mu}\varepsilon_1^2\psi_1, \qquad c_9 = -\frac{2}{\mu}\varepsilon_2^2\psi_2, \qquad c_{10} = \left(\frac{\overline{\omega}}{U^*}\right)^2,$$

$$d_0 = \frac{x_\alpha}{r_\alpha^2} - \frac{a_h}{\mu r_\alpha^2}, \qquad d_1 = 1 + \frac{1 + 8a_h^2}{8\mu r_\alpha^2},$$

$$d_2 = -\frac{1 + 2a_h}{\mu r_\alpha^2}(\varepsilon_1\psi_1 + \varepsilon_2\psi_2),$$

$$d_3 = \frac{1 - 2a_h}{2\mu r_\alpha^2} - \frac{\left(1 - 4a_h^2\right)(1 - \psi_1 - \psi_2)}{2\mu r_\alpha^2} + \frac{2\zeta_\alpha}{U^*},$$

$$d_4 = -\frac{1 + 2a_h}{\mu r_\alpha^2}(\varepsilon_1\psi_1 + \varepsilon_2\psi_2),$$

$$d_5 = -\frac{1 + 2a_h}{\mu r_\alpha^2}(1 - \psi_1 - \psi_2) - \frac{(1 + 2a_h)(1 - 2a_h)(\psi_1\varepsilon_1 - \psi_2\varepsilon_2)}{2\mu r_\alpha^2},$$

$$d_6 = -\frac{(1 + 2a_h)\psi_1\varepsilon_1}{\mu r_\alpha^2}\left(1 - \varepsilon_1\left(\frac{1}{2} - a_h\right)\right),$$

$$d_7 = -\frac{(1 + 2a_h)\psi_2\varepsilon_2}{\mu r_\alpha^2}\left(1 - \varepsilon_2\left(\frac{1}{2} - a_h\right)\right),$$

$$d_8 = \frac{(1 + 2a_h)\psi_1\varepsilon_1^2}{\mu r_\alpha^2}, \qquad d_9 = \frac{(1 + 2a_h)\psi_2\varepsilon_2^2}{\mu r_\alpha^2},$$

$$d_{10} = \left(\frac{1}{U^*}\right)^2. \tag{A.1}$$

Acknowledgments

This work is supported by the National Natural Science Foundation of China (10772202, 10102023, 10972241, 11032005), Doctoral Program Foundation of Ministry of Education of China (20090171110042), and Educational Commission of Guangdong Province of China (34310018).

References

[1] B. H. K. Lee, S. J. Price, and Y. S. Wong, "Nonlinear aeroelastic analysis of airfoils: bifurcation and chaos," *Progress in Aerospace Sciences*, vol. 35, no. 3, pp. 205–334, 1999.

[2] J. K. Liu and L. C. Zhao, "Bifurcation analysis of airfoils in incompressible flow," *Journal of Sound and Vibration*, vol. 154, no. 1, pp. 117–124, 1991.

[3] Y. M. Chen and J. K. Liu, "On the limit cycles of aeroelastic systems with quadratic nonlinearities," *Structural Engineering and Mechanics*, vol. 30, no. 1, pp. 67–76, 2008.

[4] B. H. K. Lee, L. Liu, and K. W. Chung, "Airfoil motion in subsonic flow with strong cubic nonlinear restoring forces," *Journal of Sound and Vibration*, vol. 281, no. 3–5, pp. 699–717, 2005.

[5] L. P. Liu and E. H. Dowell, "The secondary bifurcation of an aeroelastic airfoil motion: effect of high harmonics," *Nonlinear Dynamics*, vol. 37, no. 1, pp. 31–49, 2004.

[6] L. Liu, E. H. Dowell, and J. P. Thomas, "A high dimensional harmonic balance approach for an aeroelastic airfoil with cubic restoring forces," *Journal of Fluids and Structures*, vol. 23, no. 3, pp. 351–363, 2005.

[7] P. Shahrzad and M. Mahzoon, "Limit cycle flutter of airfoils in steady and unsteady flows," *Journal of Sound and Vibration*, vol. 256, no. 2, pp. 213–225, 2002.

[8] M. Cai, J. K. Liu, and J. Li, "Incremental harmonic balance method for airfoil flutter with multiple strong nonlinearities," *Applied Mathematics and Mechanics (English Edition)*, vol. 27, no. 7, pp. 953–958, 2006.

[9] K. W. Chung, C. L. Chan, and B. H. K. Lee, "Bifurcation analysis of a two-degree-of-freedom aeroelastic system with freeplay structural nonlinearity by a perturbation-incremental method," *Journal of Sound and Vibration*, vol. 299, no. 3, pp. 520–539, 2007.

[10] K. W. Chung, Y. B. He, and B. H. K. Lee, "Bifurcation analysis of a two-degree-of-freedom aeroelastic system with hysteresis structural nonlinearity by a perturbation-incremental method," *Journal of Sound and Vibration*, vol. 320, no. 1-2, pp. 163–183, 2009.

[11] L. Liu, Y. S. Wong, and B. H. K. Lee, "Application of the centre manifold theory in non-linear aeroelasticity," *Journal of Sound and Vibration*, vol. 234, no. 4, pp. 641–659, 2000.

[12] Q. Ding and D. L. Wang, "The flutter of an airfoil with cubic structural and aerodynamic non-linearities," *Aerospace Science and Technology*, vol. 10, no. 5, pp. 427–434, 2006.

[13] J. Grzedziński, "Limitation of application of the center manifold reduction in aeroelasticity," *Journal of Fluids and Structures*, vol. 21, no. 2, pp. 187–209, 2005.

[14] S. J. Liao, "A kind of approximate solution technique which does not depend upon small parameters-II: an application in fluid mechanics," *International Journal of Non-Linear Mechanics*, vol. 32, no. 5, pp. 815–822, 1997.

[15] S. J. Liao, "On the homotopy analysis method for nonlinear problems," *Applied Mathematics and Computation*, vol. 147, no. 2, pp. 499–513, 2004.

[16] S. J. Liao, *Beyond Perturbation: Introduction to Homotopy Analysis Method*, Chapman & Hall/CRC Press, Boca Raton, Fla, USA, 2003.

[17] T. Pirbodaghi, M. T. Ahmadian, and M. Fesanghary, "On the homotopy analysis method for non-linear vibration of beams," *Mechanics Research Communications*, vol. 36, no. 2, pp. 143–148, 2009.

[18] Y. M. Chen and J. K. Liu, "A study of homotopy analysis method for limit cycle of van der Pol equation," *Communications in Nonlinear Science and Numerical Simulation*, vol. 14, no. 5, pp. 1816–1821, 2009.

[19] B. T. Kennedy, D. C. Weggel, D. M. Boyajian, and R. E. Smelser, "Closed-form solution for a cantilevered sectorial plate subjected to a twisting tip moment," *Mechanics Research Communications*, vol. 35, no. 8, pp. 491–496, 2008.

[20] Y. M. Chen and J. K. Liu, "Uniformly valid solution of limit cycle of the Duffing-van der Pol equation," *Mechanics Research Communications*, vol. 36, no. 7, pp. 845–850, 2009.

[21] Y. M. Chen and J. K. Liu, "Homotopy analysis method for limit cycle flutter of airfoils," *Applied Mathematics and Computation*, vol. 203, no. 2, pp. 854–863, 2008.

[22] Y. M. Chen and J. K. Liu, "Homotopy analysis method for limit cycle oscillations of an airfoil with cubic nonlinearities," *JVC/Journal of Vibration and Control*, vol. 16, no. 2, pp. 163–179, 2010.

[23] S. J. Liao, "An optimal homotopy-analysis approach for strongly nonlinear differential equations," *Communications in Nonlinear Science and Numerical Simulation*, vol. 15, no. 8, pp. 2003–2016, 2010.

[24] Z. Niu and C. Wang, "A one-step optimal homotopy analysis method for nonlinear differential equations," *Communications in Nonlinear Science and Numerical Simulation*, vol. 15, no. 8, pp. 2026–2036, 2010.

[25] Y. H. Qian and S. M. Chen, "Accurate approximate analytical solutions for multi-degree-of-freedom coupled van der Pol-Duffing oscillators by homotopy analysis method," *Communications in Nonlinear Science and Numerical Simulation*, vol. 15, no. 10, pp. 3113–3130, 2010.

Hindawi Publishing Corporation
Advances in Acoustics and Vibration
Volume 2011, Article ID 195642, 6 pages
doi:10.1155/2011/195642

Research Article

Particle Swarm Optimization as an Efficient Computational Method in order to Minimize Vibrations of Multimesh Gears Transmission

Alexandre Carbonelli, Joël Perret-Liaudet, Emmanuel Rigaud, and Alain Le Bot

Laboratoire de Tribologie et Dynamique des Systèmes, UMR CNRS 5513, Ecole Centrale de Lyon, Universitè de Lyon, 36 Avenue Guy de Collongue, 69134 Ecully Cedex, France

Correspondence should be addressed to Alexandre Carbonelli, alexandre.carbonelli@ec-lyon.fr

Received 12 January 2011; Accepted 13 April 2011

Academic Editor: Snehashish Chakraverty

The aim of this work is to present the great performance of the numerical algorithm of Particle Swarm Optimization applied to find the best teeth modifications for multimesh helical gears, which are crucial for the static transmission error (STE). Indeed, STE fluctuation is the main source of vibrations and noise radiated by the geared transmission system. The microgeometrical parameters studied for each toothed wheel are the crowning, tip reliefs and start diameters for these reliefs. Minimization of added up STE amplitudes on the idler gear of a three-gear cascade is then performed using the Particle Swarm Optimization. Finally, robustness of the solutions towards manufacturing errors and applied torque is analyzed by the Particle Swarm algorithm to access to the deterioration capacity of the tested solution.

1. Introduction

The STE under load [1] is defined as the difference between the actual position of the driven gear and its theoretical position for a very slow rotation velocity and for a given applied torque. Its characteristics depend on the instantaneous situations of the meshing tooth pairs. Under load at very low speed (static transmission error), these situations result from tooth deflections, tooth surface modifications, and manufacturing errors. Under operating conditions, STE generates dynamic mesh force transmitted to shafts, bearings, and to the crankcase. The vibratory state of the crankcase is the main source of the radiated noise [2]. To reduce the radiated noise, the peak-to-peak amplitude of the STE fluctuation needs to be minimized by the mean of tooth modifications. It consists in micro-geometrical modifications listed below and displayed on Figure 1:

(i) tip relief magnitude $x_{\mathrm{rel},i}$, that is, the amount of material removed on the tooth tip,

(ii) start relief diameter $\Phi_{\mathrm{rel},i}$, that is, the diameter at which the material starts to be removed until the tooth tip. Linear or parabolic corrections can be done,

(iii) added up crowning centered on the active tooth width $C_{\beta,i/j}$.

Many authors [3–11] worked on the optimization of tooth modifications in simple mesh systems. Only few of them [12–14] considered multimesh systems as cascade of gears where idler gear modifications affect two meshes.

In this paper, the application is done on a cascade of three helical gears, displayed on Figure 2, for a total of 8 parameters (tip relief and start diameter for the relief for each gear, and added up crowning for a pair of meshing gears). Multiparameter optimization can easily become a difficult task if the algorithm used is not well adapted. We will show that the Particle Swarm Optimization (PSO) fits efficiently with that kind of problematic. Indeed, it permits to select a set of solutions more or less satisfying in the studied torque

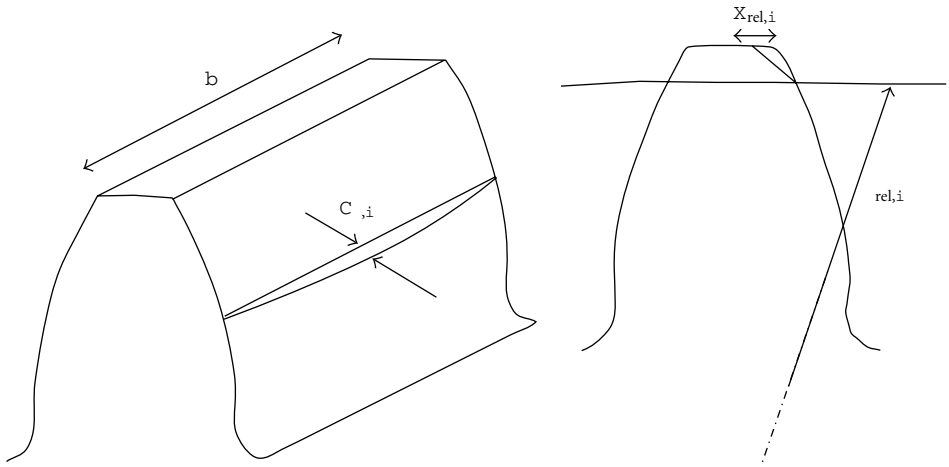

FIGURE 1: Crowning $C_{\beta,i/j}$, tip relief $x_{\text{rel},i}$, and start relief diameter $\Phi_{\text{rel},i}$.

range. Moreover, the robustness of the optimized solutions is studied regarding large manufacturing errors, lead, and involute alignment deviations. An additional difficulty arises because the modifications performed have to be efficient on a large torque range. The dispersion associated is the source of the strong variability of the dynamic behavior and of the noise radiated from geared systems (sometimes up to 10 dB [15, 16]).

2. Calculation of Static Transmission Error

The calculation of STE is relatively classical [17]. For each position θ of the driving gear, a kinematical analysis of the mesh allows determination of the theoretical contact line on the mating surfaces of gearing teeth within the plane of action.

Equation system which describes the elastostatic deformations of the teeth can be written as follows [17]:

$$\begin{aligned} \mathbf{H}^{\mathbf{u},\mathbf{F}}(\omega = 0) \cdot \mathbf{F} &= \delta(\theta) - \mathbf{e} - \mathbf{hertz}(\mathbf{F}), \\ \sum \mathbf{F_i} &= \mathbf{F}. \end{aligned} \tag{1}$$

The following data are needed to perform this interpolation:

(i) initial gaps **e** between the teeth: they are function of the geometry defects and the tooth modifications,

(ii) compliance matrix $\mathbf{H}^{\mathbf{u},\mathbf{F}}$, of the teeth coming from interpolation functions calculated by a Finite Element model of elastostatic deformations,

(iii) Hertz deformations **hertz**, calculated according to Hertz theory.

The calculation of the actual approach of distant teeth $\boldsymbol{\delta}$ on the contact line for each position θ permits to access the time variation of STE and its peak-to-peak amplitude E_{pp}, as a function of the applied torque (or the transmitted load F) and the teeth modifications. We chose linear correction

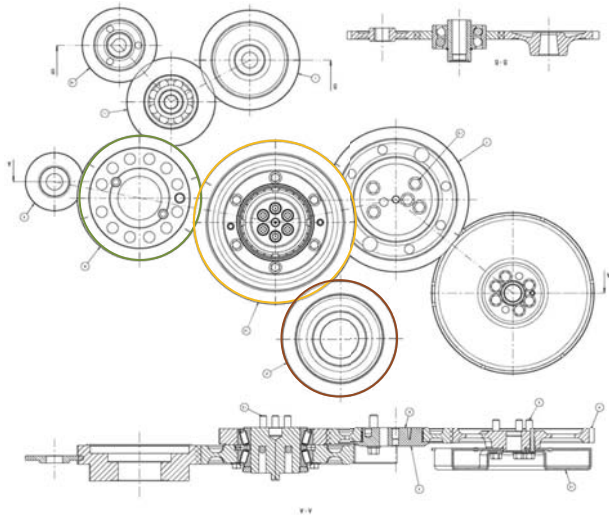

FIGURE 2: Cascade of the 3 helical gears studied: 50 teeth/72 teeth/54 teeth.

for tip reliefs and parabolic correction for the crownings. All the modifications allow to reduce the STE fluctuation. The most influent parameter is the tip relief magnitude. Indeed, removing an amount of material on the tooth tip permits to make up for the advance or late position of the tooth induced by elastic deformations.

For the robustness study, the manufacturing errors are also considered and displayed on Figure 3. The manufacturing is not directly parameters of the optimization but as they have an effect on the STE fluctuation they must be considered in the robustness study.

(i) Lead deviation: $f_{H\beta,i/j} = f_{H\beta,i} + f_{H\beta,j}$,

(ii) Involute alignment deviation: $f_{g\alpha,i}$ and $f_{g\alpha,j}$.

A fitness function f to minimize is defined as the integral of STE peak-to-peak amplitude over torque range

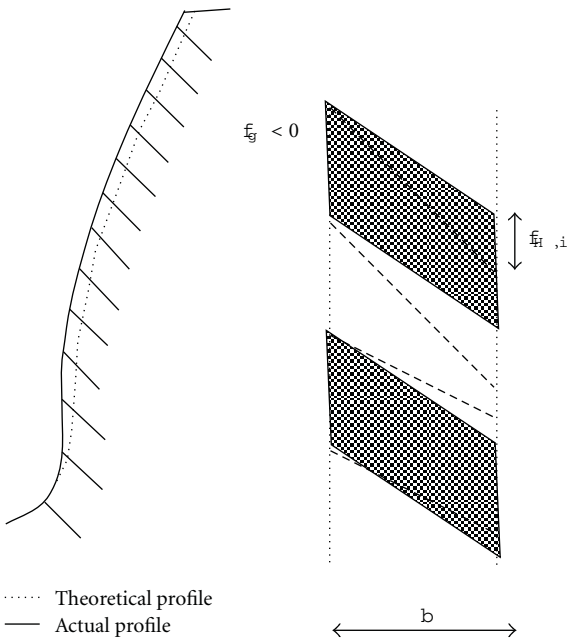

FIGURE 3: Involute alignment deviation $f_{g\alpha}$ and lead deviation $f_{H\beta}$.

$[C_{\min} - C_{\max}]$ approximated by Gaussian quadrature with 3 points.

$$f_{i,j} = \int_{C_{\min}}^{C_{\max}} E_{\text{pp}}(C)dC \longrightarrow \sum_{i=1}^{i=3} a_i E_{pp}(C_i). \tag{2}$$

The fitness function of the whole cascade is then

$$f = f_{i,j} + f_{k,j}. \tag{3}$$

We have thereby 8 parameters for the optimization leading to a combinatorial explosion. Meta-heuristic methods allow an efficient optimization, and we chose the Particle Swarm Optimization [18]. Obviously in that kind of problematic, the aim cannot be to access to the optimum optimorum but only different local minima whose performances can be quickly estimated over the torque range by a home-built gain function

$$G_0 = 10\log_{10}\left(\frac{f_{S_i}}{f_{\text{ref}}}\right), \tag{4}$$

where f_{ref} corresponds to the value of the fitness function for a standard nonoptimized gear.

3. Particle Swarm Algorithm

The principle of this method is based on the stigmergic behavior of a population, being in constant communication and exchanging information about their location in a given space [18]. Typically bees, ants, or termites are animals functioning that way. In our general case, we just consider particles which are located in an initial and random position in a hyperspace built according to the different optimization parameters. They will then change their position and their speed to search for the "best location," according to a defined criterion of optimization. It is commonly called the fitness function which has to be maximized or minimized depending on the problem.

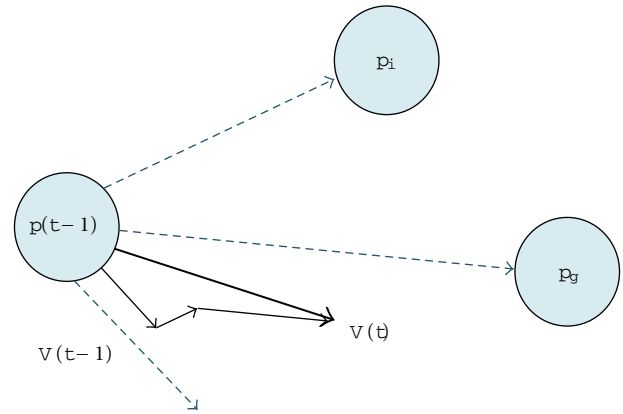

FIGURE 4: Particle Swarm algorithm representation.

For each iteration and each particle, a new speed and so a new position is reevaluated considering:

(i) the current particle velocity $V(t-1)$,

(ii) its best position p_i,

(iii) the best position of neighbors p_g.

The algorithm can thus be wrapped up to the system of (5) and Figure 4:

$$\begin{aligned}\mathbf{V}(t) &= \varphi_0\mathbf{V}(t-1) + \varphi_1\mathbf{A_1}\left[\mathbf{p}_i - \mathbf{p}(t-1)\right] \\ &\quad + \varphi_2\mathbf{A_2}\left[\mathbf{p}_g - \mathbf{p}(t-1)\right], \\ \mathbf{p}(t) &= \mathbf{p}(t-1) + \mathbf{V}(t-1).\end{aligned} \tag{5}$$

$\mathbf{A_1}$ and $\mathbf{A_2}$ represent a random vector of number between 0 and 1 and the parameters of these equations are taken following Trelea and Clerc [19–21]: $\varphi_0 = 0.729$ and $\varphi_1 = \varphi_2 = 1.494$.

4. Robustness Study

First the tolerance range $\mathbf{D_0}$ of a solution $\mathbf{x_0}$ has been defined, using a vector $\mathbf{\Delta x} = \{\Delta x_1, \Delta x_2, \ldots, \Delta x_N\}$, which takes in account the parameters variability. The gears studied have a precision class 7 (ISO 1328). Moreover, the manufacturing errors distribution is considered to be uniform over the range, which is the worst possible case in. Lead and involute alignment deviations and torque variation are associated in a 14-dimensionnal vector as following:

$$\begin{aligned}\Delta\mathbf{x} = \Big\{&\Delta X_{\text{dép},i}, \Delta\Phi_{\text{dép},i}, f_{g\alpha,i}, \Delta C_{\beta,i/j}, f_{H\beta,\,i/j}, \Delta X_{\text{dép},j}, \Delta\Phi_{\text{dép},j}, \\ &f_{g\alpha,j}, \ldots, \Delta C_{\beta,l/j}, f_{H\beta,l/j}, \Delta X_{\text{dép},l}, \Delta\Phi_{\text{dép},l}, f_{g\alpha,l}, \Delta C\Big\},\end{aligned} \tag{6}$$

where i, j, and l correspond to, respectively, the gears with 50, 72, and 54 teeth.

Table 1: Parameters ranges.

Number of teeth	$Z = 54$	$Z = 72$	$Z = 50$
Tip relief magnitude and tolerance [μm]	[15–150] ± 15	[0–150] ± 15	[15–150] ± 15
Start relief diameter and tolerance [mm]	[230–241] ± 0.46	[200–215] ± 0.46	[153–168] ± 0.40
Added up crowning and tolerance [μm]	[8–40] ± 8		—
	—	[8–40] ± 8	
Lead deviation and tolerance [μm]	0 ± 32		—
	—	0 ± 32	
Involution alignment dev. and tolerance [μm]	0 ± 12	0 ± 12	0 ± 12

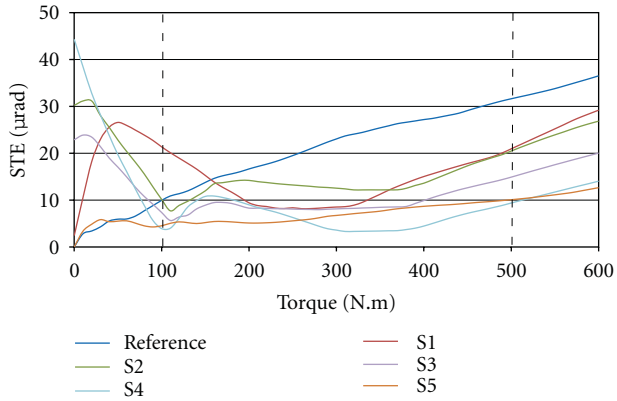

Figure 5: Optimized and reference solutions versus applied torque - - - - torque range boundaries.

Then, the tolerance range $\mathbf{D_0}$ can be written as

$$\mathbf{D_0} = \{\mathbf{x} : \mathbf{x} \in \mathbf{R^N} \mid \mathbf{x_0} - \Delta\mathbf{x} < \mathbf{x} < \mathbf{x_0} + \Delta\mathbf{x}\}. \quad (7)$$

Contrary to the case studied by Sundaresan et al. [22], the robustness study concerns micro-geometrical modifications instead of macrogeometrical parameters (i.e., teeth number). The tolerance ranges are moreover noticeably larger than the ones considered by Bonori et al. [10], especially for the tip relief modifications. The fitness function cannot be assumed monotonic and the study of the extreme boundaries of the problem is not sufficient. The PSO is then used to locate the maximum of the fitness function in the hyperspace $\mathbf{D_0}$, in order to analyze robustness of the solutions. The new values for the parameters which maximize the fitness function define the "degenerated solution," noted $\mathbf{x_d}$:

$$\mathbf{x_d} \in \mathbf{D_0}, \quad f(\mathbf{x_d}) = \max(f(\mathbf{x}) \mid \mathbf{x} \in \mathbf{D_0}). \quad (8)$$

With this additional criterion, optimal solution corresponds to the less deteriorated rather than the minimal E_{pp}.

5. Results

The cascade of three helical gears has to be optimized for torques from 100 Nm up to 500 Nm. A reference solution, with standard and not optimized tooth modifications, is used to emphasize the benefits of the Particle Swarm optimization.

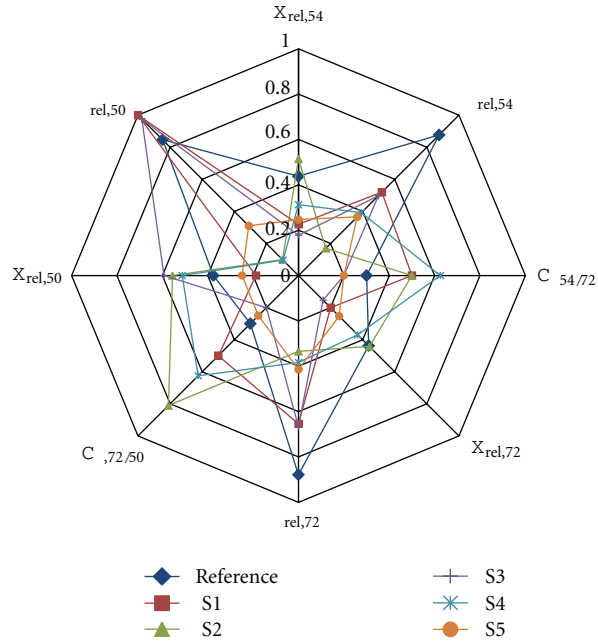

Figure 6: Optimized parameters of the solutions.

The PSO calculations have been performed using a population of 25 particles and stopped when a precision of 10^{-2} μrad for peak-to-peak amplitude E_{pp} is reached. The algorithm stops the calculation when no improvement is found 50 times successively. All the following results have converged after 250 to 400 iterations. That corresponds to 7500 to 10000 evaluations of the fitness function (instead of 10^{14} for a Monte-Carlo experiment). Table 1 lists the parameters ranges.

In order to illustrate the optimization process, Figure 5 displays 5 selected solutions—S1 to S5—corresponding to 5 local minima among the computed ones which all obviously are better than the reference solution in terms of minimal E_{pp}. Figure 6 displays the optimized parameters of the solutions rescaled in function of their extremum values.

According to the gain function (4), we can easily pick up the best solutions of the selected ones. Following the results listed in Table 2, solution S5, which provides −4.2 dB of improvement compared to the reference solution, should be selected.

Table 2: Gain of the computed optimal solutions compared to the reference solution.

Configuration	Gain G_0 [dB]
S1	−1.6
S2	−1.9
S3	−3.3
S4	−3.7
S5	−4.2

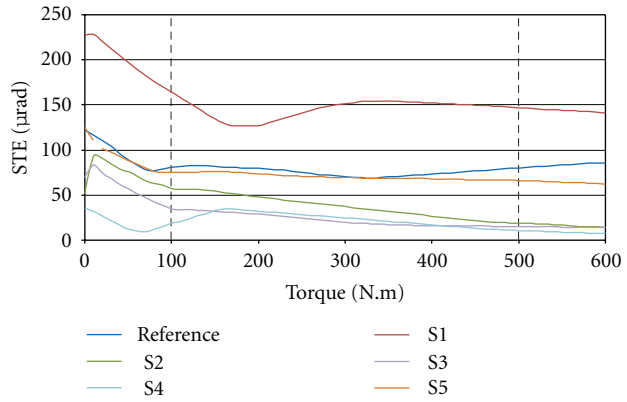

Figure 7: Degenerated solutions versus applied torque - - - - Torque range boundaries.

Figure 7 displays the deteriorated solutions.

The first analysis of the deteriorating capacity of the solutions can be done using gain function (9) and listing results in Table 3:

$$G_1 = 10\log_{10}\left(\frac{f_{\text{non-deteriorated}}}{f_{\text{deteriorated}}}\right). \quad (9)$$

The deteriorated reference solution has a gain of +6.7 dB compared with the initial reference solution. The solution S5 is worse considering the gain function (9), but its fitness function value is still less than the deteriorated reference solution one. On the other hand, the previous selected solution S4 appears as the best one with only +2.3 dB of deterioration in the gain function (9) sense.

The second analysis of the deteriorating capacity of the solutions can be done using gain function (10) and listing results in Table 4:

$$G_2 = 10\log_{10}\left(\frac{f_{S_i,\ \text{deteriorated}}}{f_{\text{ref},\ \text{deteriorated}}}\right). \quad (10)$$

The solution S1 emphasizes the importance of considering the deteriorating capacity. Indeed, although the optimal solution brings an improvement compared to the initial reference solution, it is likely to be less efficient taking in account the possible manufacturing errors. The previous choice has to be reconsidered. On the other hand, the solution S4 provides a good improvement of −3.7 dB compared to the reference solution and is quite robust as a gain of −6.2 dB is observed if S4 deteriorated solution is compared with the deteriorated reference solution.

Table 3: Gain of the degenerated solutions compared to optimal solutions.

Configuration	Gain G_1 [dB]
Reference	+6.7
S1	+11.3
S2	+6.0
S3	+6.1
S4	+2.3
S5	+11.3

Table 4: Gain of the degenerated solutions compared to the reference degenerated solution.

Configuration	Gain G_2 [dB]
S1	+2.8
S2	−2.6
S3	−4.2
S4	−6.2
S5	−0.4

6. Conclusion

Optimization with an efficient heuristic method (Particle Swarm) has been done to determinate optimized parameters of a multimesh problem. The algorithm permits the gathering of many solutions which all lead to really satisfying results over the torque range studied thank to an integration of STE peak-to-peak amplitude by Gaussian quadrature. Finally, a robustness criterion has been defined based on the deteriorating capacity of the solutions which permits to do a more accurate choice about the optimal tooth modifications. Indeed, there are many ways of estimating the robustness of the solutions. In some industrial point of view, a solution which is less efficient than another but much more robust should be preferably chosen.

Acknowledgments

This work has been supported by ANR (National Research Agency, contract number: ANR-08-VTT-007-02), ADEME (French Environment and Energy Management Agency), and Lyon Urban Trucks&Bus competitiveness cluster. The authors acknowledge gratefully this support and especially thank Denis BARDAY from Renault Trucks Company for his inestimable help.

References

[1] L.S. Harris, "Dynamic loads on the teeth of spur gears," in *Proceedings of the Institution of Mechanical Engineers*, vol. 172, pp. 87–112, 1958.

[2] D. B. Welbourn, "Fundamental knowledge of gear noise—a survey," in *Proceedings of the Conference on Noise and Vibrations of Engines and Transmissions*, vol. C177/79, pp. 9–29, Cranfield Institute of Technology, July 1979.

[3] M. S. Tavakoli and D. R. Houser, "Optimum profile modifications for the minimization of static transmission errors of spur gears," *Journal of Mechanism, Transmissions, and Automation in Design*, vol. 108, no. 1, pp. 86–95, 1986.

[4] A. Kahraman and G. W. Blankenship, "Effect of involute tip relief on dynamic response of spur gear pairs," *Journal of Mechanical Design*, vol. 121, no. 2, pp. 313–315, 1999.

[5] K. Umezawa, H. Houjoh, S. Matsumura, and S. Wang, "Investigation of the dynamic behavior of a helical gear system dynamics of gear pairs with bias modification," in *Proceedings of the 4th World Congress and Gearing and Power Transmissions*, vol. 3, pp. 1981–1990, Paris, France, 1999.

[6] M. Beghini et al., "A method to define profile modification of spur gear and minimize the transmission error," in *Proceedings of the Fall Technical Meeting of the American Gear Manufacturers Association (AGMA '04)*, Milwaukee, Wis, USA, October 2004.

[7] M. Umeyama, "Effects of deviation of tooth surface errors of a helical gear pair on the transmission error," *Transactions of the Japan Society of Mechanical Engineers, Part C*, vol. 61, no. 587, pp. 3101–3107, 1995.

[8] R. Guilbault, C. Gosselin, and L. Cloutier, "Helical gears, effects of tooth deviations and tooth modifications on load sharing and fillet stresses," *Journal of Mechanical Design*, vol. 128, no. 2, pp. 444–456, 2006.

[9] A. Kahraman, P. Bajpai, and N. E. Anderson, "Influence of tooth profile deviations on helical gear wear," *Journal of Mechanical Design*, vol. 127, no. 4, pp. 656–663, 2005.

[10] G. Bonori, M. Barbieri, and F. Pellicano, "Optimum profile modifications of spur gears by means of genetic algorithms," *Journal of Sound and Vibration*, vol. 313, no. 3–5, pp. 603–616, 2008.

[11] S. Kurokawa, Y. Ariura, and M. Ohtahara, "Transmission errors of cylindrical gears under load—influence of tooth profile modification and tooth deflection," in *Proceedings of the 7th International Power Transmission and Gearing Conference*, DE 88, pp. 213–217, American Society of Mechanical Engineers, Design Engineering Division, San Diego, Calif, USA, October 1996.

[12] T. Erltenel and R. G. Parker, "A static and dynamic model for three-dimensional, multi-mesh gear systems," in *Proceedings of the ASME International Design Engineering Technical Conferences and Computers and Information in Engineering Conference (DETC '05)*, vol. 5, pp. 945–956, Long Beach, Calif, USA, September 2005.

[13] H. Vinayak, R. Singh, and C. Padmanabhan, "Linear dynamic analysis of multi-mesh transmissions containing external, rigid gears," *Journal of Sound and Vibration*, vol. 185, no. 1, pp. 1–32, 1995.

[14] J. Lin and R. G. Parker, "Mesh stiffness variation instabilities in two-stage gear systems," *Journal of Vibration and Acoustics*, vol. 124, no. 1, pp. 68–76, 2002.

[15] N. Driot, E. Rigaud, J. Sabot, and J. Perret-Liaudet, "Allocation of gear tolerances to minimize gearbox noise variability," *Acta Acustica United with Acustica*, vol. 87, no. 1, pp. 67–76, 2001.

[16] N. Driot and J. Perret-Liaudet, "Variability of modal behavior in terms of critical speeds of a gear pair due to manufacturing errors and shaft misalignments," *Journal of Sound and Vibration*, vol. 292, no. 3–5, pp. 824–843, 2006.

[17] E. Rigaud and D. Barday, "Modelling and analysis of static transmission error of gears: effect of wheel body deformation and interactions between adjacent loaded teeth," *Mécanique Industrielle et Matériaux*, vol. 51, no. 2, pp. 58–60, 1998.

[18] R. C. Eberhart and J. Kennedy, "A new optimizer using particle swarm theory," in *Proceedings of the 6th International Symposium on Micro Machine and Human Science*, pp. 39–43, IEEE Service Center, Nagoya, Japan, October 1995.

[19] I. C. Trelea, "The particle swarm optimization algorithm: convergence analysis and parameter selection," *Information Processing Letters*, vol. 85, no. 6, pp. 317–325, 2003.

[20] M. Clerc, "The swarm and the queen: towards a deterministic and adaptive particle swarm optimization," in *Proceedings of the International Conference on Evolutionary Computation (ICEC '99)*, pp. 1951–1957, IEEE, Washington, DC, USA, 1999.

[21] M. Clerc and J. Kennedy, "The particle swarm—explosion, stability, and convergence in a multidimensional complex space," *IEEE Transactions on Evolutionary Computation*, vol. 6, no. 1, pp. 58–73, 2002.

[22] S. Sundaresan, K. Ishii, and D. R. Houser, "A robust optimization procedure with variations on design variables and constraints," *Engineering Optimization*, vol. 24, no. 2, pp. 110–118, 1995.

Hindawi Publishing Corporation
Advances in Acoustics and Vibration
Volume 2011, Article ID 637138, 12 pages
doi:10.1155/2011/637138

Research Article

Hybrid Swarm Algorithms for Parameter Identification of an Actuator Model in an Electrical Machine

Ying Wu,[1] Sami Kiviluoto,[2] Kai Zenger,[2] X. Z. Gao,[2] and Xianlin Huang[1]

[1] *Centre for Control Theory and Guidance Technology, Harbin Institute of Technology, Harbin 150000, China*
[2] *Department of Automation and Systems Technology, Aalto University School of Electrical Engineering, P.O. Box 15500, FI-00076 Aalto, Finland*

Correspondence should be addressed to Kai Zenger, kai.zenger@tkk.fi

Received 15 December 2010; Accepted 4 March 2011

Academic Editor: Snehashish Chakraverty

Efficient identification and control algorithms are needed, when active vibration suppression techniques are developed for industrial machines. In the paper a new actuator for reducing rotor vibrations in electrical machines is investigated. Model-based control is needed in designing the algorithm for voltage input, and therefore proper models for the actuator must be available. In addition to the traditional prediction error method a new knowledge-based Artificial Fish-Swarm optimization algorithm (AFA) with crossover, CAFAC, is proposed to identify the parameters in the new model. Then, in order to obtain a fast convergence of the algorithm in the case of a 30 kW two-pole squirrel cage induction motor, we combine the CAFAC and Particle Swarm Optimization (PSO) to identify parameters of the machine to construct a linear time-invariant(LTI) state-space model. Besides that, the prediction error method (PEM) is also employed to identify the induction motor to produce a black box model with correspondence to input-output measurements.

1. Introduction

One of the fundamental processes of control is the parameter identification. In control engineering a lot of effort has been done to develop methods to identify the system model and its parameters. A wide range of techniques such as the least squares method, the maximum likelihood method, and the cross correlation method, exist for system identification [1]. However, a drawback of traditional identification methods is their dependence on unrealistic assumptions such as unimodal performance landscapes and differentiability of the cost function. Consequently, some problems are oversimplified to fulfil such assumptions. Stochastic search algorithms such as evolutionary-based algorithms seem to be a promising alternative to these conventional methods. Swarm Intelligence is one of the most important branches for Evolutionary Algorithms, which has been widely used in identification problems [2–4].

The Artificial Fish-Swarm Algorithm (AFA) and the Particle Swarm Optimization (PSO) are two kinds of typical Swarm Intelligence methods [5]. The AFA is an animal behaviour-based optimization method and, like the PSO, which was firstly developed by Li and Eberhart and Kennedy, respectively [6–9]. PSO has been widely used in identification in many research fields [10–15]. However, there are few researches to apply the AFA in such kind of problems. The AFA can search for the global optimum effectively and has a certain adaptive ability for searching space. But the AFA individual behaviour is to hunt for local optimum. Therefore, avoiding individual premature becomes difficult. In this case, artificial fish will be stuck into local optima when dealing with multimodal optimization problems. To improve the performance of AFA is an im-portant challenge for applying the AFA in real problems [16].

In order to guide the evolutionary-based stochastic algorithms, a novel optimization method, the Cultural Algorithm

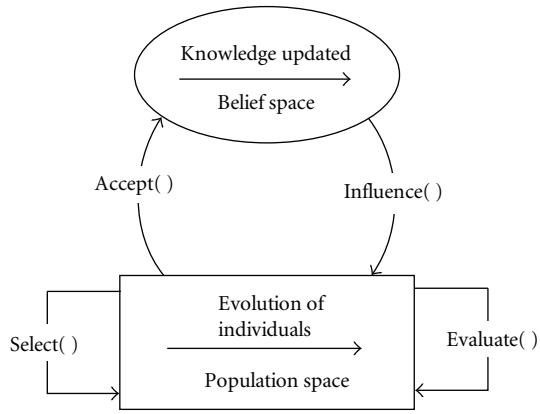

Figure 1: Culture algorithm framework.

(CA) proposed by Reynolds in 1994 was developed to demanding problems, due to its flexibility and efficiency [17]. The CA is a class of computational models derived from the principles of the culture evolution in nature, composed by the population space, the belief space and a communication protocol. In the CA, the evolution takes place in the population space. The knowledge generated from the experiences of the individuals is stored in the belief space. The communication protocol can be depicted as an acceptance function and an influence function, which is utilized to make interaction between the other two components [18, 19]. Various evolutionary algorithms have been utilized in the population space of the CA leading to good results [20–27]. The framework of the culture algorithm can be depicted in Figure 1.

The motivation behind this work is twofold. Firstly, in the literature there seems to be no results on hybrid AFA and CA. The knowledge stored in the belief space do act as a significant role in the process of evolution, and we try to find a proper framework for updating the belief space in combining the CA and AFA. Secondly, the new hybrid algorithm is applied to identify the parameters of a new kind of actuator, which is used to suppress rotor vibrations of an electronic machine.

As part of our investigation, two typical kinds of knowledge in CA, the situation knowledge and the normative knowledge, are stored in the belief space to update the population space and to establish the relationship between the two spaces in the CA. The performance of the CAFAC is explored using offline parameter identification of the actuator-rotor system in an electrical machine. The identification is performed based on a lower-order physical linear time invariant (LTI) parametric state-space model of the actuator-rotor system. The resulting model can be utilized to design model-based active control algorithms for vibrations reduction.

The rest of this paper is organized as follows. Section 2 briefly introduces the background knowledge of the system under control and the AFA. Section 3 proposes and discusses the underlying principle of the CAFAC. In Section 4 the identification of an actuator-rotor system is considered using CAFAC and PEM and simulation results showing the control performance is established. A few conclusions and remarks are given in Section 5.

2. Problem Statement and Preliminaries

2.1. The Parametric Model of the Actuator-Rotor System. We examine a two-pole cage induction motor equipped with a built-in force actuator, which actively generates force on the rotor (Figure 2(a)). The actuator is a four-pole extra winding inside the stator slots (Figure 2(b)). This design allows producing additional forces without harming the normal operation of the motor. The actuator is controlled by two voltage signals that by design induce forces on the rotor in horizontal and vertical directions (x and y).

The most important measurements for the identification are obtained using eddy current sensor. The sensors, conforming to the control signals, measure the rotor position also in horizontal and vertical directions. With them it is possible to record the rotor movement in any conditions accurately. Another set of sensors has been added on the right side of the motor in order to improve accuracy. Another important measurement devise is the encoder that provides the rotational angle and frequency of the rotor.

In the identification measurement the motor was operating at 32.085 Hz and the excitation input (control voltages in horizontal and vertical directions) was a uniform random number signal with frequency content up to 500 Hz. The output data was then processed so that the effects of vibrations were removed and only the response to the excitation signals remained [28]. The processed measurement is displayed in Figure 3.

The data from this setup is used to obtain a mathematical actuator model that can be used for control design purposes, when the objective is compensating rotor vibrations. The motivation of obtaining a new parametric physical model is increased understanding of the model compared to a black box model, which has been used before successfully [29]. Parametric models have been identified before with data from a finite element model, but they do not describe the test motor and some of the identified parameters had complex values, although for a realistic machine the parameters such as resistances must be realvalued.

The linear time-invariant parametric (LTI) model of the system will be discussed. The model for the induction motor according to [30] is based on the mechanical model in modal coordinates [31]

$$\ddot{\eta} + 2\Omega\Xi\dot{\eta} + \Omega^2 = \Phi_{rc}^T f_c + \Phi_{rc}^T f_{\text{ex}}, \tag{1}$$

$$u_{rc} = \Phi_{rc}\eta, \tag{2}$$

where η is the modal coordinate vector, u_{rc} is the displacement in x-direction and y-direction, Φ_{rc} is the modal matrix, Ω is a diagonal matrix, and Ξ is the modal damping matrix, f_{ex} denotes the sinusoidal disturbance causing rotor vibration disturbance, and f_c the electro mechanical force

(a) (b)

Figure 2: (a) The test motor [28]. Eddy current sensors are positioned on top of the rotor and behind it on the left. Encoder is located on the left side of the machine in the end of the rotor. (b) Control windings are built in the stator slots inside the motor [28].

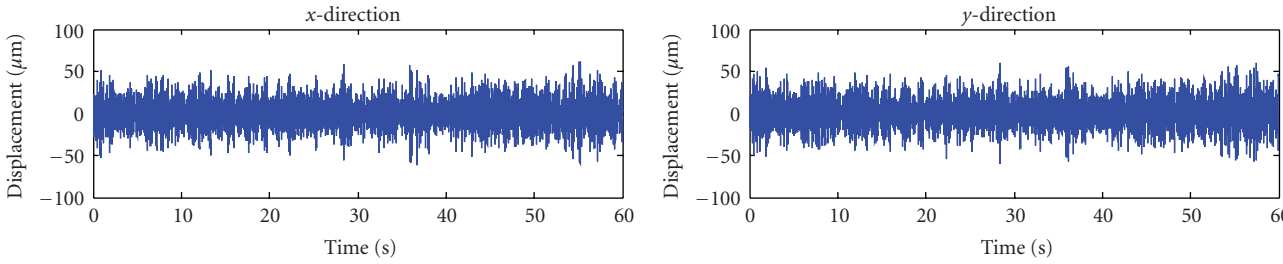

(a) (b)

Figure 3: The response to control voltages in x- and y-directions.

acting on the rotor. The model structure is the same as in [32]

$$\frac{d}{dt}\begin{pmatrix}\dot{\eta}\\ \eta\\ i\end{pmatrix} = \begin{bmatrix}-2\Omega\Xi & \Phi_{rc}^T P_{em}\Phi_{rc} - \Omega^2 & \Phi_{rc}^T C_{em}\\ I & 0 & 0\\ S_{em}\Phi_{rc} & Q_{em}\Phi_{rc} & A_{em}\end{bmatrix}\begin{pmatrix}\dot{\eta}\\ \eta\\ i\end{pmatrix} + \begin{bmatrix}0 & \Phi_{rc}^T\\ 0 & 0\\ B_{em} & 0\end{bmatrix}\begin{pmatrix}v\\ f_{\text{ex}}\end{pmatrix}, \tag{3}$$

$$u_{rc} = \begin{bmatrix}0 & \Phi_{rc} & 0\end{bmatrix}\begin{pmatrix}\dot{\eta}\\ \eta\\ i\end{pmatrix}.$$

The input $v = (\text{Re}(\hat{\underline{u}}_{c,0}), \text{Im}(\hat{\underline{u}}_{c,0}))$, is the control voltage, the first block row is the mechanical model, and $i = (\text{Re}(\hat{\underline{i}}_{c,0}), \text{Re}(M_{r,c,2}\hat{\underline{i}}_{r,2,0})^{\text{T}}, \text{Im}(\hat{\underline{i}}_{c,0}), \text{Im}(M_{r,c,2}\hat{\underline{i}}_{r,2,0}))^{\text{T}}$, where $\hat{\underline{i}}_{c,0}$ and $\hat{\underline{i}}_{r,2,0}$ are current space vectors and $M_{r,c,2}$ included in i is mutual inductance of control winding and the rotor cage. In variables the subscript c denotes a relation to the control winding, the subscript r denotes a relation to the rotor cage inside the motor, and the number in subscript denotes harmonic component [33]. All the parameters for the model are based on measured data and their explanations are listed in Table 1 [30].

Following [30, 32] a combined electromechanical model can be derived starting from the voltage-flux equation for the control winding and the equation for rotor cage four-pole harmonic in stator coordinates

$$\begin{aligned}\hat{\underline{u}}_c &= R_c\hat{\underline{i}}_c + \frac{d\hat{\underline{\psi}}_{c,2}}{dt},\\ 0 &= R_{r,2}\hat{\underline{i}}_{r,2} + \frac{d\hat{\underline{\psi}}_{r,2}}{dt} - j2\omega_m\hat{\underline{\psi}}_{r,2}.\end{aligned} \tag{4}$$

The four-pole harmonic flux leakages are

$$\begin{aligned}\hat{\underline{\psi}}_{c,2} &= L_c\hat{\underline{i}}_c + M_{r,c,2}\hat{\underline{i}}_{r,2} + X_{c,\epsilon,2}\hat{\underline{B}}_1\underline{z}_r,\\ \hat{\underline{\psi}}_{r,2} &= L_{r,2}\hat{\underline{i}}_{r,2} + M_{c,r,2}\hat{\underline{i}}_c + X_{r,\epsilon,2}\hat{\underline{B}}_1\underline{z}_r.\end{aligned} \tag{5}$$

By substitution

$$\hat{\underline{u}}_{c,0} = (R_c + j\omega_1 L_c)\hat{\underline{i}}_{c,0} + L_c\frac{d\hat{\underline{i}}_{c,0}}{dt} + j\omega_1 M_{r,c,2}\hat{\underline{i}}_{r,2,0} + \frac{d}{dt}\left(M_{r,c,2}\hat{\underline{i}}_{r,2,0}\right) + X_{c,\epsilon,2}\underline{B}_1(\dot{\underline{z}}_r + j\omega_1\underline{z}_r),$$

Table 1: Parameters in the electromechanical model.

Parameter	Unit	Explanation
R_c	mΩ	The resistance of the control winding.
L_c	mH	The inductance of the control winding.
$k_c\underline{B}_1^*$	N/(A·m)	The eccentricity coupling factor of the control winding multiplied with the complex conjugate of the first air-gap field harmonic [34].
$M_{r,c,2}\widetilde{M}_{c,r,2}$	mH	Mutual inductance of rotor cage and control winding multiplied by itself and divided by rotor cage inductance of four-pole harmonic ($M_{c,r,2}\cdot M_{c,r,2}/L_{r,2}$).
$\gamma_{r,2}$	1/s	$R_{r,2}M_{c,r,2}/L_{r,2}$, where $R_{r,2}$ is the rotor cage resistant of 4-pole harmonic.
$X_{c,\epsilon,2}\underline{B}_1$	Wb/m	The eccentricity coupling factor of control winding multiplied with first air-gap field harmonic.
α	T^2	A coefficient related to the unbalanced magnetic pull towards the shortest air-gap (gap between stator and rotor) [33].
$k_{r,2}B_1^*/M_{r,c,2}$	N/(m·Wb)	The coupling factor of rotor cage multiplied with the complex conjugate of the first air-gap field harmonic and divided by rotor cage inductance of four-pole harmonic.
$\widetilde{X}_{r,\epsilon,2}\underline{B}_1/M_{r,c,2}$	Wb/m	The eccentricity coupling factor of rotor cage four-pole harmonic multiplied with the first air-gap field harmonic and divided by rotor cage inductance of four-pole harmonic.

$$\begin{aligned}0 &= (\gamma_{r,2}+j\omega_2)M_{r,c,2}\hat{\underline{i}}_{r,2,0}+\frac{d}{dt}\left(M_{r,c,2}\hat{\underline{i}}_{r,2,0}\right)\\&\quad+j\omega_2 M_{r,c,2}\widetilde{M}_{c,r,2}\hat{\underline{i}}_{c,0}+M_{r,c,2}\widetilde{M}_{c,r,2}\frac{d\hat{\underline{i}}_{c,0}}{dt}\\&\quad+M_{r,c,2}\widetilde{X}_{r,\epsilon,2}\underline{B}_1\left[\dot{\underline{z}}_r+j\omega_2\underline{z}_r\right],\end{aligned}\tag{6}$$

where $\underline{z}$ is a complex coordinate representation of the rotor eccentricity. In addition, the control force f_c in terms of the parameters in Table 1 is given by

$$\begin{aligned}f_c &= \underbrace{\frac{\pi d_r l_r}{4\mu_0\delta_0}\left[\alpha\underline{z}_r+\underline{\beta}e^{j2\omega_1 t}\underline{z}_r^*\right]}_{\Rightarrow P_{em}(t)}\\&\quad+\underbrace{\frac{\pi d_r l_r}{4\delta_0}\underline{B}_1^*\left[\left(\frac{k_{r,2}}{M_{r,c,2}}\right)M_{r,c,2}\hat{\underline{i}}_{r,2,0}+k_c\hat{\underline{i}}_{c,0}\right]}_{\Rightarrow C_{em}}.\end{aligned}\tag{7}$$

These equations include all the parameters to identify. Since the complex coordinate system of $\underline{z}$ is decomposed in real and imaginary parts in the final model, matrices $P_{em}(t)$ and C_{em}, are given by

$$\begin{aligned}P_{em}(t) = \frac{\pi d_r l_r}{4\mu_0\delta_0}\Bigg(&\begin{bmatrix}\mathrm{Re}\{\alpha\} & -\mathrm{Im}\{\alpha\}\\ \mathrm{Im}\{\alpha\} & \mathrm{Re}\{\alpha\}\end{bmatrix}\\&+\begin{bmatrix}\mathrm{Re}\{\beta e^{j2\omega_1 t}\} & \mathrm{Im}\{\beta e^{j2\omega_1 t}\}\\ \mathrm{Im}\{\beta e^{j2\omega_1 t}\} & -\mathrm{Re}\{\beta e^{j2\omega_1 t}\}\end{bmatrix}\Bigg),\end{aligned}\tag{8}$$

$$C_{emC} = \frac{\pi d_r l_r}{4\delta_0}\left[k_c\underline{B}_1^* \quad \left(\frac{k_{r,2}}{M_{r,c,2}}\right)\underline{B}_1^*\right],\tag{9}$$

$$C_{em} = \begin{bmatrix}\mathrm{Re}\{C_{emC}\} & -\mathrm{Im}\{C_{emC}\}\\ \mathrm{Im}\{C_{emC}\} & \mathrm{Re}\{C_{emC}\}\end{bmatrix}.\tag{10}$$

It should be noted that in the time-invariant case $P_{em}(t)$ is constant P_{em}.

Equation (6) can be written in matrix form

$$\begin{aligned}&\begin{bmatrix}L_c & 1\\ M_{r,c,2}\widetilde{M}_{c,r,2} & 1\end{bmatrix}\times\frac{d}{dt}\begin{bmatrix}\hat{\underline{i}}_{c,0}\\ M_{r,c,2}\hat{\underline{i}}_{r,2,0}\end{bmatrix}\\&+\begin{bmatrix}R_c+j\omega_1 L_c & j\omega_1\\ j\omega_2 M_{r,c,2}\widetilde{M}_{c,r,2} & \gamma_{r,2}+j\omega_2\end{bmatrix}\begin{bmatrix}\hat{\underline{i}}_{c,0}\\ M_{r,c,2}\hat{\underline{i}}_{r,2,0}\end{bmatrix}\\&+\begin{bmatrix}X_{c,\epsilon,2}\underline{B}_1\\ M_{r,c,2}\widetilde{X}_{r,\epsilon,2}\underline{B}_1\end{bmatrix}\dot{\underline{z}}_r+\begin{bmatrix}j\omega_1 X_{c,\epsilon,2}\underline{B}_1\\ j\omega_1 M_{r,c,2}\widetilde{X}_{r,\epsilon,2}\underline{B}_1\end{bmatrix}\underline{z}_r=\begin{bmatrix}1\\0\end{bmatrix}\hat{\underline{u}}_{c,0}.\end{aligned}\tag{11}$$

Rearranging this will give the rest of the matrices, which are needed for the combined model

$$\begin{aligned}&\frac{d}{dt}\begin{bmatrix}\hat{\underline{i}}_{c,0}\\ M_{r,c,2}\hat{\underline{i}}_{r,2,0}\end{bmatrix}\\&=\underbrace{-\begin{bmatrix}L_c & 1\\ M_{r,c,2}\widetilde{M}_{c,r,2} & 1\end{bmatrix}^{-1}\begin{bmatrix}X_{c,\epsilon,2}\underline{B}_1\\ M_{r,c,2}\widetilde{X}_{r,\epsilon,2}\hat{\underline{B}}_1\end{bmatrix}}_{S_{emC}}\dot{\underline{z}}_r\\&\quad\underbrace{-\begin{bmatrix}L_c & 1\\ M_{r,c,2}\widetilde{M}_{c,r,2} & 1\end{bmatrix}^{-1}\begin{bmatrix}j\omega_1 X_{c,\epsilon,2}\underline{B}_1\\ j\omega_1 M_{r,c,2}\widetilde{X}_{r,\epsilon,2}\underline{B}_1\end{bmatrix}}_{Q_{emC}}\underline{z}_r\\&\quad\underbrace{-\begin{bmatrix}L_c & 1\\ M_{r,c,2}\widetilde{M}_{c,r,2} & 1\end{bmatrix}^{-1}\begin{bmatrix}R_c+j\omega_1 L_c & j\omega_1\\ j\omega_2 M_{r,c,2}\widetilde{M}_{c,r,2} & \gamma_{r,2}+j\omega_2\end{bmatrix}}_{A_{emC}}\end{aligned}$$

$$\times \begin{bmatrix} \hat{\underline{i}}_{c,0} \\ M_{r,c,2}\hat{\underline{i}}_{r,2,0} \end{bmatrix} + \underbrace{\begin{bmatrix} L_c & 1 \\ M_{r,c,2}\widetilde{M}_{c,r,2} & 1 \end{bmatrix}^{-1} \begin{bmatrix} 1 \\ 0 \end{bmatrix}}_{B_{emC}} \hat{\underline{u}}_{c,0}. \tag{12}$$

Matrices A_{em}, B_{em}, S_{em}, and Q_{em} are finally obtained like C_{em} in (10)

$$A_{em} = \begin{bmatrix} \mathrm{Re}\{A_{emC}\} & -\mathrm{Im}\{A_{emC}\} \\ \mathrm{Im}\{A_{emC}\} & \mathrm{Re}\{A_{emC}\} \end{bmatrix},$$

$$B_{em} = \begin{bmatrix} \mathrm{Re}\{B_{emC}\} & -\mathrm{Im}\{B_{emC}\} \\ \mathrm{Im}\{B_{emC}\} & \mathrm{Re}\{B_{emC}\} \end{bmatrix},$$

$$S_{em} = \begin{bmatrix} \mathrm{Re}\{S_{emC}\} & -\mathrm{Im}\{S_{emC}\} \\ \mathrm{Im}\{S_{emC}\} & \mathrm{Re}\{S_{emC}\} \end{bmatrix}, \tag{13}$$

$$Q_{em} = \begin{bmatrix} \mathrm{Re}\{Q_{emC}\} & -\mathrm{Im}\{Q_{emC}\} \\ \mathrm{Im}\{S_{emC}\} & \mathrm{Re}\{Q_{emC}\} \end{bmatrix}.$$

These matrices and the mechanical model (1) can be combined in one state-space model (3).

The parameters of the electromechanical model are listed in Table 1. Certain practical constraints were set for the parameters for fulfilling physical quantities. Here the resistance is constant and known (14.5), so it does not need to be optimized. When the effect of the unbalanced magnetic pull is ignored we can get the LTI model. The input $u(t)$ consists of the voltage input v to the control winding and the disturand the outputs are the displacements u_{rc} of the rotor center. The system matrices A, B, and C are the functions of the unknown parameters in the model which are reformed in a vector as

$$P = \left\{ L_c, k_c\underline{B}_1^*, M_{r,c,2}\widetilde{M}_{c,r,2}, \gamma_{r,2}, X_{c,\epsilon,2}\underline{B}_1, \alpha, \frac{k_{r,2}\underline{B}_1^*}{M_{r,c,2}}, \frac{\widetilde{X}_{c,\epsilon,2}\underline{B}_1}{M_{r,c,2}} \right\}. \tag{14}$$

The corresponding significances of the unknown parameters, and the detailed derivation of the model can be found in [32].

2.2. The Artificial Fish-Swarm Algorithm. Suppose that the problem under consideration has D-dimensions. Initialize the swarm with N artificial fish. The state of one artificial fish can be formulated as $X_i = (x_{i1}, x_{i2}, \ldots, x_{iD})$, $i = 1, \ldots, N$, where X_i represents the target variable for the problem under consideration. $y = f(X_i)$ stands for the food concentration of the artificial fish currently, where it is the objective function. The basic behaviours of artificial fish can be expressed as follows ($d_{ij} = \|X_j - X_i\|$ stands for the Euclidean distance between X_i and X_j, "vd" is visual distance of the artificial fish individual, "s" is the size of the movement of artificial fish, δ is the crowd factor of the artificial fish) [6].

(1) Preying. The current state of the artificial fish is X_i, the artificial fish selects a state X_j randomly within the visual distance, such as $X_j = X_i + \mathrm{rand}(0,1) \times \mathrm{vd}$. If $f(X_j) < f(X_i)$ the artificial fish moves from X_i towards X_j, meaning that $X_i^t \rightarrow X_i^{t+1}$. The formulation can be depicted as follows:

$$X_i^{t+1} = X_i^t + \mathrm{rand}(0,1) \times s \times \frac{X_j^t - X_i^t}{\left\| X_j^t - X_i^t \right\|}. \tag{15}$$

If $f(X_j) > f(X_i)$, the artificial fish selects another state randomly again. If the artificial fish cannot meet the requirement in a given time, then it moves one step randomly as

$$X_i^{t+1} = X_i^t + \mathrm{rand}(0,1) \times s. \tag{16}$$

(2) Swarming. The current state of the artificial fish is X_i, nf is the number of its fellows within the visual distance, equal to the number of elements in the set of $B = \{X_j \mid d_{ij} \leq \mathrm{Visual}\}$. If $\mathrm{nf} \neq 0$ that is the set B is not empty, let $X_{\mathrm{center}} = \sum_{j=1}^{\mathrm{nf}} X_j/\mathrm{nf}$ and then $y_{\mathrm{center}} = f(X_{\mathrm{center}})$ stands for the fitness of the centre position. If $\mathrm{nf} \times y_{\mathrm{center}} < \delta \times y_i$, meaning that this area is not crowded, then if $y_{\mathrm{center}} < y_i$, the artificial fish moves one step towards the centre position:

$$X_i^{t+1} = X_i^t + \mathrm{rand}(0,1) \times s \times \frac{X_c^t - X_i^t}{\|X_c^t - X_i^t\|}. \tag{17}$$

Otherwise it executes the behaviour of preying.

(3) Chasing. The current state of the artificial fish is X_i, $X_{\min}$ stands for the best artificial fish individual within X_i's visual distance. nf is the number of $X_{\min}$'s fellows within the visual distance. $y_{\min} = f(X_{\min})$, if $y_{\min} < y_i$ and $\mathrm{nf} \times y_{\min} < \delta \times y_i$, the artificial fish moves one step to $X_{\min}$:

$$X_i^{t+1} = X_i^t + \mathrm{rand}(0,1) \times s \times \frac{X_{\min}^t - X_i^t}{\|X_{\min}^t - X_i^t\|}. \tag{18}$$

Otherwise it executes the behaviour of preying.

3. Hybrid Optimization Methods of Articificial Fish Algorithm and Culture Algorithm

Here, the fish swarm is regarded as the population space, where the domain knowledge is extracted from. Then the domain knowledge is formed and stored in belief space so as to model and impact the evolution of the population at iteration. In four versions of CAFAC, we use the situation knowledge and the normative knowledge to guide the direction and the step size of the evolution. Both of them can be depicted as follows.

3.1. Structures of Belief Space in CAFAC. The situational knowledge provides a set of best individuals available for the interpretation of specific individual experience [19]. Here, the situational exemplar set consists of only the best fish found so far, $S = \langle S^t \mid S^t = \{s_1^t, s_2^t, \ldots, s_n^t\} \rangle$, S^t stands for

the best fish in the swarm at iteration t. In other words, it can be initialized with the best fish in the initial fish swarm and updated by the following function:

$$s_j^{t+1} = \begin{cases} X_{\text{gbest},j}^{t+1} & \text{if } f\left(X_{\text{gbest}}^{t+1}\right) < f(s^t), \\ s_j^t & \text{otherwise,} \end{cases} \tag{19}$$

where $X_{g\text{best}}^{t+1}$ denotes the best artificial fish individual in the fish swarm at generation $t+1$.

The normative knowledge can give the feasible solution space of the optimization problems under consideration [19]. It is a set of information for each variable and is given as

$$N = \langle I, U, L, D \rangle, \tag{20}$$

where U, L and D are n-dimensional vectors, and $I = \{x \mid l \le x \le u\}$, n is the number of the variables, l_j and u_j are the lower and upper bounds for the jth variable, respectively, L_j and U_j are the values of the fitness function associated with the bound l_j and u_j. Generally, l_j and u_j are initialized with the lower and upper bounds of individuals. L_j and U_j are usually initialized with positive infinity. The formulation for normative knowledge updating can be depicted in Table 2.

3.2. Acceptance Function in CAFAC. The acceptance function determines which individuals and their performances can have impact on the knowledge in the belief space. The number of the individuals accepted for the update of the belief space is obtained according to the following function [1]:

$$f_a(N, t) = N \cdot \beta + \left\lfloor N \cdot \frac{\beta}{t} \right\rfloor, \tag{21}$$

where N is the size of the swarm, t is the iteration number, and β is a constant (usually chosen as 0.2).

3.3. Influence Functions in CAFAC. The belief space can influence the evolution in the population space in three ways:

(i) determining the step size of the evolution,

(ii) determining the direction of the evolution,

(iii) determining the visual distance of AFA.

More precisely, if the normative knowledge is used to determine the step size of the evolution and visual distance in AFA, our knowledge-based AFA is named as CAFAC (Ns). In four versions of CAFAC, all of the behaviours, preying, swarming, and chasing, are modelled by the knowledge. The influence function for the CAFAC is defined as in Tables 3, 4 and 5.

If the situational knowledge is used to guide the direction of the evolution, our knowledge-based AFA is named as CAFAC (Sd).

If the normative knowledge guides the step size and the visual distance meanwhile the situational knowledge is used to determine the direction of the evolution, respectively, our knowledge-based AFA is named as CAFAC (Ns+Sd).

If the normative knowledge is used to determine the step size and direction of the evolution and the visual distance, our knowledge-based AFA is named as CAFAC (Ns+Nd).

In Tables 3, 4, and 5, size$(I_k) = u_k - l_k$ is the size of the belief interval which is decided by the normative knowledge for the kth variable. The rand$(0, 1)$ is a random number uniformly distributed in the interval (0,1). The other parameters are depicted in Section 2.2.

3.4. Crossover Operator. A criterion is set up to judge whether the algorithm falls into local optimum:

$$\left| \frac{f(X_i^t) - f\left(X_i^{t-1}\right)}{f\left(X_i^{t-1}\right)} \right| < 0.1. \tag{22}$$

When the criterion is satisfied, the crossover operator will be applied to the ith artificial fish X_i $(i = 1, \ldots, N)$:

$$x_i' = x_{r1} + \alpha \times (x_{r2} - x_{r1}), \tag{23}$$

where x_{r2}, x_{r1} are two individuals selected randomly, r_1, r_2 are integers, which are generated randomly in the interval of $[1, N]$ and $r_1 \neq r_2 \neq i$. α is random number uniformly distributed in interval of $[-d, 1+d]$ and d is constant (0.25). Evaluate the child x_i' and replace the individual x_i with the child if x_i' performs better [35].

4. Application for Parameter Identification of Induction Motor

4.1. Identification Using CAFAC and PEM. In the identification process we disturb the system by voltage v and force f_{ex} excitations. In order to decrease the dimension of the problem we remove the disturbance from the data. So the input f_{ex} is set to zero. Then the problem to be considered is to match the model output with processed data using the recorded band limited white noise signal as input v. The basic idea of parameter estimation is to find a vector P to minimize the following cost function:

$$J(P) = \frac{\sum_{n=1}^{N} \left| \widehat{u}_{rc}(n) - u_{rc}(n) \right|}{N}, \tag{24}$$

where $u_{rc}(n)$ are the measurement of output for the real system under certain inputs; $\widehat{u}_{rc}(n)$ is the estimated output by exciting the model (1)-(2) using the same inputs. The experiments are carried out using a simulated reference signal generated by the real system's parameters, which have been verified by simulations for a small 30 kW two-pole cage induction motor.

Here we use an indicator of fit value to evaluate the accuracy of an identified model for a specific parameters vector P and given inputs $v(t)$ and $f_{\text{ex}}(t)$. The fit value is computed as [30]

$$md = 100 \times \left(1 - \frac{J(P)}{\left(\sum_{n=1}^{N} \left| \widehat{u}_{rc}(n) - \overline{u}_{rc} \right|^2 \right)^{1/2}} \right), \tag{25}$$

Table 2: Formulation for normative knowledge updating.

$$l_j^{t+1} = \begin{cases} x_{i,j} & \text{if } x_{i,j} \le l_j^t \text{ or } f(X_i) < L_j^t \\ l_j^t, & \text{otherwise} \end{cases} \qquad L_j^{t+1} = \begin{cases} f(X_i) & \text{if } x_{i,j} \le l_j^t \text{ or } f(X_i) < L_j^t \\ L_j^t, & \text{otherwise} \end{cases}$$

$$u_j^{t+1} = \begin{cases} x_{k,j} & \text{if } x_{k,j} \ge u_j^t \text{ or } f(X_k) < U_j^t \\ u_j^t, & \text{otherwise} \end{cases} \qquad U_j^{t+1} = \begin{cases} f(X_k) & \text{if } x_{k,j} \ge u_j^t \text{ or } f(X_k) < U_j^t \\ U_j^t, & \text{otherwise} \end{cases}$$

where the ith individual affects the lower bound for variable j, and the kth individual affects the upper bound for variable j. Note that t denotes the current generation of the belief space.

Table 3: Influence function for swarming.

	Swarming
Ns	$x_{ik}^{t+1} = x_{ik}^t + \dfrac{\text{size}(I_k) \times \text{rand}(0,1) \times (x_{ck}^t - x_{ik}^t)}{\|X_c^t - X_i^t\|}$
Sd	$x_{ik}^{t+1} = \begin{cases} x_{ik}^t + \left\lvert \dfrac{\text{rand}(0,1) \times s \times (x_{ck}^t - x_{ik}^t)}{\|X_c^t - X_i^t\|} \right\rvert & \text{if } x_{ik}^t < s_k^t \\ x_{ik}^t - \left\lvert \dfrac{\text{rand}(0,1) \times s \times (x_{ck}^t - x_{ik}^t)}{\|X_c^t - X_i^t\|} \right\rvert & \text{if } x_{ik}^t > s_k^t \\ x_{ik}^t + \dfrac{\text{rand}(0,1) \times s \times (x_{ck}^t - x_{ik}^t)}{\|X_c^t - X_i^t\|}, & \text{otherwise} \end{cases}$
NsSd	$x_{ik}^{t+1} = \begin{cases} x_{ik}^t + \left\lvert \dfrac{\text{size}(I_k) \times \text{rand}(0,1) \times (x_{ck}^t - x_{ik}^t)}{\|X_c^t - X_i^t\|} \right\rvert & \text{if } x_{ik}^t < s_k^t \\ x_{ik}^t - \left\lvert \dfrac{\text{size}(I_k) \times \text{rand}(0,1) \times (x_{ck}^t - x_{ik}^t)}{\|X_c^t - X_i^t\|} \right\rvert & \text{if } x_{ik}^t > s_k^t \\ x_{ik}^t + \dfrac{\text{size}(I_k) \times \text{rand}(0,1) \times (x_{ck}^t - x_{ik}^t)}{\|X_c^t - X_i^t\|}, & \text{otherwise} \end{cases}$
NsNd	$x_{ik}^{t+1} = \begin{cases} x_{ik}^t + \left\lvert \dfrac{\text{size}(I_k) \times \text{rand}(0,1) \times (x_{ck}^t - x_{ik}^t)}{\|X_c^t - X_i^t\|} \right\rvert & \text{if } x_{ik}^t < l_k^t \\ x_{ik}^t - \left\lvert \dfrac{\text{size}(I_k) \times \text{rand}(0,1) \times (x_{ck}^t - x_{ik}^t)}{\|X_c^t - X_i^t\|} \right\rvert & \text{if } x_{ik}^t > u_k^t \\ x_{ik}^t + \dfrac{\text{size}(I_k) \times \text{rand}(0,1) \times (x_{ck}^t - x_{ik}^t)}{\|X_c^t - X_i^t\|}, & \text{otherwise} \end{cases}$

where $\overline{u}_{rc}$ is the average value of the measurement data $\{u_{rc}(n)\}$. This indicator was chosen because it has been used in the research of optimal control of an induction motor using the prediction error method (PEM) for identification.

In our previous work, we found that the NsSd version has better performance than the three others we mentioned in Section 3 [26]. Even if the CAFAC has better optimization function than PSO, the speed of the PSO is an obvious advantage. Therefore we combine the CAFAC and the basic PSO so as to speed up the optimization process. The optimization process is implemented using the software MATAB. The basic procedure of CAFAC algorithm can be described as follows.

(1) Set all the values for the parameters and initialize the N artificial fish in the search scope with random positions.

(2) Evaluate all the artificial fishes using the fitness function y and initialize the belief space.

(3) For each ith artificial fish, simulate the preying pattern, swarming, and chasing patterns separately, and select the best child fish. If the child is better, replace the ith artificial fish with the child.

(4) Update the belief space.

(5) If the crossover criterion is satisfied, apply the crossover operator to the ith artificial fish got from Step (3).

(6) Switch to PSO until the termination criterion is satisfied.

(7) Switch to (3) until the termination criterion is satisfied.

(8) End the program if the final termination criterion is satisfied.

The termination criterion here is the same as (22) and the final termination criterion is the maximum of the whole iteration.

Table 4: Influence function for preying.

Preying	
Select next state (Ns, NsSd, NsNd)	$X_i^{t+1} = X_i^t + \text{rand}(0,1) \times \text{size}(I_i)$
$i \le$ try_num	
Ns	$x_{ik}^{t+1} = x_{ik}^t + \dfrac{\text{size}(I_k) \times \text{rand}(0,1) \times (x_{ik}^{t+1} - x_{ik}^t)}{\|X_i^{t+1} - X_i^t\|}$
Sd	$x_{ik}^{t+1} = \begin{cases} x_{ik}^t + \left\lvert \dfrac{\text{rand}(0,1) \times s \times (x_{ik}^{t+1} - x_{ik}^t)}{\|X_i^{t+1} - X_i^t\|} \right\rvert & \text{if } x_{ik}^t < s_k^t \\ x_{ik}^t - \left\lvert \dfrac{\text{rand}(0,1) \times \text{s} \times (x_{ik}^{t+1} - x_{ik}^t)}{\|\text{X}_\text{i}^{\text{t+1}} - \text{X}_\text{i}^\text{t}\|} \right\rvert & \text{if } x_{ik}^t > s_k^t \\ x_{ik}^t + \dfrac{\text{rand}(0,1) \times \text{s} \times (x_{ik}^{t+1} - x_{ik}^t)}{\|\text{X}_\text{i}^{\text{t+1}} - \text{X}_\text{i}^\text{t}\|}, & \text{otherwise} \end{cases}$
NsSd	$x_{ik}^{t+1} = \begin{cases} x_{ik}^t + \left\lvert \dfrac{\text{size}(I_k) \times \text{rand}(0,1) \times (x_{ik}^{t+1} - x_{ik}^t)}{\|X_i^{t+1} - X_i^t\|} \right\rvert & \text{if } x_{ik}^t < s_k^t \\ x_{ik}^t - \left\lvert \dfrac{\text{size}(I_k) \times \text{rand}(0,1) \times (x_{ik}^{t+1} - x_{ik}^t)}{\|\text{X}_\text{i}^{\text{t+1}} - \text{X}_\text{i}^\text{t}\|} \right\rvert & \text{if } x_{ik}^t > s_k^t \\ x_{ik}^t + \dfrac{\text{size}(I_k) \times \text{rand}(0,1) \times (x_{ik}^{t+1} - x_{ik}^t)}{\|X_i^{t+1} - X_i^t\|}, & \text{otherwise} \end{cases}$
NsNd	$x_{ik}^{t+1} = \begin{cases} x_{ik}^t + \left\lvert \dfrac{\text{size}(I_k) \times \text{rand}(0,1) \times (x_{ik}^{t+1} - x_{ik}^t)}{\|\text{X}_\text{i}^{\text{t+1}} - \text{X}_\text{i}^\text{t}\|} \right\rvert & \text{if } x_{ik}^t < l_k^t \\ x_{ik}^t - \left\lvert \dfrac{\text{size}(I_k) \times \text{rand}(0,1) \times (x_{ik}^{t+1} - x_{ik}^t)}{\|\text{X}_\text{i}^{\text{t+1}} - \text{X}_\text{i}^\text{t}\|} \right\rvert & \text{if } x_{ik}^t > u_k^t \\ x_{ik}^t + \dfrac{\text{size}(I_k) \times \text{rand}(0,1) \times (x_{ik}^{t+1} - x_{ik}^t)}{\|X_i^{t+1} - X_i^t\|}, & \text{otherwise} \end{cases}$
$i >$ try_num	
Ns	$x_{ik}^{t+1} = x_{ik}^t + \text{size}(I_k) \times \text{rand}(0,1)$
Sd	$x_{ik}^{t+1} = \begin{cases} x_{ik}^t + \lvert\text{rand}(0,1) \times s\rvert & \text{if } x_{ik}^t < s_k^t \\ x_{ik}^t - \lvert\text{rand}(0,1) \times s\rvert & \text{if } x_{ik}^t > s_k^t \\ x_{ik}^t + \text{rand}(0,1) \times s, & \text{otherwise} \end{cases}$
NsSd	$x_{ik}^{t+1} = \begin{cases} x_{ik}^t + \lvert\text{size}(I_k) \times \text{rand}(0,1)\rvert & \text{if } x_{ik}^t < s_k^t \\ x_{ik}^t - \lvert\text{size}(I_k) \times \text{rand}(0,1)\rvert & \text{if } x_{ik}^t > s_k^t \\ x_{ik}^t + \text{size}(I_k) \times \text{rand}(0,1), & \text{otherwise} \end{cases}$
NsNd	$x_{ik}^{t+1} = \begin{cases} x_{ik}^t + \lvert\text{size}(I_k) \times \text{rand}(0,1)\rvert & \text{if } x_{ik}^t < l_k^t \\ x_{ik}^t - \lvert\text{size}(I_k) \times \text{rand}(0,1)\rvert & \text{if } x_{ik}^t > u_k^t \\ x_{ik}^t + \text{size}(I_k) \times \text{rand}(0,1), & \text{otherwise} \end{cases}$

In PEM identification the general idea is to produce a model that minimizes a norm, such as

$$V_N\left(\theta, Z^N\right) = \frac{1}{N}\sum_{t=0}^{N} \ell(\varepsilon_F(t,\theta)), \tag{26}$$

where $\varepsilon_F(t,\theta)$ is the prediction error filtered through a linear filter and $\ell(\cdot)$ is a scalar function [36]. Z^N is the data consisting of N samples and θ is the model parameterization (i.e., polynomials). The problem is usually solved iteratively using gradient-based methods.

With the identification data, the PEM identification will result in fit values of 79.1 and 80.6 in horizontal and vertical directions. The CAFAC identification produced a model that had fit values of 73.9 and 77.7. Figure 4 displays the filtered measurement, and the model outputs from PEM and the parametric model. It can be stated that the models estimate the data reasonably well. The main differences occur near zero where the response is modest.

4.2. Simulation Results. The obtained model was tested in simulations by implementing a state observer and a linear quadratic controller (LQ) for the model. The same was done in [29] with a model, which was identified using PEM. A real measurement of rotor vibrations (similar to

Table 5: Influence function for chasing.

Chasing	
Ns	$x_{ik}^{t+1} = x_{ik}^{t} + \dfrac{\text{size}(I_k) \times \text{rand}(0,1) \times (x_{\min\, k}^{t} - x_{ik}^{t})}{\|X_{\min}^{t} - X_i^{t}\|}$
Sd	$x_{ik}^{t+1} = \begin{cases} x_{ik}^{t} + \left\lvert \dfrac{\text{rand}(0,1) \times s \times (x_{\min\, k}^{t} - x_{ik}^{t})}{\|X_{\min}^{t} - X_i^{t}\|} \right\rvert & \text{if } x_{ik}^{t} < s_k^{t} \\ x_{ik}^{t} - \left\lvert \dfrac{\text{rand}(0,1) \times s \times (x_{\min\, k}^{t} - x_{ik}^{t})}{\|X_{min}^{t} - X_i^{t}\|} \right\rvert & \text{if } x_{ik}^{t} > s_k^{t} \\ x_{ik}^{t} + \dfrac{\text{rand}(0,1) \times s \times (x_{\min\, k}^{t} - x_{ik}^{t})}{\|X_{\min}^{t} - X_i^{t}\|}, & \text{otherwise} \end{cases}$
NsSd	$x_{ik}^{t+1} = \begin{cases} x_{ik}^{t} + \left\lvert \dfrac{\text{size}(I_k) \times \text{rand}(0,1) \times (x_{\min\, k}^{t} - x_{ik}^{t})}{\|X_{\min}^{t} - X_i^{t}\|} \right\rvert & \text{if } x_{ik}^{t} < s_k^{t} \\ x_{ik}^{t} - \left\lvert \dfrac{\text{size}(I_k) \times \text{rand}(0,1) \times (x_{\min\, k}^{t} - x_{ik}^{t})}{\|X_{\min}^{t} - X_i^{t}\|} \right\rvert & \text{if } x_{ik}^{t} > s_k^{t} \\ x_{ik}^{t} + \dfrac{\text{size}(I_k) \times \text{rand}(0,1) \times (x_{\min\, k}^{t} - x_{ik}^{t})}{\|X_{\min}^{t} - X_i^{t}\|}, & \text{otherwise} \end{cases}$
NsNd	$x_{ik}^{t+1} = \begin{cases} x_{ik}^{t} + \left\lvert \dfrac{\text{size}(I_k) \times \text{rand}(0,1) \times (x_{\min\, k}^{t} - x_{ik}^{t})}{\|X_{\min}^{t} - X_i^{t}\|} \right\rvert & \text{if } x_{ik}^{t} < l_k^{t} \\ x_{ik}^{t} - \left\lvert \dfrac{\text{size}(I_k) \times \text{rand}(0,1) \times (x_{\min\, k}^{t} - x_{ik}^{t})}{\|X_{\min}^{t} - X_i^{t}\|} \right\rvert & \text{if } x_{ik}^{t} > u_k^{t} \\ x_{ik}^{t} + \dfrac{\text{size}(I_k) \times \text{rand}(0,1) \times (x_{\min\, k}^{t} - x_{ik}^{t})}{\|X_{\min}^{t} - X_i^{t}\|}, & \text{otherwise} \end{cases}$

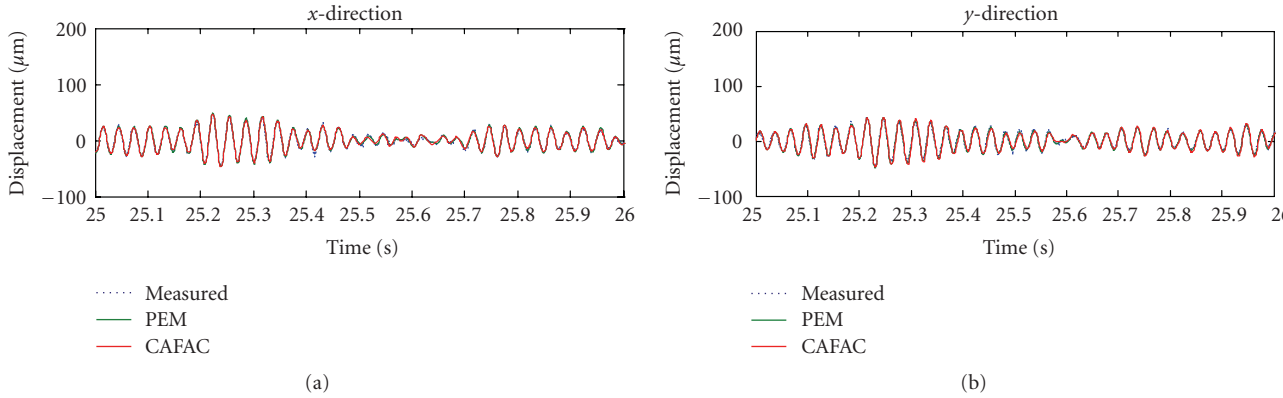

Figure 4: Measured data and modelled outputs using PEM and CAFAC identification methods.

the identification data, but including the disturbance and not input signal) in the 2-pole induction motor was used as the input in the simulations. The expected result was that the observer would follow this signal and the LQ controller, fed through the model of the actuator and would compensate the vibrations. Figure 5 shows the estimation error of the observer. It can be concluded that the observer works decently since the amplitude of the estimation error is about 5 μm and the measured amplitude varies between 130 and 240 μm. The control result is displayed in Figure 6, where the controller is switched on after three seconds. During the 17-second period when control is on, the reductions of the vibrations are up to 67.0% and 70.3% and the control also reduces the fluctuation of the amplitude, which depends on the slip angle.

It is also necessary to consider the control signal because the test equipment can produce voltages in the range of ± 100 V, and naturally the voltage levels should not be very high in a properly working controller. Figure 7 shows that there is at first a peak in the control signal, which reaches the saturation level, but it settles close to ± 20 V range after 0.02 seconds.

The same simulations were also done with the black box model, which was identified using PEM, and the controller was tuned in the same manner. In this case the controller reduced vibrations in the simulations by 70.0% and 64.2%. The result is displayed in Figure 8. The control signals with the PEM model stay between ± 50 V after that (see Figure 9). Strictly based on this data, the parametric model is slightly better than the PEM identification. However, the parametric

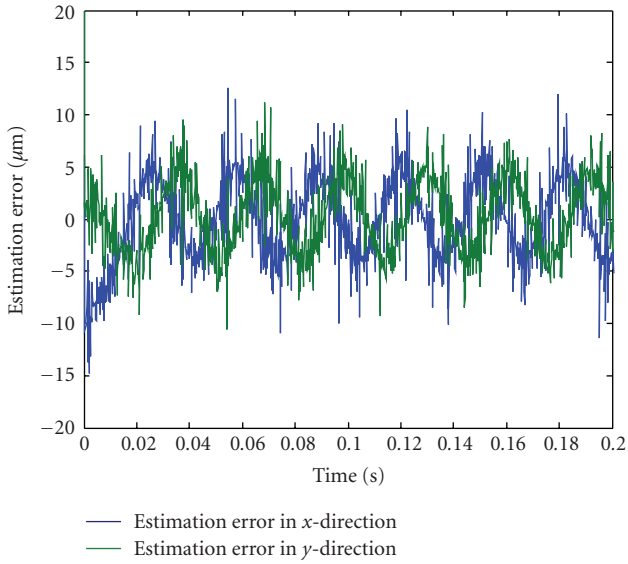

Figure 5: The estimation error of the observer in x- and y-directions.

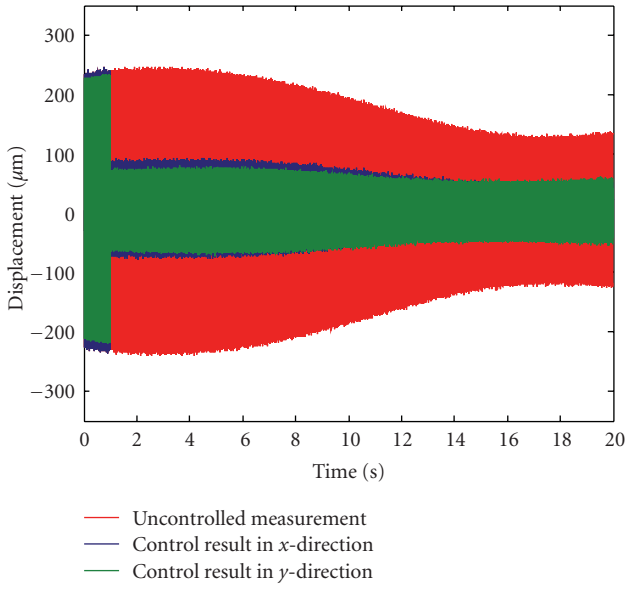

Figure 6: Rotor displacement with the CAFAC model when control is switched on after 3 seconds.

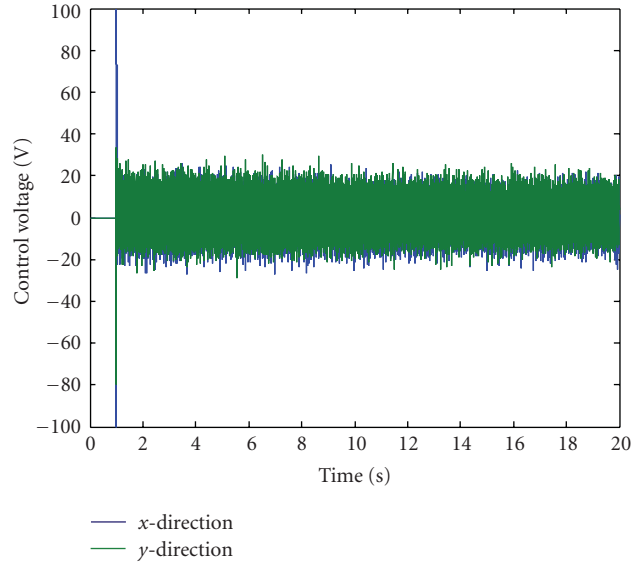

Figure 7: Control voltage of the LQ controller with CAFAC model when control is switched off after 3 seconds.

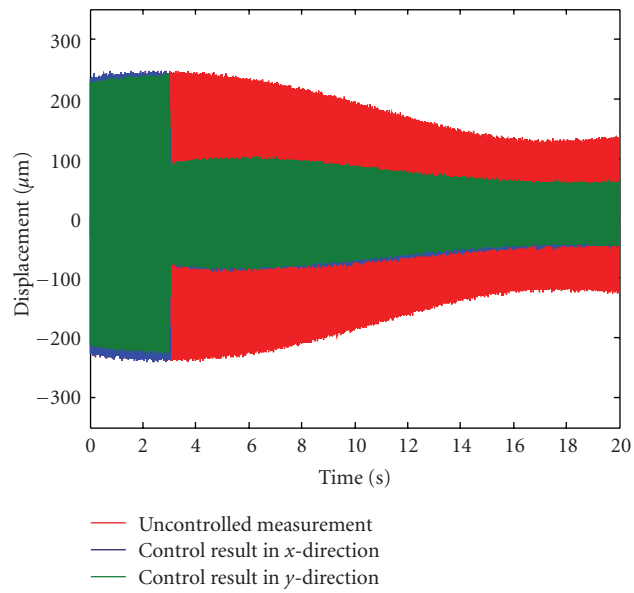

Figure 8: Rotor displacement with the PEM model when control is switched on after 3 seconds.

model has not yet been successfully used in the real environment, whereas the PEM identification has been proven to work and to provide a reduction of the vibrations up to 90% depending on how the controller is tuned.

5. Conclusions

In this paper, we used a knowledge-based Artificial Fish-Swarm optimization algorithm to identify the parameters of an actuator model in an electrical machine. The culture framework was invested to direct the crossover operation in the AFA. In the culture framework, the situation knowledge and the normative knowledge were employed to guide the evolution of the Artificial Fish-Swarm optimization. The crossover operation can help the artificial fish jump out of the local optimum without losing the characteristics of the previous generation. The proposed knowledge-based Artificial Fish-Swarm optimization can improve the performance of the original Artificial Fish-Swarm optimization and can be applied, for example, to find parameter values for a model of an actuator used for vibration control of rotor in an induction motor. Realistic values for the components of a structural first-principles electromechanical model were obtained, which improved the earlier identification results

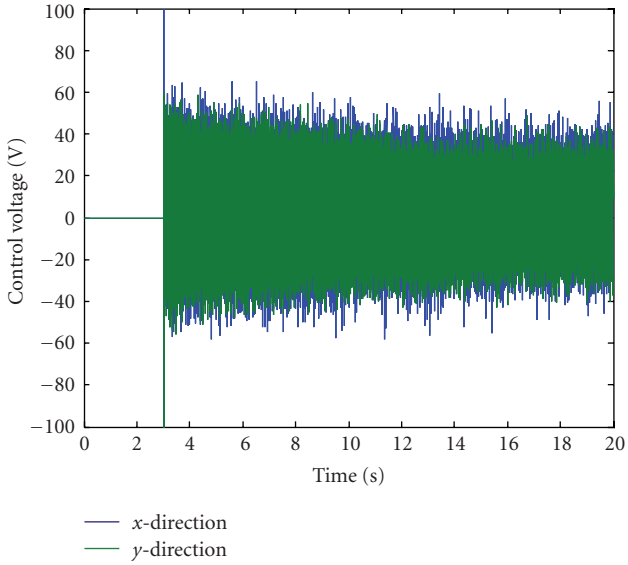

Figure 9: Control voltage of the LQ controller with PEM model when control is switched on after 3 seconds.

considerably. The results compared well with those obtained by PEM identification, but because the latter does not provide physical parameter values, the method presented in the paper can be considered an improvement. Also, the nature-inspired evolutionary algorithms considered are particularly interesting, because they are computationally effective and reasonably easy to understand. Also, they do not need computation of gradients. For the future works, a time-varying model must be considered. In order to do that, more knowledge in the culture framework should be invested and more swarm intelligence must be tested to succeed in parameter identification.

Acknowledgment

This research work was funded by the Academy of Finland under Grants 135225 and 127299 and the NSFC under Grant no. 60874084.

References

[1] R. K. Ursem, *Models for evolutionary algorithms and their applications in system identification and control optimization*, Ph.D. dissertation., Department of Computer Science University of Aarhus, Aarhus University, Aarhus, Denmark, 2003.

[2] Y. H. Shi and R. Eberhart, "Parameter selection in particle swarm optimization," in *Proceedings of the 7th Annual Conference on Evolutionary Programming*, pp. 591–600, Washington, DC, USA, 1998.

[3] T. Kumon, M. Iwasaki, T. Suzuki, T. Hashiyama, N. Matsui, and S. Okuma, "Nonlinear system identification using genetic algorithm," in *Proceedings of the 26th Annual Conference of the IEEE Electronics Society (IECON '00)*, vol. 4, pp. 2485–2491, 2000.

[4] R. Storn, "System design by constraint adaptation and differential evolution," *IEEE Transactions on Evolutionary Computation*, vol. 3, no. 1, pp. 22–34, 1999.

[5] E. Bonabeau, M. Dorigo, and G. Theraulaz, *Swarm Intelligence: From Natural to Artificial Systems*, Oxford University Press, New York, NY, USA, 1999.

[6] X. L. Li, Z. J. Shao, and JI. X. Qian, "Optimizing method based on autonomous animats: fish-swarm algorithm," *System Engineering Theory and Practice*, vol. 22, no. 11, p. 32, 2002.

[7] R. Eberhart and J. Kennedy, "A new optimizer using particle swarm theory," in *Proceedings of the 6th International Symposium on Micro Machine and Human Science*, pp. 39–43, Nagoya, Japan, 2002.

[8] Y. Shi and R. Eberhart, "A modified particl swarm optimizer," in *Proceedings of the IEEE World Congress on Computational Intelligence*, pp. 69–73, Anchorage, Alaska, USA, 1998.

[9] U. Baumgartner, C. H. Magele, and W. Renhart, "Pareto optimality and particle swarm optimization," *IEEE Transactions on Magnetics*, vol. 40, no. 2, pp. 1172–1175, 2004.

[10] M. S. Voss and X. Feng, "Emergent system identification using particle swarm optimization," in *The International Society for Optical Engineering*, vol. 4512 of *Proceedings of SPIE*, Hutchinson Island, Fla, USA, June 2001.

[11] S. Z. Rizvi and H. N. Al-Duwaish, "A PSO-Subspace algorithm for identification of Hammerstein models," in *Proceedings of the IFAC Conference on Control Applications of Optimisation*, p. 5, Agora, Finland, 2009.

[12] V. Katari, S. Malireddi, S. K. S.bendapudi, and G. Panda, "Adaptive nonlinear system identification using comprehensive learning PSO," in *Proceedings of the 3rd International Symposium on Communications, Control, and Signal Processing (ISCCSP '08)*, pp. 434–439, Las Vegas, Nev, USA, 2008.

[13] S. Chen, T. Mei, M. Luo, and X. Yang, "Identification of nonlinear system based on a new hybrid gradient-based PSO algorithm," in *Proceedings of the International Conference on Information Acquisition (ICIA '07)*, pp. 265–268, Jeju City, Korea, July 2007.

[14] Y. Liu and X. He, "Modeling identification of power plant thermal process based on PSO algorithm," in *Proceedings of the American Control Conference (ACC '5)*, pp. 4484–4489, Portland, Ore, USA, June 2005.

[15] E. Král, V. Lubomír, V. Pollinay, and P. Varacha, "Usage of PSO algorithm for parameters identification of district heating," *Latest Trends on Systems*, vol. 2, no. 657, p. 659, 2010.

[16] Y.-L. Zhou, Q.-Y. He, and M.-F. Xu, "Application of artificial fish-swarm algorithm in gas-solid fluidized bed flow regime identification," *Chemical Engineering*, vol. 38, no. 7, pp. 39–42+50, 2010.

[17] R. G. Reynolds, "An introduction to cultural algorithms," in *Proceedings of the 3rd Annual Conference on Evolutionary Programming*, pp. 131–139, San Diego, Calif, USA, 1994.

[18] R. G. Reynolds and B. Peng, "Cultural algorithms: modeling of how cultures learn to solve problems," in *Proceedingsof the 16th IEEE International Conference on Tools with Artificial Intelligence (ICTAI '04)*, pp. 166–172, Boca Raton, Fla, USA, November 2004.

[19] C. J. Chung, *Knowledge-based approaches to self-adaptation in cultural algorithms*, Ph.D. Dissertation, Department of Computer Science, Wanyne State University, Detroit, Mich, USA, 1997.

[20] R. G. Reynolds and C. J. Chung, "Knowledge-based self-adaptation in evolutionary programming using cultural algorithms," in *Proceedings of the IEEE Conference on Evolutionary*

Computation (ICEC 97), pp. 71–75, Indianapolis, Ind, USA, 1997.

[21] Robert G. Reynolds and Chung, "Knowledge-based self-adaptation in evolutionary programming using cultural algorithms," in *Proceedings of the IEEE Conference on Evolutionary Computation (ICEC '97)*, pp. 71–75, Indianapolis, Ind, USA, 1997.

[22] L. S. Dos Coelho and V. C. Mariani, "An efficient particle swarm optimization approach based on cultural algorithm applied to mechanical design," in *Proceedings of the IEEE Congress on Evolutionary Computation (CEC '06)*, pp. 1099–1104, Vancouver, Canada, July 2006.

[23] Y. Huang, Y. Xu, and G. Chen, "The culture-based particle swarm optimization algorithm," in *Proceedings of the 4th International Conference on Natural Computation (ICNC '08)*, pp. 256–262, Jinan, China, October 2008.

[24] Y. Wu, X.-Z. Gao, X.-L. Huang, and K. Zenger, "A cultural Particle Swarm Optimization algorithm," in *Proceedings of the 2010 6th International Conference on Natural Computation (ICNC '10)*, vol. 5, pp. 2505–2509, Yantai, China, 2010.

[25] Y. Wu, X.-Z. Gao, X.-L. Huang, and K. Zenger, "A hybrid optimization method of particle swarm optimization and cultural algorithm," in *Proceedings of the 6th International Conference on Natural Computation (ICNC '10)*, vol. 5, pp. 2515–2519, Yantai, China, 2010.

[26] X. Z. Gao, Y. Wu, K. Zenger, and X. Huang, "A knowledge-based artificial fish-swarm algorithm," in *Proceedings of the 13th IEEE International Conference on Computational Science and Engineering (CSE '10)*, pp. 327–332, Hong Kang, China, 2010.

[27] L. D. S. Coelho, R. C. T. Souza, and V. C. Mariani, "Improved differential evolution approach based on cultural algorithm and diversity measure applied to solve economic load dispatch problems," *Mathematics and Computers in Simulation*, vol. 79, no. 10, pp. 3136–3147, 2009.

[28] A. Sinervo, *Modeling and control of flexural rotor vibration of a two-pole cage induction motor*, M.S. thesis, Department of electrical Engineering, Faculty of electronics, Communications and Automation, Helsinki University of Technology, Espoo, Finland, 2008.

[29] A. Laiho, A. Sinervo, J. Orivuori, K. Tammi, A. Arkkio, and K. Zenger, "Attenuation of harmonic rotor vibration in a cage rotor induction machine by a self-bearing force actuator," *IEEE Transactions on Magnetics*, vol. 45, no. 12, Article ID 5326448, pp. 5388–5398, 2009.

[30] J. Orivuori, K. Zenger, and A. Sinervo, "Active control of rotor vibrations by advanced control methods," in *Proceedings of the 16th International Congress on Sound and Vibration- Recent Developments in Acoustics, Noice and Vibration*, M. Pawelczyk and D. Bismor, Eds., Krakow, Poland, 2010.

[31] A. Laiho, K. Tammi, and V. Vidquist, "Modelling of flexural rotor vibration and time-periodic system dynamics in a two-pole cage induction machine equipped with a self-bearing force actuator," in *Proceedings of the IFAC Workshop on Periodic Systems*, Bogazici University, Turkey, 2010.

[32] G. Genta, *Vibration of Structures and Machines: Practical Aspects. Section 6.4.*, Springer, New York, NY, USA, 1999.

[33] A. Laiho, K. Tammi, K. Zenger, and A. Arkkio, "A model-based flexural rotor vibration control in cage induction electrical machines by a built-in force actuator," *Electrical Engineering*, vol. 90, no. 6, pp. 407–421, 2008.

[34] T. P. Holopainen, A. Tenhunen, E. Lantto, and A. Arkkio, "Unbalanced magnetic pull induced by arbitrary eccentric motion of cage rotor in transient operation. Part 1: analytical model," *Electrical Engineering*, vol. 88, no. 1, pp. 13–24, 2005.

[35] X. P. Wang and L. M. Cao, *Genetic Algorithm: Theory, Application and Software Implementation*, Xi'an JiaoTong University Press, Xi'an, China, 2002.

[36] P. Krause, *Analysis of Electric Machinery*, McGraw–Hill, New York, NY, USA, 1987.